Advanced Manufacturing of Microfiber Conduits for Tissue Engineering

Kelly L. O'Neill

A dissertation accepted and approved in partial fulfillment of the

requirements for the degree of

Doctor of Philosophy

in Bioengineering

Dissertation Committee:

Timothy J. Gardner, Chair

Paul D. Dalton, Advisor

Morgan Giers, Core Member

Erin McColl, Core Member

Cristopher M. Niell, Institutional Representative

University of Oregon

&

Oregon State University

Fall 2025

DISSERTATION ABSTRACT

Kelly L. O'Neill

Doctor of Philosophy in Bioengineering

Title: Advanced Manufacturing of Microfiber Conduits for Tissue Engineering

This thesis investigates the application of high-resolution additive manufacturing, specifically melt electrowriting (MEW), for the fabrication of bioengineered scaffolds designed for tissue engineering (TE).

The research spans the scientific, technological, and translational dimensions of MEW, beginning with an in-depth exploration of the process fundamentals, material behavior, and precision control mechanisms that enable microscale fiber deposition. Building upon this foundation, the thesis advances the design and characterization of MEW-fabricated scaffolds with precise fiber architecture and biological functionality towards TE applications.

Beyond laboratory-scale innovation, this work extends toward translational development through the conceptualization of a prototype nerve guidance conduit under the working name *PeriMend3D*. Peripheral nerve injuries remain a significant clinical challenge, often resulting in permanent functional loss and reduced quality of life. Current gold-standard treatments, such as autografts, are limited by donor site morbidity, size mismatch, and incomplete regeneration. To address these limitations, *PeriMend3D* case study integrates regulatory, manufacturing, and

commercialization strategies, illustrating how MEW-based technologies can evolve from experimental platforms to viable medical device candidates.

Collectively, the findings establish MEW as a robust and versatile additive manufacturing technology capable of fabricating reproducible, high-fidelity scaffolds for TE applications that meet both scientific and translational demands.

This dissertation includes previously published coauthored material.

ACKNOWLEDGMENTS

I would like to begin by expressing my sincere gratitude to my advisor, Paul Dalton, for his mentorship, patience, and guidance. I am deeply thankful to Phil and Penny Knight for their generous funding and support, which made this work possible. To my lab members, thank you for creating an inspiring, collaborative, and supportive environment that made every challenge worthwhile. I am grateful to my committee members for their valuable feedback and time.

I extend my appreciation to the Knight Campus Undergraduate Scholarship program and to my wonderful mentees, Amanda Kurtz and Georgia Van der Linden. I thank the Impact Team, the professors in Bioengineering and the professors in the Lillis School of Business for broadening my perspective and challenging me to think critically across disciplines. Special thanks to the Entrepreneurship Center at the Lillis School of Business for offering insight into translating research beyond the lab, and the Oregon Innovation Challenge (OIC) Team for their encouragement and teamwork. I am very grateful to the staff at the International Student and Scholar Services (ISSS).

I thank Geordi Allred, Julien McAdams, Jefferson Garman and John Boosinger, the engineers at the machine shop, for their exceptional skill and dedication in building custom printer components essential for this work. I would also like to thank Kelly Leguineche, Melissa Bemrose, and Vinni Thoms for their help while I was setting up the Dalton Lab cell culture room, and Kait Link for the coordination of tissue harvests.

Finally, to all my colleagues and professors, thank you for the countless discussions, insights, and moments of collaboration that shaped this research and my growth as a scientist.

PUBLICATIONS ARISING DURING THIS THESIS

1. Kim J, Bakirci E, **O'Neill KL**, Hrynevich A, Dalton PD (2021). Fiber bridging during melt electrowriting of poly(ε-caprolactone) and the influence of fiber diameter and wall height. *Macromol Mater Eng*, 306, 2000685.
2. Dalton PD, **O'Neill KL**, Pêgo AP, Plant GW, Nisbet DR, Oudega M, Brook GA, Harvey AR (2023) Chapter 17: Tissue Engineering of the Nervous System, in Tissue Engineering. 3rd Edition, De Boer & Van Blitterswijk, Academic Press. ISBN 9780128244593, pp 585-628.
3. **O'Neill KL**, Dalton PD (2023) A decade of melt electrowriting, *Small Methods*, **7**, 2201589.
4. Hall PC, Reid HW, Liashenko I, Tandon B, **O'Neill KL**, Paxton NC, Lindberg GCJ, Jasti R, Dalton PD (2024) [n]Cycloparaphenylenes as Compatible Fluorophores for Melt Electrowriting. *Small*, 20, 2400882.
5. **O'Neill KL**, Kurtz A, Liashenko I, Rocha G, Paxton NC, Dalton PD. (2024) Tailoring Cell Attachment onto Melt Electrowritten Scaffolds via a Phase Separated Hydrogel Coating with Peptide Functionalization. *Advanced Interface Technologies*, **12**, 2400692.
6. **O'Neill KL**, McLoughlin T, Van der Linden G, Buson IL, Paxton NC, Polites M, Dalton PD. (2025) Visualizing fiber path and generating G-code for melt electrowriting of tubular scaffolds using Grasshopper software. *Visual and Virtual Prototyping*, **20**, e2466190.
7. Galindo AN, Chi AK, Liashenko I, **O'Neill KL**, Sharma R, Khachatourian JD, Dalton PD, Hettiaratchi MH. (2025) Hyaluronic Acid-Coated Melt Electrowritten Scaffolds Promote Myoblast Attachment, Alignment, and Differentiation, *Cellular and Molecular Bioengineering* https://doi.org/10.1007/s12195-025-00865-y.
8. Guyer T, Gill D, Leguineche KE, Link K, Jones K, Williams KE, Strait LK, **O'Neill KL**, Hastings MA, Lin A, Maniar D, Roy K, Guldberg RE, All-trans Retinoic Acid Modulates Circulating Immune Cells in a Preclinical Model of Musculoskeletal Trauma Submitted to Journal of Orthopaedic Research (2025).
9. **O'Neill KL**, Williams KE, Hajarizadeh A, Rauff A, Liashenko I, Guldberg RE, Dalton PD Automated Seamless Poly(ε-caprolactone) Electrospun Tubes for Critically-Sized Bone Defect Repair. *Submitted to Tissue Engineering Part C: Methods* (Dec 2025).

TABLE OF CONTENTS

LIST OF FIGURES

LIST OF TABLES

CHAPTER 1: INTRODUCTION

Tissue engineering (TE) integrates materials science, cellular biology, and advanced manufacturing to study, restore or replace damaged tissues. With scaffolds and matrices being a fundamental part of TE, additive manufacturing techniques including melt electrowriting (MEW) have impacted the field with increased structural precision of biomaterial fabrication.

As a hybrid between solution electrospinning (SES) and traditional 3D printing (known as fused filament fabrication (FFF)), MEW extrudes molten polymer under a controlled electric field, producing fibers in the sub-micron to 50 μm range that can be deposited with precision. Unlike traditional SES, which usually produces randomly oriented fibrous mats, MEW allows for layer-by-layer construction of scaffolds with user-defined orientation, porosity, and geometry. Compared to FFF, MEW includes applying a high voltage between the printer head and collector, which allows for the production of much thinner fibers. The combination of these features make MEW ideally suited to fabricating microscale architectures. This level of architectural precision is particularly important for TE applications, where features such as alignment, porosity, and mechanical properties dictate cellular organization and function. Moreover, MEW operates with medical-grade polymers such as poly(ε-caprolactone) (PCL) and poly(L-lactide-co-ε-caprolactone) (PLCL), ensuring compatibility with regulatory and translational frameworks.

The overarching goal of this doctoral thesis is to advance the scientific, technological, and translational potential of MEW towards TE applications. The central hypothesis of this thesis is that by integrating MEW's structural precision with biological and translational design principles, it is possible to create scaffolds inspired by natural architecture. Through a sequence of interlinked studies, this work establishes MEW as a reproducible and scalable platform for design and manufacturing of scaffolds for TE applications in muscle, bone and peripheral nerve.

The objectives of this work are:

1. To establish precise MEW hardware for a comprehensive understanding of the process (its electrohydrodynamic principles, operational parameters, and processing limitations) to enable reproducible fabrication of microscale structures suitable for TE (Chapter 2).

2. To develop computational design tools for MEW tubular printing, introducing parametric modeling and automated G-code generation to bridge digital design prototyping and physical fabrication (Chapter 3).

3. To expand MEW toward multi-material fabrication, integrating PCL and PLCL to produce seamless tubular scaffolds with aligned structures towards TE applications (Chapter 4).

4. To incorporate functionalized coatings onto MEW scaffolds, enabling controlled cell attachment and biochemical signaling through hydrogel-peptide integration (Chapter 5).

5. To improve automated manufacturing of tubes and demonstrate their relevance to broader TE contexts, such as bone defect repair (Chapter 6).

6. To analyze the commercialization opportunities for MEW-based scaffolds, establishing regulatory, market, and financial frameworks for clinical deployment of a nerve guidance conduit through the case study “PeriMend3D” (Chapter 7).

Collectively, these objectives form a cohesive research arc that advances MEW from a microfabrication technique to a broadly relevant biofabrication platform.

Thesis Overview

This thesis begins with a comprehensive review of MEW research since its development in 2011, focusing on electrohydrodynamic principles, operational parameters, and processing

limitations. A Decade of Melt Electrowriting (Chapter 2) establishes the technological and conceptual foundation upon which all subsequent chapters are built. This work identifies how parameters such as voltage, pressure, collector speed, and temperature govern fiber morphology during MEW processing. By defining key concepts like critical translation speed (CTS) and jet lag, the chapter formalizes a framework that allows predictive control over scaffold structure and establishes reproducible conditions for medical-grade PCL printing. This work situates MEW as a reliable, tunable process for creating microscale scaffolds. This chapter includes published work with co-author Paul D. Dalton.

Building upon this theoretical groundwork, the work presented in Chapter 3 introduces a parametric modeling environment capable of visualizing fiber trajectories and generating G-code for tubular collectors. Through the integration of Rhinoceros and Grasshopper software, this platform improves upon existing virtual prototyping tools that enabled control over winding angles, inter-fiber spacing, and tube geometry, but were limited in tubular design options. The new Grasshopper program aims to reduce the barrier for adoption for new MEW users, and simultaneously aid experienced users improve design iterations via virtual prototyping. This chapter includes published work with co-authors Taite McLoughlin, Georgia Van der Linden, Ignacio Lopez Buson, Naomi C. Paxton, Mary Polites and Paul D. Dalton.

Having established the theoretical foundations and user design/control, the thesis advances toward expanding MEW's material and design capabilities. Chapter 4 details the development of a custom four-axis MEW printer designed to fabricate seamless tubular scaffolds from different polymers. By demonstrating the successful printing of both semi-crystalline PCL and elastic PLCL tubular structures, the chapter demonstrates a milestone in MEW adaptability.

Chapter 5 introduces biochemical control through a synthetic hydrogel coating. By applying phase-separated poly(2-hydroxyethyl methacrylate) (pHEMA) hydrogels functionalized with RGD peptides, the study establishes a strategy for tailoring cell adhesion. The resulting hybrid scaffolds combine MEW's structural fidelity with bioactive interfaces that selectively promote cell attachment. This chapter includes published work with co-authors Amanda Kurtz, Ievgenii Liashenko, Guilherme Rocha, Naomi C. Paxton and Paul D. Dalton.

While earlier chapters focus on microstructural precision and biological response, Chapter 6 broadens the scope to scalable and automated manufacturing. The development of seamless, electrospun PCL tubes for bone defect repair demonstrates how automation enhances reproducibility and throughput. By integrating programmable perforation and eliminating manual assembly, this approach establishes a process for improved manufacturing. This chapter includes published work with co-authors Kylie E. Williams, Auveen Hajarizadeh, Adam Rauff, Ievgenii Liashenko, Robert E. Guldberg and Paul D. Dalton.

The final chapter (Chapter 7) unites the scientific and translational aspects of the thesis through the case study PeriMend3D. PeriMend3D represents a commercialization analysis for MEW-fabricated nerve guidance conduits and was developed under the Specialization in Innovation and Entrepreneurship taught at Lillis School of Business at the University of Oregon, and the entrepreneurship program Oregon Innovation Challenge (OIC). This chapter situates the research within the ecosystem of medical device development, outlining regulatory pathways, market segmentation strategies, and funding models. By integrating surgeon feedback into scaffold design, the project translates laboratory insights into a viable product concept. In doing so, it bridges academic research with clinical and commercial implementation, demonstrating how precision biofabrication can evolve from innovation to impact.

CHAPTER 2: A DECADE OF MELT ELECTROWRITING

O'Neill KL, Dalton PD (2023) A decade of melt electrowriting, *Small Methods*, **7**, 2201589.

The review A Decade of Melt Electrowriting provides the most comprehensive synthesis to date of the scientific principles and processing fundamentals that define MEW. The chapter elucidates how the dynamic interplay between voltage, pressure, collector speed, and temperature governs jet stability, fiber morphology, and scaffold fidelity. Through this systematic integration of material science and process control, it defines the parameters that enable high-resolution fabrication of reproducible, microscale architectures suitable for TE.

Scientific Contribution and Advancement of Knowledge

This chapter expands the scientific understanding of MEW as an electrohydrodynamic manufacturing process. It identifies the interdependent relationships among key variables that determine fiber trajectory, deposition accuracy, and structural organization. Concepts such as CTS, jet lag, charge accumulation, and fiber bridging are defined and contextualized within a framework that advances both theoretical and practical knowledge of micro-scale jet behavior. By explaining how these parameters influence fiber placement and morphology, the work facilitates the prediction and optimization of scaffold characteristics. The identification of reproducible conditions for medical-grade PCL printing provides a transferable foundation for future studies and applications.

Broader Implications and Future Directions

The insights presented in this review broadly cover fields of tissue engineering, biomaterials science, and advanced manufacturing. The discussion of visualization tools, machine

vision, and open-source system design demonstrates the potential for MEW to become a widely accessible and standardized fabrication technique. The chapter positions MEW as both a precise engineering process and an enabling scientific discipline that supports the design and fabrication of microstructured biomaterials. Its findings provide a roadmap for future innovations in scaffold design and fabrication precision, contributing to the long-term objective of developing patient-specific and clinically effective solutions for complex tissue injuries.

A Decade of Melt Electrowriting

*Kelly L. O'Neill and Paul D. Dalton**

Phil and Penny Knight Campus for Accelerating Scientific Impact, University of Oregon, 1505 Franklin Boulevard, Eugene, OR 97403-6231, USA

*Corresponding author: Paul D. Dalton pdalton@uoregon.edu

Keywords: melt electrospinning writing, additive manufacturing, 3D printing, poly-ε-caprolactone (PCL), biofabrication.

Abstract for “A Decade of Melt Electrowriting”

Over the past decade, melt electrowriting (MEW) has established the fundamental understanding of processing (and printer) requirements. Iterative work on parametric development and dissemination of this recent additive manufacturing (AM) technology have been performed across many systems and polymers (mainly poly-(ε-caprolactone)), showing similarities and trends. However, the software and hardware ecosystem of MEW are not mature. Further, due to its multi-parametric nature, MEW can be challenging for laboratories to master. This review intends to provide a unique perspective on the dynamic relationship between MEW processing parameters. Such parameters can be divided into 1) those that affect the polymer flow rate *to* or 2) *from* the nozzle, and 3) environmental conditions. The most influential parameters for high quality printing are applied voltage, applied pressure, collector speed, polymer temperature, nozzle diameter and the conditions that lead to charge buildup (e.g., relative humidity). Other factors such as ambient temperature, nozzle size and protrusion, collector temperature and conductivity, and collector distance can all affect the process. Success for MEW printing means fibers fall onto the collector according to their preprogrammed path with predicted fiber diameter. Here, we elucidate how the dynamic relationship between these parameters can converge into ideal printing conditions to achieve highly organized scaffolds.

1. Introduction

A decade has passed since melt electrowriting (MEW) was introduced to the additive manufacturing (AM) community. MEW processes microscale polymer fibers into high resolution and well-organized porous scaffolds, often intended to resemble native tissue architecture. MEW brings a new resolution standard for the printable materials for tissue engineering (TE) applications, especially in the context of using polymers with a history of clinical use. MEW scaffolds have to date been used for cancer research, biofabrication and the TE of bone, cartilage, tendons and muscle [1]. Given the complexity of each tissue and the variability in mechanical and biochemical profiles between them, there is a need to create highly intricate structures tuned to mimic each tissue and its respective native microenvironment. Such complex microstructures can be designed and approximated with MEW because there is fine control over the placement of microscale polymer fibers. The accuracy of fiber placement is dependent on that stability of the jet, which reflects the overall quality of the print. The influential printing parameters can be divided into three groups: 1) those that influence mass flow rate ***to*** the nozzle, namely applied pressure, viscosity of the polymer melt, nozzle size and protrusion; 2) parameters that affect the mass flow rate ***from*** the nozzle, such as applied electric field, molten jet conductivity, and collector speed; and 3) the environmental conditions (ambient temperature and relative humidity) (**Figure 2.1**). Printing parameters have been iteratively studied over the past decade to determine the influence of each individual parameter on the fiber placement and, consequently morphology of the sample. The most important parameters are applied pressure, applied voltage and collector speed [2]. However, the relationship between these parameters has yet to be explored in depth. In addition, and given the wide range of parameters, it is important to understand not only the degree each one

individually influences each part of the printing process, but also how and to what extent these parameters overlap and are interdependent.

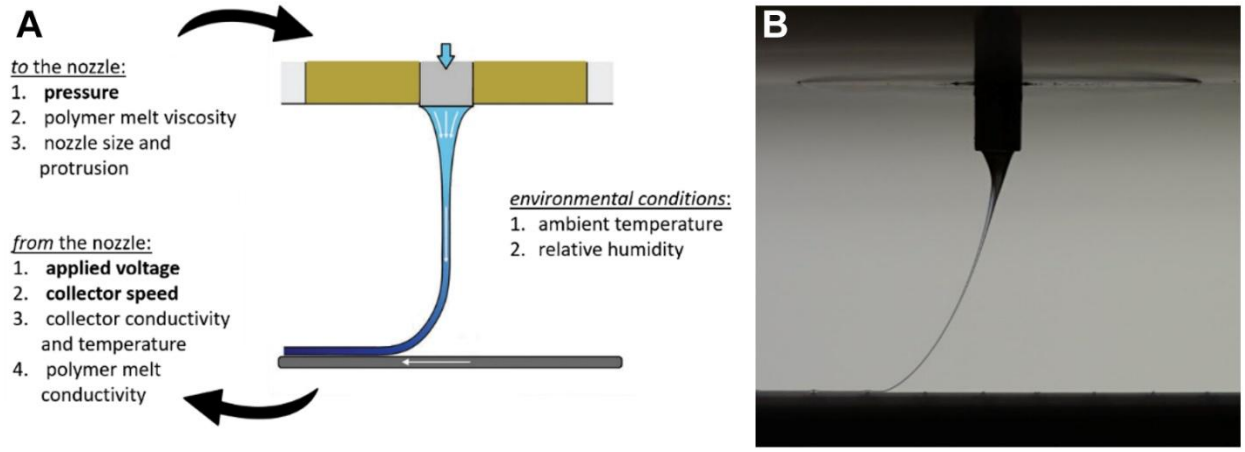

Figure 2.1. Melt electrowriting (MEW) is affected by a range of printing parameters, including those to or from the nozzle, and environmental conditions. The most important printing parameters are applied pressure, applied voltage, and collector speed (noted in bold). A) Adapted with permission from [2] under the terms of the CC BY-NC-ND license. Copyright 2016, The Authors, De Gruyter. B) Reproduced with permission from [1b] under the terms of the CC BY-NC-ND license. Copyright 2019, The Authors, Wiley-VCH Verlag GmbH & Co.

1.1. What is MEW?

MEW is a high-resolution fabrication technique that yields highly porous structures with defined microarchitecture. Similar to melt electrospinning (MES), it is a process where a polymer is heated above its melting point, and a high voltage is applied between a nozzle and collector (**Figure 2.2A**). The distinction between MEW and MES is that parameters are significantly adjusted to prevent electrical instabilities – a feature of electrospinning technique.

The pressure applied to extrude the molten polymer through the nozzle determines the flow rate and a molten polymer drop appears at the nozzle tip. The applied voltage difference forces the

polymer into a conical-shaped jet called Taylor cone (**Figure 2.2B**). Once a stable Taylor cone is formed, the molten polymer forms a thin fiber that falls onto a moving collector (**Figure 2.2C**). The collector speed relative to the polymer flow rate influences fiber placement. At faster speeds, the lag increases, and when the nozzle changes direction, the fiber deposits further from its preprogrammed toolpath (**Figure 2.2D**). At slower speeds, the jet behaves as a mini "liquid rope" that coils (see section on buckling) and accumulates. In addition to the collector speed, the applied pressure, heating temperature and applied voltage also play an essential role during MEW [3]. Learning to balance these three most important parameters provides sufficient control over fiber placement and allows the fabrication of very intricate structures (**Figure 2.2G**). Furthermore, adjusting these parameters during the printing process in real-time allows for high control over the fiber diameter (**Figure 2.2H**). Typically, MEW fiber diameters range from 2 – 50 μm [1b], but sub-micron fibers have been achieved, down to 350 nm [4].

MEW collectors are typically flat and mounted on X-Y linear stages. In recent years, MEW collectors include a cylindrical conformation (rotating mandrel, **Figure 2.2E**), or spherical (**Figure 2.2F**). Achieving the same high resolution on newer conformations is challenging because small changes in jet angle affect the turning point on the curved surface. These difficulties have been overcome for printed tubes (**Figure 2.2I**) and domes (**Figure 2.2J**).

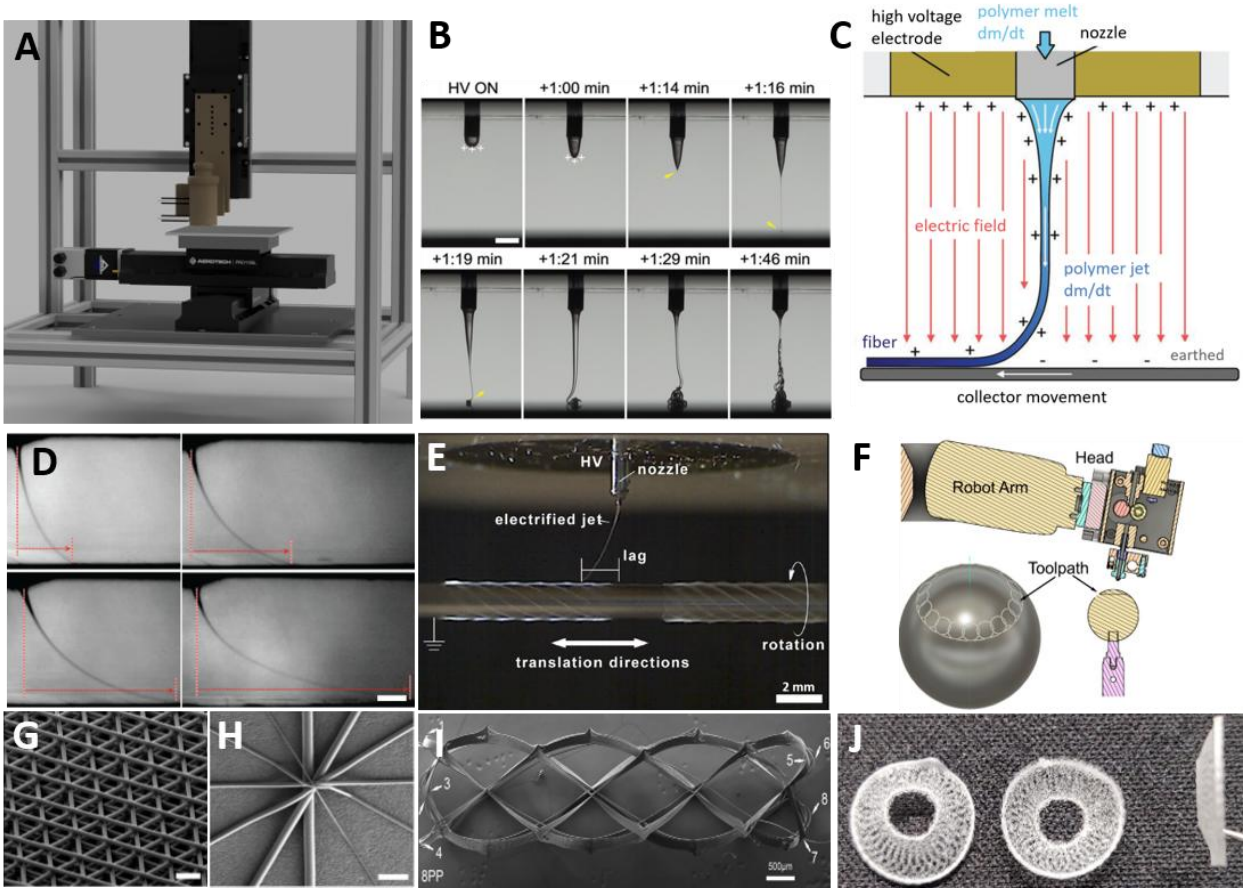

Figure 2.2. Printer configurations and resulting MEW scaffolds. A) MEW setup and its main components. B) Time frames of jet initiation and formation of the Taylor cone: once high voltage is applied to the PCL molten drop charges accumulate at the surface of the liquid closest to the collector. Over time the drop is distorted and the Taylor cone is drawn to the collector [5]. Scale bar: 1 mm. C) A stable jet depends on applied pressure and voltage difference. As the collector moves, a polymer fiber is deposited. The relative movement of the collector is programmed in G-code. D) Images of lag in stable jet that influence fiber placement [2]. Scale bar: 1 mm. E) MEW setup using tubular collector [6]. Scale bar: 2 mm. F) Rendered figure of MEW head attached to a multi-axis robot arm [7]. G) SEM image of a high precision triangular design printed on flat collector [8]. Scale bar: 100 µm. H) SEM image showing control over fiber diameter [9]. Scale bar:

100 µm. I) SEM image of a tube with 8 pivot points printed on tubular collector [6]. Scale bar: 500 µm. J) Photograph of dome scaffold printed with multi-axis robot arm [7]. A) is unpublished, B) Reproduced with permission from [1b] under the terms of the CC BY-NC-ND license. Copyright 2019, The Authors, Wiley-VCH Verlag GmbH & Co. C/D) Reproduced with permission from [2] under the terms of the CC BY-NC-ND license. Copyright 2016, The Authors, De Gruyter; E/I) Reproduced with permission from [6]; F/J) Reproduced with permission from [7] under the terms of the CC BY 4.0 license; G) Reproduced with permission from [8] Copyright 2019, The Authors, Mary Ann Liebert, Inc. publishers; H) Reproduced with permission from [9] under the terms of the CC BY-NC license. Copyright 2018, The Authors, Wiley-VCH Verlag GmbH & Co.

1.2. Background and motivation

MEW can be considered a hybrid of traditional melt extrusion-based 3D printing (i.e., fused filament fabrication (FFF)) and SES. Similar to FFF, a polymer is melt extruded through a nozzle at a temperature above the melting or flow point of the polymer and direct-written onto a collector layer-by-layer. Different from FFF, and similar to MES, a high voltage is applied to the nozzle or collector to induce the polymer into a conical-shaped jet called Taylor cone (**Figure 2.2B**). This yields much thinner fibers than possible with extrusion-based printing. MEW differs from MES in that the jet travels without whipping instabilities, while the low flow rate controls the diameter. Therefore, MEW allows the direct writing of microscale fibers that can be layered upon each other with high fidelity, yielding complex fine-tuned structures with highly organized microarchitectures.

The multi-parametric nature of MEW and the dynamic relationship between the printing parameters directly impact the quality of the print. The point at which the collector speed matches the jet speed is a printing outcome called the **critical translation speed** (CTS) and is the way that

the jet speed can be measured. Below the CTS, the jet buckles as it impinges onto the collector and behaves like a “mini liquid rope”. The CTS and jet speed are determined experimentally with iterative increases in collector speeds until achieving a straight fiber [10].

Another important concept in MEW is **jet lag**. Jet lag is described as the distance between the nozzle position and the point at which the jet falls onto the collector [11]. Defining jet lag anticipates this discrepancy and incorporates this factor into the programmed movement of the collector to achieve correct fiber placement. For an accurate print, the fiber falls onto the collector according to its pre-designed path [2].

Poly(ε-caprolactone) (PCL) is the current gold standard for MEW and has broad appeal due to its low melting point (60 °C) and high thermal stability (up to 160 °C). The temperature for MEW processing of PCL is most commonly 90 °C ± 3 °C [5], although minimizing degradation is most effective at 75 °C. PCL is available in medical grade, which offers improved purity compared to technical grade. The lack of excipients or contaminants in the medical grade PCL not only facilitates clinical translation of MEW scaffolds but also contributes to the reliability and reproducibility of the printing process. Given medical-PC-12 PCL from Corbion (Netherlands) is the most widely studied polymer for MEW, we can more easily extrapolate the conclusions from individual studies and overlap them to elucidate the relationship between the printing parameters.

Throughout this work, we highlight that MEW depends on multiple parameters, and many of the examples provided here are based on PCL. We systematically go through the effect that each of these parameters have on fiber placement and morphology and how the printing parameters can be adjusted to achieve highly organized structures.

2. A MEW handbook: exploring the relationships between processing parameters

This review is intended for new users of MEW printers and overviews the various parameters that affect the process. Visual information acquired during and post-processing is how many users balance the numerous parameters that are required to achieve stable printing. **Table 2.1** therefore provides a selection of videos that are located in supporting information of published articles and may be a valuable starting point.

Table 2.1. Selected videos available for MEW.

Video Description	**Video Info/Hyperlink**	**Reference**
Instructional video on how to perform MEW	Main Video	[12]
Imaging of the jet at increasing collector speeds	Supplemental Video S1	[11]
Adjustments in the collector speed up to and beyond the CTS	Supplemental Video S1	[10]
Electrostatic distortion caused by object on collector	Supplemental Video S1	[13]
Performing MEW onto tubular mandrels	Supplemental Video S4	[14]
Toolpath generation using a multi-axis robot and a MEW filament head	Supplemental Video S1	[7]
MEW scaffold video using a high-resolution electron microscope image	Supplemental Video S1	[15]
A heart valve made from a MEW/hydrogel composite	Supplemental Video S1	[1d]
Biaxial stretching of MEW fibers in an aortic heart valve	Supplemental Video S8	[16]
A MEW fiber reinforced hydrogel in compression	Supplementary Movie 2	[17]
Liquid Crystal Elastomer as a 4D printed material	Supplementary Video S4	[18]

2.1. Voltage difference, applied pressure and collector speed are the most important printing parameters

MEW process depends on multiple printing parameters. Previous studies based on visual analysis of the influence of MEW printing parameters have shown that temperature, high voltage, applied pressure and collector speed are the most important [2, 19]. In this section we explore the dynamic relationship between these and other parameters, and their influence on printing stability and fiber morphology.

The temperature of the polymer melt greatly influences the viscosity of the material, yet this has different effects on the fiber diameter depending on how the PCL is delivered to the nozzle. For air pressure systems, the lower melt viscosity results in more melt extruded to the nozzle and the fiber diameter therefore increases. For piston-driven systems, the melt flow rate delivered to the nozzle is constant irrespective of temperature so the fiber diameter reduces with increased temperature since it is stretched more easily by the electric field [20].

The viscoelastic properties of the polymer are particularly relevant in MEW because they influence fiber placement, reflecting the overall quality of the resulting scaffold. The ideal printing temperature for PCL is 75 °C, where it is more fluid than its melting temperature of 60 °C. PCL has been thoroughly studied and is by far the most used polymer in MEW processing. Limiting the variance of temperature fluctuation ± 3 °C facilitates the extrapolation towards transversal application of varying printing parameters for MEW.

2.1.1. Varying voltage affects fiber diameter

In MEW, a voltage difference is applied between the nozzle tip and collector to prevent Rayleigh-plateau instabilities and establish a Taylor cone [21]. Voltage differences in MEW usually

range from 4 to 5 kV [9]. At a threshold voltage, the jet is stabilized, allowing for a sustained continuous print at very low flow rates [1c]. Below this value, continuous jets/fibers can result however they will periodically change in diameter in a phenomenon termed "fiber pulsing"[2]. Maintaining a sufficient electric field is typical, however, increasing the electrical field during the printing process is useful to maintain jet stability and produce thinner fibers with increasing scaffold height [14]. The thickest of samples require increases in voltage and collector distance to keep accurate printing with more layers [22].

To initiate a jet, a lower initial voltage difference is applied and fiber pulsing is checked by looking at the repeated turns. Then, throughout the printing process, the voltage difference may be increased within the working range. A higher voltage difference reduces the jet angle which results in increased CTS and reduced jet lag [12, 19]. A higher CTS and reduced jet lag translate to faster prints with improved fiber placement. Even within the working range of voltage difference, an accumulation of charges may cause an electrical discharge known as arcing. Arcing interrupts the jet and compromises the stability of the printing process and the equipment and must be avoided.

2.1.2. Switching voltage polarity changes the jet speed, but not the diameter

One of the initial decisions when establishing MEW is whether to use positive or negative applied voltage and whether to apply it to the nozzle, collector or both. A study within the doctoral thesis of Dr Andrei Hrynevich [23] (in the wider context essential reading for new users of MEW) investigated what happened when different applied voltages were applied to both the nozzle and the collector. From a fiber diameter and morphology perspective, the applied polarity did not influence the outcome. However, a negative voltage applied to the nozzle and positive polarity applied to the collector resulted in a significantly slower jet. The CTS was measured at 320 mm/min and 240 mm/min for positive/negative and negative/positive polarity respectively [23].

Recently Lu *et al.* found that different ground/applied voltage configurations do not affect the fiber or the jet speed of PCL [24]. This does not discount the possibility that effects of voltage configuration may perhaps manifest when printing in different circumstances or with different materials. Different polarities used with bioactive glass/PCL were inconclusive [25] and while more information is needed, the decision on where to apply the voltage should be based on whether this would be harmful for the electronics of the device.

2.1.3. Varying pressure affects fiber diameter

Air or nitrogen pressure is normally applied to extrude the molten polymer through a nozzle, typically from 0.5 to 4 bar [9]. Applying a higher pressure increases the polymer's flow rate. Intuitively, by increasing the flow rate, the diameter of the resulting fiber increases (**Figure 2.3B**). Therefore, adjusting the pressure may be used to control fiber diameter. However, a change in diameter caused by varying applied pressure require a stabilization phase in the matter of seconds or minutes since the diameter change is not instantaneous [9]. As discussed later, the nozzle diameter is a simple parameter that can be adjusted between printing and significantly affects the melt flow to the tip.

A change in applied pressure also affects CTS. Specifically, at higher pressure, the CTS is lower [9]. This decreases the speed at which ideal prints can be achieved. Given the limitations of varying pressure to adjust fiber diameter, it is important to focus on other parameters. For example, varying collector speed has an almost immediate effect on fiber diameter. Fiber diameter can be digitally controlled by changing pressure and collector speed without changing applied voltage [9].

2.1.4. Varying collector speed affects fiber diameter and fiber placement

Collector speed can have an almost immediate effect on fiber diameter and placement. Typical collector speeds for MEW range from 4.5 to 92 mm/s [1b] although studies have been performed at much higher collector speeds up to 167 mm/s [9]. If the collector speed is increased to match that of the jet, a straight fiber forms at this so-called CTS. Typical CTS for MEW scaffolds range from 5 to 12.5 mm/s [9]. Finding and maintaining CTS throughout the print is important for accurate fiber placement. If the printing speed is below CTS, the polymer fiber buckles and even accumulates onto the collector as a periodic or sinusoidal pattern instead of straight lines [2]. This phenomenon is called fiber buckling (**Figure 2.3I**) (see section on buckling). Fiber buckling may be avoided by increasing the collector speed [2]. The most accurate fiber placement occurs by maintaining the collector speed at or slightly above CTS [9] but even at this point, there is mechanical stretching of the fibers. Further increasing the collector speed also increases jet lag, which decreases printing fidelity when the nozzle changes direction [11]. Therefore, even though higher speeds allow the formation of thinner fibers, using collector speed alone to adjust fiber diameter compromises the fiber flight path because this increases the potential offset compared to the preprogrammed path. Achieving correct fiber placement is especially relevant when changing printing direction (**Figure 2.3I**) [11].

With expanding design complexity in MEW structures, recent studies have found that in printing circular scaffolds, there is inherent tilting of the fiber walls inwards (**Figure 2.4C**) [10, 26]. The inwards tilting of the walls can be corrected with slight 6 μm layer shifts in amplitude in an approach termed microscale layer shifting. Further, and more relevant to using collector speed as a parameter to improve fiber placement, the resolution of circular structures increases when printing slightly below CTS [10]. This sub-CTS printing for sinusoidal tool paths occurs without

buckling, likely as there are stresses that result from naturally inward fiber wall tilting and the slower jet speed provides "slack" in for improved positioning.

Taken together, we appreciate that the ideal collector speed is highly dependent on the CTS, but the collector speed relation to the CTS is itself dependent on the structure being printed: when printing the first layer of a scaffold or a tall straight wall, the ideal collector speed is slightly above CTS; when printing circular arcs, the ideal collector speed is slightly below the CTS.

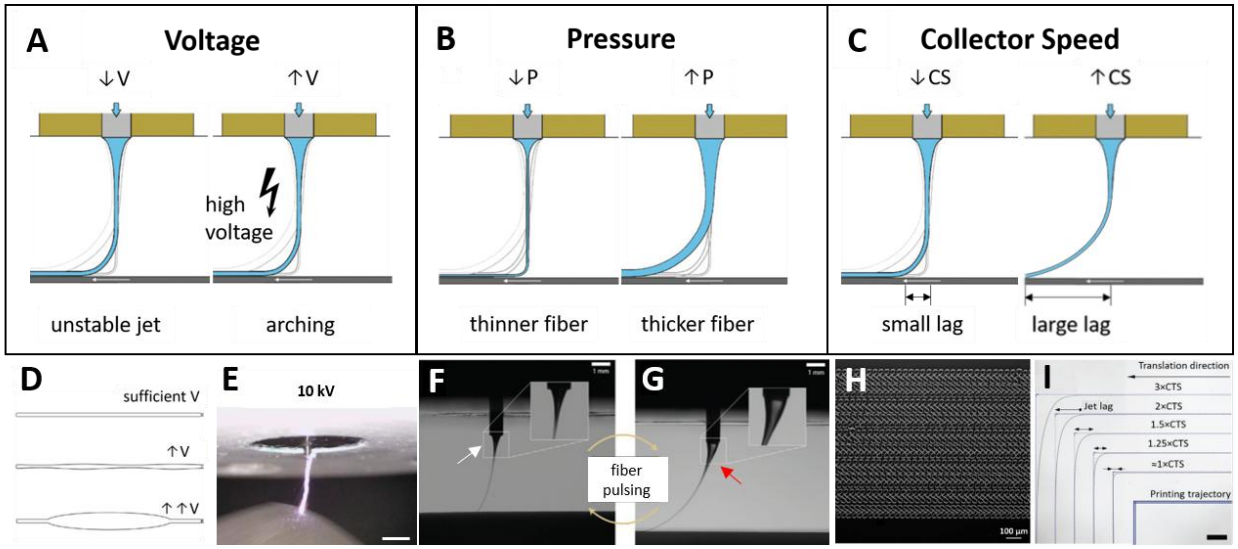

Figure 2.3. The quality of MEW scaffolds is mainly dependent on A) voltage, B) pressure, and C) collector speed. Adapted from [2]. D) At low voltage, the jet is unstable (fiber pulsing) [2] while E) high voltage causes arcing and consequently, an interrupted jet. E) At high voltage, there is a discharge in the form of arcing. Scale bar: 2 mm [27]. F-G) Varying P causes fiber pulsing. F) White arrow points to ideal Taylor cone volume. G) Red arrow points to excessive Taylor cone volume which will cause fiber pulsing. Adjusting pressure allows control over fiber diameter with great precision [14]. H) If collector speed is slower than the jet speed, the jet will form buckle and form coils. I) If collector speed is too high, the jet will cut corners relative to programmed path when changing direction. At CTS, we have some of the most accurate fiber placement. Scale bar:

1.5 mm. [11] Reproduced with permission. A-D, H) Adapted with permission from [2] under the terms of the CC BY-NC-ND license. Copyright 2016, The Authors, De Gruyter. E) Reproduced with permission from Saidy et al. under the terms of the CC-BY license. Copyright 2020, The Authors, Frontiers. F/G) Reproduced with permission from [1b] under the terms of the CC BY-NC-ND license. Copyright 2021, The Authors, Wiley-VCH Verlag GmbH & Co. I) Reproduced with permission from [11] under the terms of the CC BY-NC-ND license. Copyright 2020, The Authors, Wiley-VCH Verlag GmbH & Co.

2.2. Other parameters

2.2.1. Charge buildup affects fiber placement

The semi-conductive nature of the polymer melts printed with MEW results in entrapped charges within the scaffold, and these charges exert significant forces between the sample and the jet. Charges can destabilize the fiber path trajectory of the positively charged polymer melt as it is extruded through the nozzle. The poorly conductive polymer does not completely discharge as it falls onto the collector causing each fiber to be repelled by the previously deposited fiber.

From a different perspective, charges can cause the jet to be attracted to the previously deposited fiber. Referred to as an "autofocusing effect", this attraction naturally favors stacking of MEW fibers into walls. Inherently, this phenomenon limits the minimum fiber spacing between existing neighboring fibers [11, 28]. The term given to when fibers are deviated from their preprogrammed path towards an existing fiber is fiber bridging (see section on fiber bridging). Interestingly, the conductive nature of the collector influences the jet path: if the substrate is conductive, the newly printed fiber tends to be attracted by the pre-existing one, whereas if the substrate is non-conductive, the new fiber is repulsed and steered away from the pre-existing fiber [28b].

As the scaffold height increases with every layer, there is a charge buildup which affects CTS and jet lag (**Figure 2.4A-C**), consequently compromising fiber path. Therefore, with increasing scaffold height, the likelihood of fiber bridging increases. Specifically, increasing the number of layers from 1 to 10 layers increases the minimum inter-fiber distance without fiber bridging approximately two-fold [28a].

2.2.2. Varying collector distance affects fiber placement and jet angle

In MEW, the typical distance between the nozzle tip and collector surface is 3.5 - 6 mm [9-10]. Studies using PCL have shown that increasing the collector distance from 3 to 7 mm causes a slight decrease in fiber diameter [29]. As the height of the scaffold increases with each deposited layer, varying the distance between the print head and collector may be used to influence the flight path and morphology. Increasing the distance in the z axis forces the fiber to travel a longer distance and the polymer will solidify before it reaches the previously deposited fiber. Increasing the distance from the print head to the collector can also promote the correct layering of fibers by eliminating fiber merging/fusion, while compromising perfect fiber placement. The successful iteration of correct fiber placement allows the creation of fiber walls. Adjusting the distance between the nozzle and collector may also be necessary if the fiber does not correctly attach to the collector. In this case, a large polymer droplet is dragged along the collector. To correct this, the z distance may be decreased. Alternatively, the collector may be heated to promote the droplet attachment onto the collector. However, there is a risk of the fibers partially melting onto the collector, displaying an unsolicited flat morphology called fiber embossing [9].

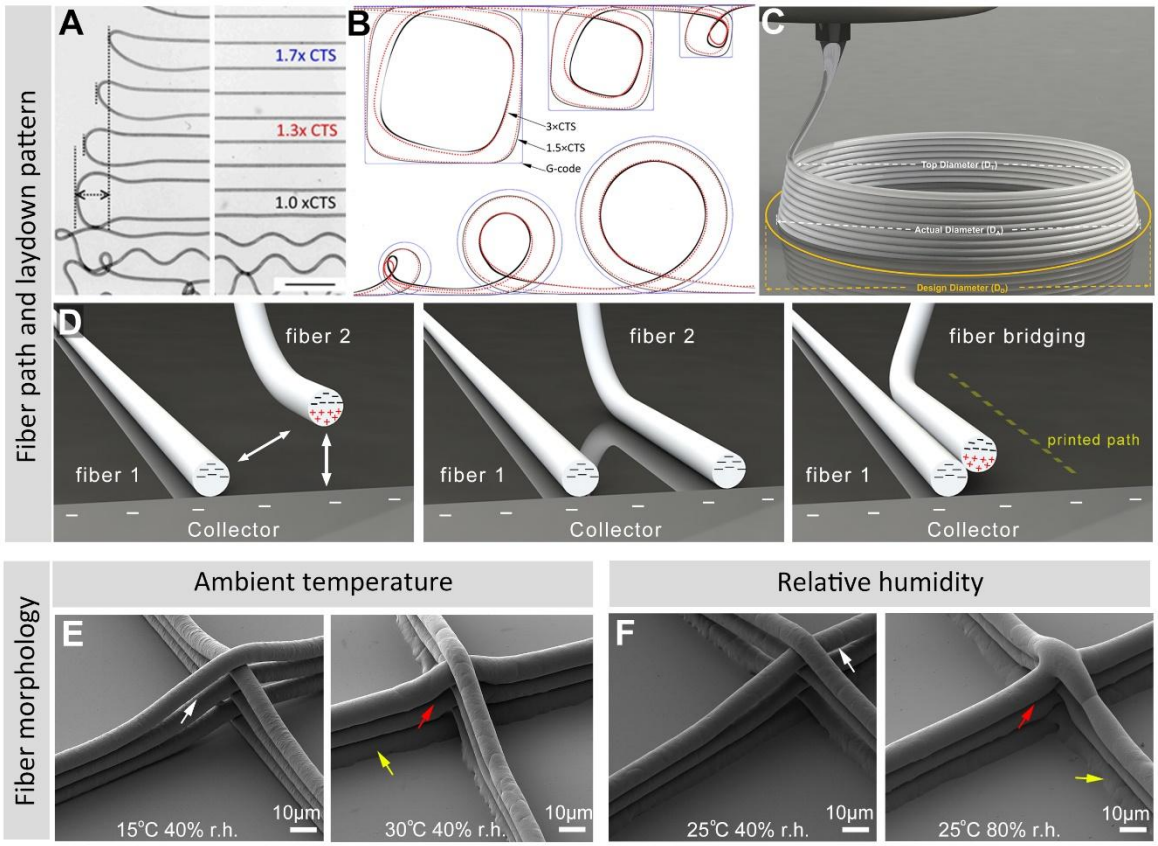

Figure 2.4. MEW fiber placement and morphology. Relationship between collector speed and jet lag influences MEW fiber path and laydown pattern. A) Ratio of collector speed and jet speed determines CTS [2]. Scale bar: 1 mm. B) Rendered image showing printing above CTS causes changes in laydown pattern compared to programmed path [11]. C) Rendered image showing fiber path changes on circular multilayered constructs: walls tilt inwards [26]. D) Rendered image showing charge buildup causes a deflection in the fiber path. A second fiber is attracted to the previously deposited fiber, leading to fiber bridging. Fiber morphology is affected by ambient temperature and relative humidity [23]. Increasing E) ambient temperature or F) relative humidity causes fibers to stack closer together (white arrows compared to red arrows) and fiber embossing (yellow arrows) [23]. Scale bars E) and F): 10 μm. A) Reproduced with permission from [2] under the terms of the CC BY-NC-ND license. Copyright 2016, The Authors, De Gruyter. B) Reproduced

with permission from [11] under the terms of the CC BY-NC-ND license. Copyright 2020, The Authors, Wiley-VCH Verlag GmbH & Co. C) Reproduced with permission from [26] under the terms of the CC BY license. Copyright 2020, The Authors, Wiley-VCH Verlag GmbH & Co. D) Reproduced with permission from [28a] under the terms of the CC BY license. Copyright 2021, The Authors, Wiley-VCH Verlag GmbH & Co. E/F) Reproduced from [23] under the terms of the Creative Commons Attribution 4.0 International License (CC BY 4.0).

2.2.3. Collector conductivity affects uniformity of fiber morphology and fiber spacing

To create a voltage difference between the print head and the collector, the collector must be grounded. A highly conductive collector can be uniformly grounded, eliminating any gradient that might influence fiber path. Interestingly, the conductivity nature of the collector may influence the polarity of the resulting scaffold: opposite charge polarity was observed between scaffolds printed onto a conductive and non-conductive surface [28b].

In some cases, the MEW printer can be modified to have a heated collector. This is particularly useful for MEW processing of higher melting point polymers where the jet does not adhere to the collector as they solidify, for example PVDF [5]. By heating the surface, the fiber adheres to the collector allowing correct fiber placement. However, this may result in melting of the first layer onto the collector, as well as fiber fusion between iterative layers. Either of these occurrences may compromise the integrity of a multilayered structure as it is being printed layer upon layer. Respecting the need for a highly conductive and lightweight material, most MEW collectors are made from aluminum.

2.2.4. Nozzle size and nozzle protrusion affects fiber diameter and fiber placement

Each nozzle provides a range of fiber diameters [30] and smaller diameter nozzles will yield smaller diameter fibers. In MEW, a 22G-nozzle is most common, yet studies have been successful using much smaller nozzles (33G) [1b]. Achieving smaller diameter fibers by decreasing nozzle size should be approached with caution because it is not uncommon that smaller diameter nozzles clog. This interrupts the jet and compromises the quality of the print. This issue can be bypassed by using medical grade materials which offer higher purity compared to commercially available polymers. This reinforces the importance of using pure grade polymers. Not only do medical grade polymers translate better into clinical settings, but also facilitate the printing process, which in turn reflects the quality of the print. Nozzle protrusion usually ranges from 0.5 – 2 mm [28c, 31]. No systematic efforts have been published to date to examine the effect that nozzle protrusion may have on fiber placement or morphology. However, a greater protrusion of the nozzle is expected to cool the melt at the tip, locally increasing the viscosity and therefore flow rate. Excessive protrusion will cause the melt to solidify.

2.2.5. Ambient temperature and relative humidity affect fiber diameter and morphology

The environmental conditions of MEW influence fiber diameter and fiber morphology. Given that MEW printers are ideally enclosed, the temperature and relative humidity are kept stable and can easily be monitored using a weather station. Typical values for ambient temperature and relative humidity are 21±2 °C and 40±10%, respectively [14]. As shown in **Figure 2.4E**, increasing the ambient temperature from 15 to 30 °C reduces the spacing between stacked fibers (white arrow compared to red arrow) and causes the first deposited fiber to melt onto the collector, yielding a flat morphology (yellow arrow). In the same study, similar changes in fiber stacking and morphology were observed when increasing the relative humidity from 40 to 80% while

maintaining the ambient temperature constant (**Figure 2.4F**): the spacing between stacked fibers was also reduced (white arrow compared to red arrow) and the first fiber also showed a flat morphology (yellow arrow)[23]. Due to the iterative layer-upon-layer nature of MEW, the fiber stacking and morphology will inevitably affect the overall quality of the print. Therefore, it is important to monitor and maintain a constant ambient air temperature and relative humidity.

Ambient temperature and relative humidity have also shown to affect the ability to suspend fibers. Specifically, an increase in ambient temperature from 20 to 24 °C resulted in 50% reduction in cumulative length of suspended fibers [31]. This study proves that a small variance in ambient temperature can dramatically affect the ability for the fiber to suspend larger gaps.

Previous studies that explored the effect of varying ambient temperature and humidity on MES demonstrated contradicting conclusions to what has recently been shown for MEW. Changes in temperature during MES had only moderate effects on the resulting fibers, whereas changes in relative humidity compromised both fiber morphology and critical speed of the collector [32]. A more recent study claimed that relative humidity did not play a significant role in inter-layering fiber ordering, nor did it affect fiber diameter consistency or fiber surface morphology [33]. The fact that this difference exists within MES emphasizes that it is distinct from MEW, even though the two techniques have identical configurations.

2.2.6. Varying polymer melt temperature affects ability to suspend fibers

Fibers that span airgaps between structures already on the collector is a feature of MEW but is highly dependent on certain parameters. For example, the typical printing temperature for PCL is 90 ± 3 °C [5], but lower temperatures are more appropriate to deliberately suspend fibers. The heating temperature was found to greatly influence the ability to suspend fibers between supporting

walls ranging up to 9 mm apart. At temperatures greater than 90 °C, almost no suspended fibers were found on the test sample. At 75 °C, the lowest printing temperature attempted for this study, almost half of the suspended fibers were observed [31].

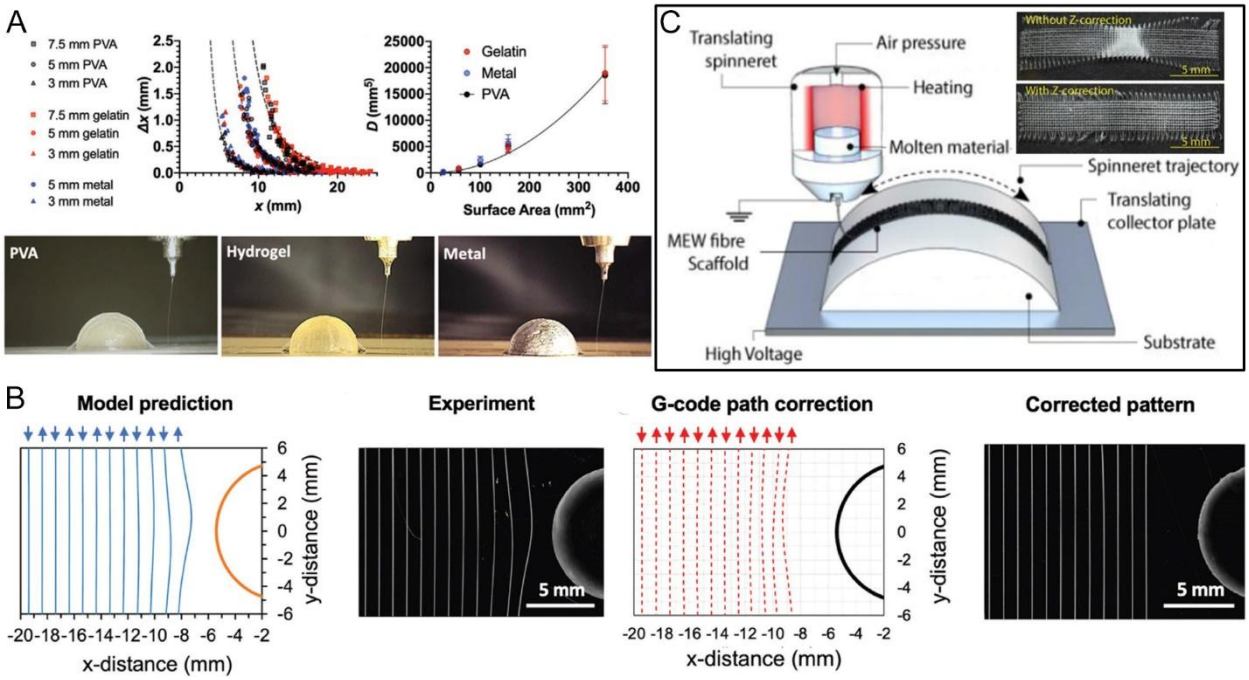

Figure 2.5. Effect of existing shapes on the collector surface. A) Different materials with the same dimensions and similar charge dissipation deflect the MEW jet to similar degrees. B) When the toolpath is adjusted for this, the intended pattern can still be generated. C) Changing the Z-axis to maintain the collector distance can correct distortions in the print that can occur onto an existing shape. A) Reproduced with permission from [13], Copyright 2021, The Authors, Wiley-VCH Verlag GmbH & Co. B) Reproduced with permission from [35] under the terms of the CC BY license. Copyright 2020, The Authors, Wiley-VCH Verlag GmbH & Co.

2.2.7. Direct writing onto existing features

In certain instances, non-planar shapes are important for biofabrication including dome-shapes [13], apexes [34] and undulating surfaces [27]. These shapes are attained by increasing the degrees of freedom for the print head by using a multi-axis robot (**Figure 2.2F**) [7] or placing an object (a feature) onto a flat or tubular collector [13, 27, 35]. **Figure 2.5** shows that while these structures can distort the electric field, this can be adjusted for in the tool path to achieve a predictable printing outcome. These features can be dissolvable so that, once the print has been made, the feature is removed and the MEW structure obtained [36].

2.3. Troubleshooting

Appreciating that MEW is a multi-parametric processing technology, choosing and adjusting towards correct printing conditions is a skill to master and achieve a stable jet with predictable laydown, which determines the regularity of the scaffold. In addition, there are important jet/fiber characteristics to observe and avoid, to obtain an ideal outcome.

2.3.1. Fiber pulsing

Fiber pulsing is when there is a change in fiber diameter along its length, periodically occurring up to minute intervals. This variation in fiber diameter can be traced back to an imbalance in the electrical field. A non-uniform electrical field during printing causes a change in jet volume resulting in periods where the polymer accumulates as it falls irregularly onto the collector. Reducing flow rate by nozzle diameter or applied pressure will reduce fiber pulsing, as will increasing collector speed or applied voltage to increase the drawing capacity of the jet. Fiber pulsing worsens with multiple layers because previously deposited fibers diminish the electric field

and reduce its influence on the jet. Increasing the voltage difference between nozzle and collector can help stabilize the jet and correct fiber pulsing [2, 14].

2.3.2. Fiber buckling

Fiber buckling occurs when there is an excess of polymer being deposited onto the collector yielding a "liquid pattern" instead of a straight line. To avoid this, the melt temperature or applied pressure could be decreased (consequently decreasing the polymer flow rate). A much simpler alternative to correct fiber buckling would be to increase the collector speed to match or stay slightly above CTS [2]. When printing with circular arc toolpaths, using collector speeds just below the CTS makes favorable structures [10].

2.3.3. Fiber embossing

Fiber embossing occurs when the first fiber which falls onto the collector displays a flat morphology [6, 9]. The underneath of the first deposited fiber displays a flat morphology because the molten polymer jet arrives at the collector surface before it completely solidifies and melts onto the collector. This phenomenon may be corrected by adjusting printing parameters that will allow the polymer to solidify before it reaches the collector. Approaches to avoid fiber buckling include decreasing the ambient temperature or relative humidity (**Figure 2.4E-F**), or by increasing the collector distance.

2.3.4. Fiber fusion

Fiber fusion refers to the extent of melting that occurs when two or more fibers stack upon or intersect with each other. It is arguably the most important aspect of MEW that has not been systematically correlated to processing parameters, since the extent of fiber fusion is expected to

significantly affect the mechanical properties. It reflects the state of the jet at deposition and increases when the jet path is short, or the temperature of the collector is too high. While possible to speculate on the various parameters that induce fiber fusion, a comprehensive fiber fusion remains to be performed.

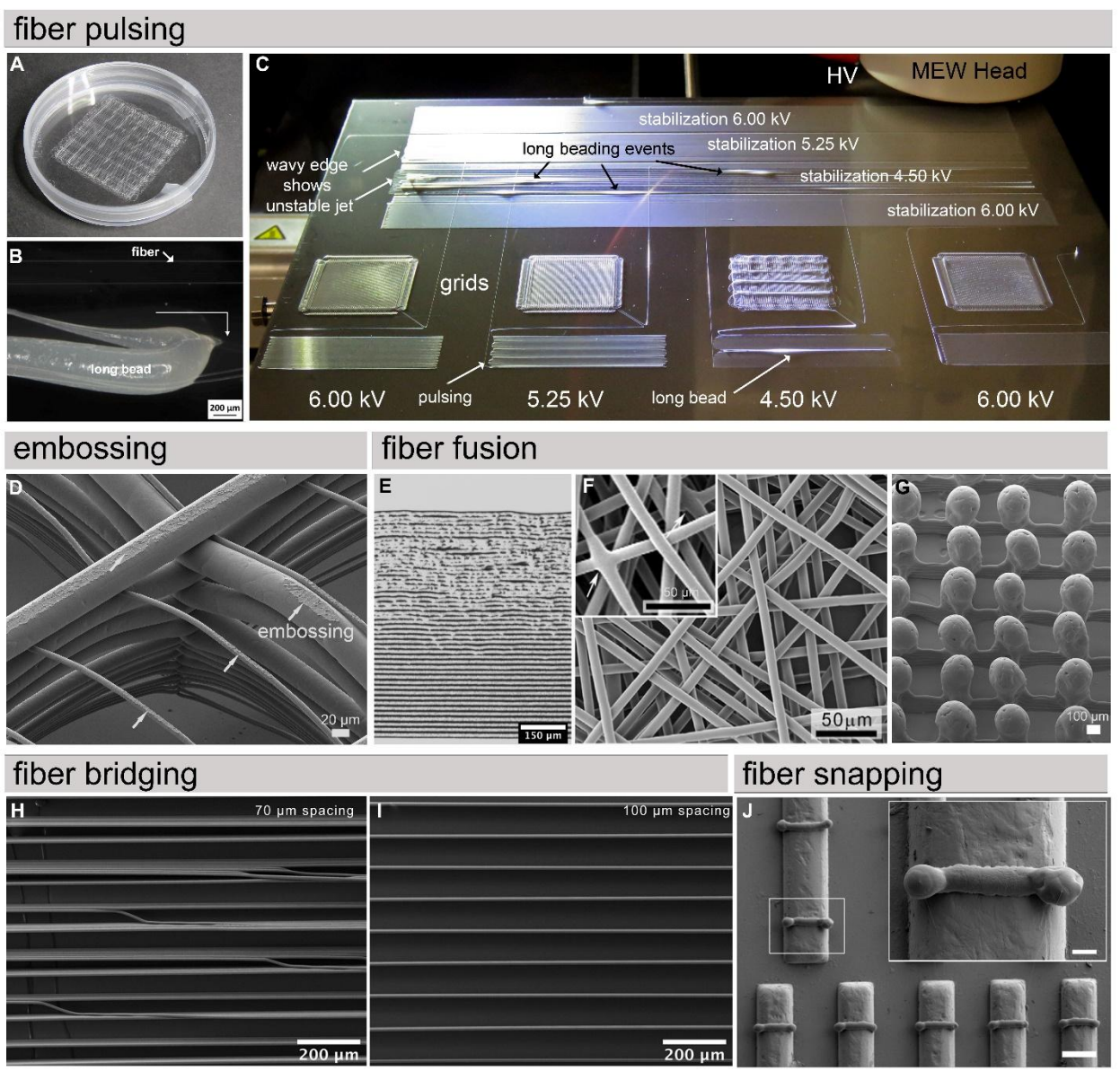

Figure 2.6. Printing outcomes that may require troubleshooting. A-C) Fiber pulsing is a common and typically undesired printing outcome where the flow rate to the jet does not match the volume

of the fiber being deposited. D) Embossing results when there is some flattening of the fiber. E-G) Fiber fusion can manifest in different circumstances with different outcomes. H-I) Fiber bridging occurs when fibers are placed close together and J) snapping of the fiber can sometimes be seen or induced. A-C) Reproduced with permission from [2] under the terms of the CC BY-NC-ND license. Copyright 2016, The Authors, De Gruyter. D) Reproduced with permission from [9] under the terms of the CC BY-NC license. Copyright 2018, The Authors, Wiley-VCH Verlag GmbH & Co. E) Reproduced with permission from [1b] under the terms of the CC BY-NC-ND license. Copyright 2021, The Authors, Wiley-VCH Verlag GmbH & Co. F) Reproduced with permission from [37] with permission. Copyright 2013, IOP Physics, G) Reproduced with permission from [38] under the terms of the CC BY-NC license. Copyright 2021, The Authors, Wiley-VCH Verlag GmbH & Co. H-I) Reproduced with permission from [28a] under the terms of the CC BY license. Copyright 2021, The Authors, Wiley-VCH Verlag GmbH & Co. Reproduced with permission from [39] under the terms of the CC BY license. Copyright 2021, The Authors, Wiley-VCH Verlag GmbH & Co.

It is known, however, that fiber fusion can occur with increased number of layers – this has been seen when imaging the fiber wall (**Figure 2.6**). It is expected to be related to the crystallization kinetics of the polymer used, exemplified in **Figure 2.6** in an extreme case when PVDF forming "drops" at higher layers is used in addition to a heated collector. Moreover, fiber fusion decreases the overall construct height compared to the expected scaffold design [26]. Therefore, it is important to consider fiber fusion and determine from the outset whether this is a desired or unwanted property in the printed structure.

2.3.5. Fiber bridging

The accumulation of charges during MEW leads to an autofocusing effect of fibers towards previously existing fibers on the collector [40]. This autofocusing effect limits the distance at which fibers can be positioned in parallel onto a collector. The minimum inter-fiber distance without fiber bridging depends on fiber diameter: single fibers with diameter of 5 or 15 μm have a minimum inter-fiber distance without fiber bridging ranging from 33 to 62 μm, respectively. Increasing the number of layers to ten increases this minimum inter-fiber distance approximately twofold for the respective increasing fiber diameters [28a].

2.3.6. Fiber snapping

MEW is an inherently continuous process and normally an interrupted jet is not desirable because this destabilizes the jet conditions and a new stabilization period is required. Therefore, to reestablish a correct and continuous jet once it breaks, the print must be interrupted, and the scaffold is often discarded. To avoid fiber snapping, it is important to monitor and maintain printing conditions that favor a continuous jet, including stable ambient temperature and relative humidity, a high voltage, and a constant collector speed close to or slightly above CTS [9].

Even though a discontinuous print is not desirable for MEW, micro-fragments with defined morphology could have interesting applications within the fields of AM and TE. For example, short polymer fragments may be used to reinforce hydrogel materials that induce bioactive response from cells [41]. Therefore, an interest has shifted towards using MEW to produce micro-fragments. By maintaining an elevated ambient temperature of 36 °C and high relative humidity of 60% that favor the breaking of the jet, micro-fragments with controlled fiber length were printed onto a microrelief substrate [39].

2.3.7. Microscale layer shifting

An accumulation of charges during MEW creates an autofocusing effect of fibers as they fall onto the collector. This process favors the vertical stacking of fiber layers, yielding straight fiber walls [28a]. When attempting to print multi-layered structures of circular nature, there is inherent tilt in the walls (**Figure 2.4C**) [26]. Recently, however, the formation of tilted walls has been achieved through deliberate offset of the printing trajectory in a process is called microscale layer shifting [40]. An inward and outward tilting allowed the creation of sinusoidal fiber walls with tunable mechanical properties. Tuning the mechanical properties to achieve a given maximum displacement when stress or strain is applied to the tilted walls is an interesting aspect for biomedical applications. This study achieved substantial layer shifting up to a horizontal geometry, proving the capabilities of MEW for innovative designs which can be directed towards a wide range of applications.

3. Miscellaneous Aspects

Controlling the printing parameters during MEW enables the creation of complex and intricate microstructures. Even within a decade of its development, very different approaches have been presented to explore the capabilities of MEW from an unorthodox perspective. This section focuses on the different angles taken on the technology, including hollow fibers, selective dissolution, surface coatings and expanding to the use of aqueous systems to printing living systems.

3.1. Core-shell MEW printing

Iterations on the printer design opens new possibilities for MEW. Recently, the MEW printer head has been tailored to introduce a conventional nozzle into a custom design coaxial system.

The inner core nozzle introduces air into the molten polymer during the print, yielding hollow fibers (**Figure 2.7A**) [42]. The coaxial approach may be further developed to print core-shell fibers of different materials. Some printing parameters may independently change, namely applied pressure, or melt temperature. However, the temperature at which the polymers are printed must be similar as to avoid unplanned melting of one of the phases that would compromise the fiber morphology.

3.2. Sacrificial inks

Similar to a coaxial setup where two polymers may be introduced into the nozzle and printed simultaneously, a polymer blend may be heated homogeneously and melt electro written into thin fibers. However, instead of maintaining the bulk polymer fibers, one of the polymer phases may be selectively dissolved. In a recent study, polymer phase separation was incorporated into MEW to yield highly aligned nanofibrils that mimic native collagen (**Figure 2.7B**) [43].

The same sacrificial approach may also be applied at a larger scale. PCL scaffolds printed with MEW were used to create pores within a hydrogel mesh. The PCL template was sacrificed to yield interconnected pores with microscale diameters. The resulting structures have interesting applications as cell scaffolds with tunable diffusion rates [44].

3.3. Coating of MEW scaffolds

MEW scaffolds can be manipulated post print to improve their surface properties. For example, PCL scaffolds were coated with star-shaped PEG macromer that forms a hydrogel which minimizes unspecific interactions with proteins and cells [45]. This permanent hydrogel coating can be used to covalently attach biomolecules such as collagen. **Figure 2.7C** show a homogenous collagen distribution on a PCL scaffold after successful functionalization.

Surface modifications may be introduced via precipitation techniques. For example, inorganic coating of MEW scaffolds with calcium phosphate introduces nanotexture to the surface of PCL fibers without changing the resultant fiber diameter when compared to non-treated scaffolds (**Figure 2.7D**) [46]. The nanotopography increases the surface area, promoting cell adhesion, which is important from a biological perspective.

Adding hydrogels to aligned fibers provides a soft environment for cell growth due to their high-water content. MEW has been used as a frame for the development of a 3D electrophysiological platform without interfering with cell measurements [47]. In addition to the advantages from a biological perspective, combining MEW scaffolds with hydrogels increases the mechanical stiffness of the scaffold/hydrogel composite by up to 54-fold compared with either of its individual components [17].

3.4. MEW with materials other than PCL

In recent years, there has been an increase in MEW processing materials other than PCL, however the parametric relationships follow similar trends. One of the first examples is a class of hydrophilic polymers called poly(2-oxazoline)s (POx). Interest in POx stems from its capability to solve drugs coupled with a thermoresponsive profile. An in depth study on the effect that each printing parameter had on the processability of a type of POx called poly(2-ethyl-2-oxazoline) (PEtOx), revealed that the temperature of the polymer melt had dominating influence, while keeping constant pressure, voltage difference and collector distance [29]. Given POx can store functional proteins that mimic natural biomolecules, POx scaffolds can be used for drug delivery platform in the future.

The piezoelectric properties of poly(vinylidene fluoride) (PVDF) have many interesting biomedical applications including use in flexible electrodes or sensors. The printing parameters to process PVDF with MEW were explored thoroughly (over 50 combinations) to yield scaffolds with small diameter fibers (17-55 μm) and confirmed electroactive phase [48].

Polypropylene (PP) has increased long term stability and stronger mechanical profile when compared to PCL. Increased stability and strength are attractive properties for medical devices. To enable MEW processibility with PP, several printing parameters were explored (namely collector speed, temperature and melt flow rate to the nozzle) and optimized to yield small diameter fibers (as small as 16.4 μm). This study highlighted that a heated collector was critical for the fiber to successfully adhere to the collector. Specifically, for the correct placement of PP fibers, the collector had to be heated above 70 °C [49].

A different class of polymers, namely thermoplastic elastomers, have also been successfully processed with MEW. Printing parameters that included applied voltage, temperature, and feeding pressure were optimized to process poly(urea-siloxane) into small diameter fibers ranging from 10 to 20 μm with accurate stacking of up to 50 layers [50]. More recently, poly(L-lactide-co-ε-caprolactone) (PLCL) was also printed with MEW. PLCL is more elastic and has a faster degradation rate when compared to PCL. One of the major limitations to MEW PLCL is its high melting temperature, which was resolved by pre-treating the polymer. After maintaining PLCL at 150 °C for at least 24 hours, scaffolds were printed at a working temperature of 110 °C with small diameter fibers (14 - 40 μm) [51]. Further, this study showed that PLCL of higher molecular weights had improved physical and mechanical stability with tunable degradability and mechanical profiles.

Adapting MEW to different polymers has brought a shift towards using these intricate scaffolds towards biomedical applications. For example, the thermosensitive polymer poly(L-lactic acid) (PLLA) has been successfully processed with MEW for applications in bone TE. Printing parameters including applied voltage, collection speed, and flow rate were optimized to yield fibers with 40 μm diameter and scaffolds with pore size of 200 μm [52]. The resulting scaffolds fabricated with high deposition accuracy and crystallinity have *in vitro* potential for bone regeneration. Copolymer approaches have also been explored within MEW to mimic ligaments and tendons. Specifically, poly(L-lactide-*co*-ε-caprolactone-co-acryloyl carbonate) (p(LLA-*co*-CL-*co*-AC)) and poly(ε-caprolactone-co-acryloyl carbonate) (p(CL-co-AC)) were synthesized and printed into sinusoidal pattern with mechanical properties similar to that of the toe region [1e].

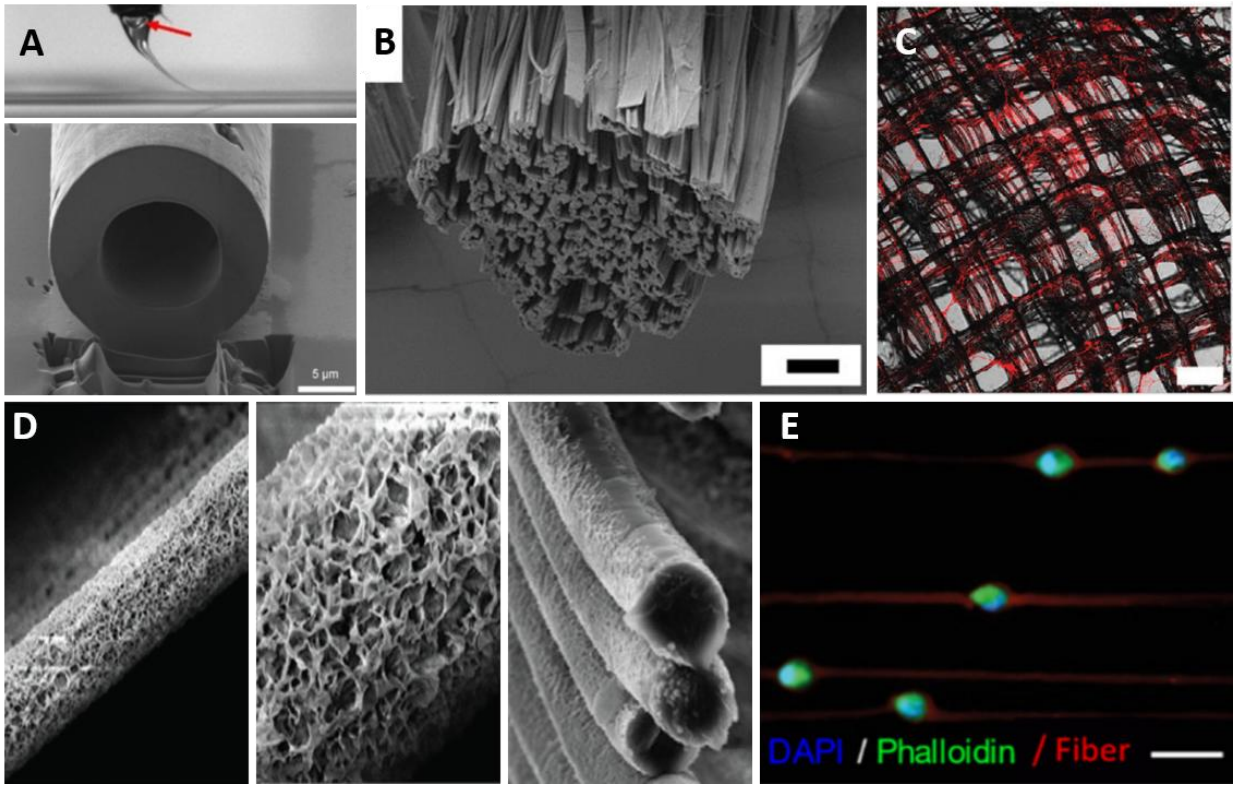

Figure 2.7. Fiber structures and coatings within MEW. A) Coaxial nozzle system produces hollow fibers when air is pushed into the central nozzle [42]. Red arrow points at air in Taylor cone. Scale bar 5 µm. B) Aligned nanofiber microbundles after dissolution of a matrix polymer blend [43]. Scale bar: 10 µm C) Collagen-functionalized PCL scaffolds highlighted through red staining [45]. Scale bar 200 µm. D) Inorganic coating of MEW scaffolds with calcium phosphate changes surface morphology [46]. Scale bars 10 µm, 5µm and 10 µm. E) Cells incorporated within aqueous-based inks [53]. Scale bar 20 µm. A-B) Reproduced with permission from [42]. Copyright 2021, The Authors, Wiley-VCH Verlag GmbH & Co. C) Reproduced with permission from [45]. Copyright 2021, The Authors, Wiley-VCH Verlag GmbH & Co. D) Reproduced with permission from Reprinted with permission from [46], Copyright 2019 American Chemical Society. E) Reproduced with permission from [53] under the terms of the CC-BY-NC-ND license. Copyright 2019, The Authors, American Chemical Society.

Further embracing the biological needs within the field of TE while aiming for the intricate structures made possible with MEW, biomaterial inks have been developed specifically for this AM technology. Poly(2-ethyl-2-oxazine) (PEtOzi) can be processed with MEW in a molten state, but rapidly swells in water to yield thermoreversible hydrogels with high water content of 84% [54]. PEtOzi scaffolds retain water-soluble functional groups and therefore can be functionalized with a wide range of fluorescent peptides. This presents a dual advantage: not only may the scaffolds be tailored for protein adsorption and cell attachment, but also modified to improve visualization.

3.5. Living systems

MEW requires the printing temperature to be relatively high. Until recently, this has limited MEW to thermoplastics and hydrogel-based materials that would then be used as frames to seed cells for biomedical applications. However, cell electrowriting (CEW) had been made possible via the engineering of bioinks based on gelatin and fibrin fibroin to fabricate cell-laden constructs (**Figure 2.7E**). Both formulations were developed to MEW small diameter fibers (up to 200 μm) into different designs with pores as small as 100 μm [53].

4. Modern visualization and manipulation of the MEW process

MEW has some of the best visual access to important real time information of all the AM technologies. Indeed, the visualization of the jet is an important aspect in becoming proficient in MEW printer use and **Table 2.1** directs the reader to several published examples of informative videos. With an elevated nozzle above a collector, the parabolic jet has distinct characteristics that allow monitoring [12], real-time fiber diameter extrapolation [14] and even high-throughput digitized experiments [19].

4.1. Machine Vision

Using the appropriate backlighting, the electrified MEW jet is readily visible with low-cost digital cameras or other accessible optical components. **Figure 2.8B** shows how the various regions of the jet inform aspects such as proximity to the CTS, the existence or lack of fiber pulsing as well as the predicted fiber diameter. This latter perspective was highlighted by Mieszczanek *et al.*[14] who measured the area of the Taylor cone using the number of pixels below the nozzle. By creating a region of interest (ROI) where this Taylor cone area was visualized, specific parts of the scaffold could have their fiber diameters measured using SEM imaging and how this changed with time could be correlated. The fiber diameter was found to strongly correlate with the Taylor cone volume and could even be used to predict printing outcomes in real time.

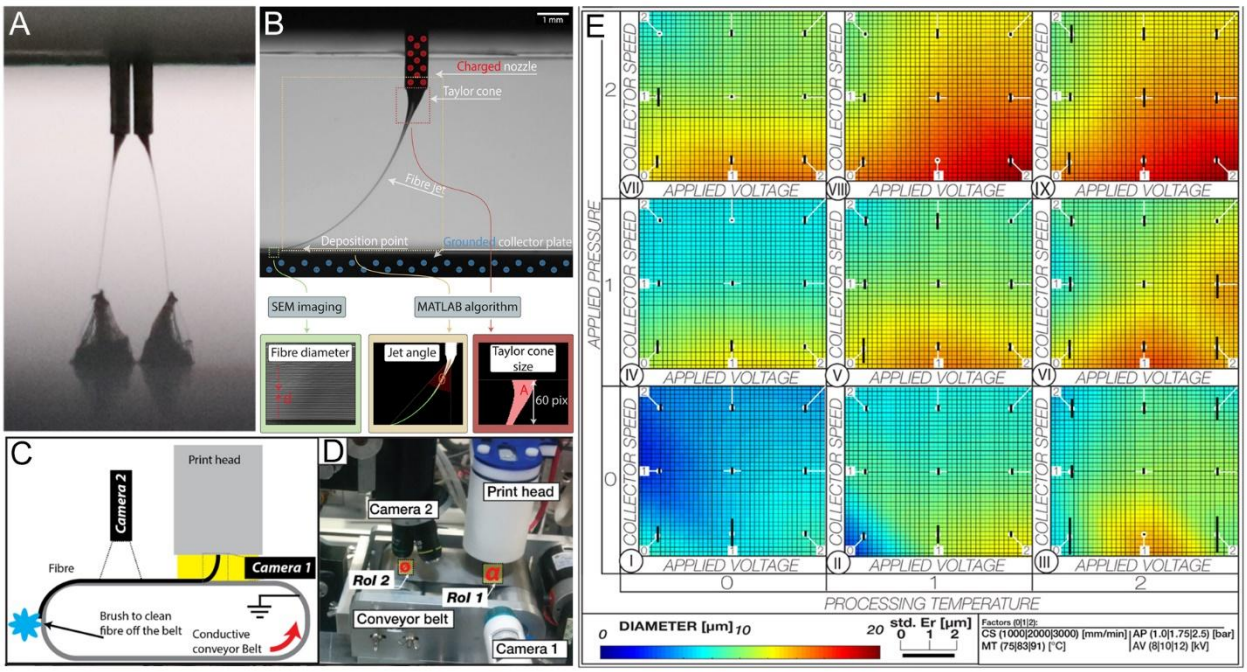

Figure 2.8. Imaging to improve MEW outcomes. A) Backlit lighting of a double nozzle shows the symmetry of fiber collection without stage movement. B) Monitoring the MEW jet to avoid fiber pulsing, especially the Taylor cone volume. C/D) shows a concept MEW printer that uses a conveyor belt to collect and brush off fibers while the jet and fiber diameter are monitored. This

high-throughput approach allows E) multiparametric analysis with heat map fiber diameter presentations covering processing temperature, applied pressure, collector distance and applied voltage, with vertical lines representing the standard deviation. A) Reproduced with permission from [51] under the terms of the CC BY license. Copyright 2022, The Authors, Wiley-VCH Verlag GmbH & Co. B) Reproduced with permission from [14] under the terms of the CC BY-NC license. Copyright 2021, The Authors, Wiley-VCH Verlag GmbH & Co., C-E) Reproduced with permission [19], Copyright 2019, IOP Physics.

4.2. Printomics and the high-throughput screening of printing parameters

The excellent visual access of the MEW jet has allowed fully digitized experiments. In this context, a concept printer was designed and developed that enabled fully programmed control of four crucial printing parameters as well as the automated generation of data using multiple cameras. This was achieved with a conveyor belt printer (**Figure 2.8C/D**) where the jet and fiber is destroyed after a few seconds by a brush – but not before important information could be attained. Using camera vision, the jet angle and fiber diameter could be measured and correlated with the various parameters using heat maps to provide an understanding of multiparametric trends. The important variables measured in this study were melt temperature, applied voltage, applied air pressure and collector speed (**Figure 2.8E**). The parameters that achieved certain diameters on the conveyor belt system were then inputted into a conventional MEW printer to confirm the printing outcomes.

4.3. Variable parameter adjustment during printing

In addition to the many parameters that influence MEW (**Figure 2.9**), there are studies showing how printing outcomes are improved when these change during the print. In one example, the diameter could be changed by adjusting the air pressure during direct writing [9], and another

where the jet speed is observed to decrease for each deposited layer [40]. Rapid fluctuations in the collector speed can also generate patterns and shapes [55] as this parameter changes the fiber diameter.

There are also printing benefits when two parameters are adjusted simultaneously (**Figure 2.9B**). For example, maintaining a constant distance between the nozzle and the top layer during the print is essential for the successful stacking of fibers into thick walls [14]. Even thicker scaffolds result when the electric field strength is slightly increased by adjusting the z-axis while incrementally increasing voltage for each layer during the print [14, 22], shown in (**Figure 2.9C**).

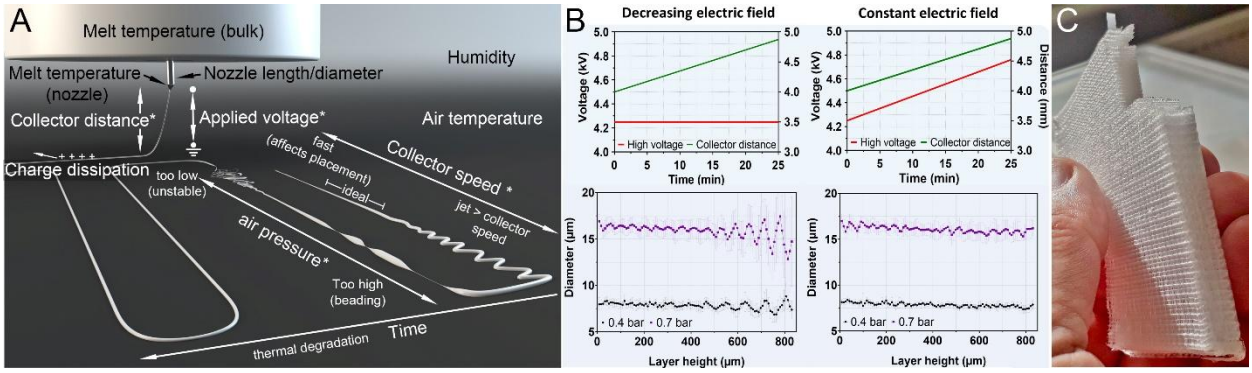

Figure 2.9. Parameters used for MEW A) Schematic indicating the various parameters that can affect outcomes, with an asterisk indicating those that have been adjusted during processing. B) Graphs showing how fiber diameters are affected by decreasing or constant electric fields and the resulting C) thick MEW scaffolds made by slight increases in both the collector distance and voltage for each layer. A) Adapted from [48] with permission, B) Reproduced with permission from [14] under the terms of the CC BY-NC license. Copyright 2021, The Authors, Wiley-VCH Verlag GmbH & Co.

4.4. Perspectives on MEW Printer Accessibility

Of all the publications focusing on MEW, over 95% of them are performed on custom-built systems. In our opinion, there are several reasons for this. The origins of commercial MEW printers are not designed by operators who were already familiar with researchers needs, but come from backgrounds in bioprinting, electrospinning or dispense plotting. Consequently, the learning curve for companies is steep and market forces require MEW printer sales before they reach a quality level that allows the fine control demonstrated by self-built systems.

Commercial MEW printers are also expensive, with price tags that then limit the ability of a MEW user to modify their components for fear of voiding the warranty. As they are built on frames already designed for other purposes, the configuration and many of the components are either over-engineered or not favorable for MEW. There have been some publications that describe the self-building MEW printers [56], notably with one high-end research line system described in 2022 [4]. Designed by expert operators for other MEW users to build, it includes features not available in the expensive and commercial options.

From a configuration perspective, there is little rationale why MEW printers need to be so expensive compared to readily accessible and ubiquitous FFF 3D printers. The next five years will be a defining period for open-source hardware ecosystems for MEW research that provide high quality, low-cost printers available that are readily modifiable – similar to the existing landscape for FFF printers. We expect this accessibility to spur growth in the field and challenge existing MEW printer companies to provide products that are of interest to experienced MEW users rather than expensive entry-level systems that set hurdles to generating interesting data and consequently hinder new MEW users from publishing their research.

5. Conclusion

The parameters that influence MEW processing have been iteratively studied throughout the past decade. To date, MEW produces highly porous, cell invasive, materials that are of interest as scaffolds for several fields, including biomaterials, TE, biofabrication and cancer research. There are further areas where this AM technology could provide benefits, especially fields where single, continuous fibers are important such as optics, electronics and textiles.

New users of this technology will encounter a multi-parametric process that has four essential parameters; melt temperature, applied voltage, applied pressure and collector speed that all influence each other. There are further parameters that can significantly impact printing outcomes depending on the polymer used and the desired outputs. This review has provided a basic summary of the parameters that need to be considered and controlled to achieve high quality MEW scaffolds. While there are undoubtedly further aspects and caveats of the process to discover, the fundamentals to MEW have been established and leveraged to produce a spectrum of different scaffolds applied mainly for biomedical applications.

6. Acknowledgements

We are grateful for discussions and technical insights from Simon Luposchainsky and Dr Ievgenii Liashenko.

7. References

[1] a)Z. Qiao, M. Lian, Y. Han, B. Sun, X. Zhang, W. Jiang, H. Li, Y. Hao, K. Dai, *Biomaterials* **2021**, 266, 120385; b)T. M. Robinson, D. W. Hutmacher, P. D. Dalton, *Advanced Functional Materials* **2019**, 29, 1904664; c)T. D. Brown, P. D. Dalton, D. W. Hutmacher, *Advanced Materials* **2011**, 23, 5651; d)N. T. Saidy, A. Fernández-Colino, B. S. Heidari, R. Kent, M. Vernon, O. Bas, S. Mulderrig, A. Lubig, J. C. Rodríguez-Cabello, B. Doyle, D. W. Hutmacher, E. M. De-Juan-Pardo, P. Mela, *Advanced Functional Materials* **2022**, 32, 2110716; e)G. Hochleitner, F. Chen, C. Blum, P. D. Dalton, B. Amsden, J. Groll, *Acta Biomater* **2018**, 72, 110.

[2] G. Hochleitner, A. Youssef, A. Hrynevich, J. N. Haigh, T. Jungst, J. Groll, P. D. Dalton, *BioNanoMaterials* **2016**, 17, 159.

[3] F. Tourlomousis, H. Ding, D. M. Kalyon, R. C. Chang, *J Manuf Sci E-T Asme* **2017**, 139.

[4] K. F. Eichholz, I. Gonçalves, X. Barceló, A. S. Federici, D. A. Hoey, D. J. Kelly, *Additive Manufacturing* **2022**, 58, 102998.

[5] J. C. Kade, P. D. Dalton, *Adv Healthc Mater* **2021**, 10, e2001232.

[6] E. McColl, J. Groll, T. Jungst, P. D. Dalton, *Materials & Design* **2018**, 155, 46.

[7] S. Luposchainsky, S. Jörissen, A. Nüchter, P. D. Dalton, *Macromolecular Materials and Engineering* **2022**, 307, 2200450.

[8] A. Youssef, A. Hrynevich, L. Fladeland, A. Balles, J. Groll, P. D. Dalton, S. Zabler, *Tissue Engineering Part C: Methods* **2019**, 25, 367.

[9] A. Hrynevich, B. S. Elci, J. N. Haigh, R. McMaster, A. Youssef, C. Blum, T. Blunk, G. Hochleitner, J. Groll, P. D. Dalton, *Small* **2018**, 14, e1800232.

[10] H. Xu, I. Liashenko, A. Lucchetti, L. Du, Y. Dong, D. Zhao, J. Meng, H. Yamane, P. D. Dalton, *Advanced Materials Technologies* **2022**, 7, 2101676.

[11] A. Hrynevich, I. Liashenko, P. D. Dalton, *Advanced Materials Technologies* **2020**.

[12] F. M. Wunner, O. Bas, N. T. Saidy, P. D. Dalton, E. M. D.-J. Pardo, D. W. Hutmacher, *Journal of Visual Experiments* **2017**, e56289.

[13] C. D. O'Connell, O. Bridges, C. Everett, N. Antill-O'Brien, C. Onofrillo, C. Di Bella, *Advanced Materials Technologies* **2021**, 6, 2100345.

[14] P. Mieszczanek, T. M. Robinson, P. D. Dalton, D. W. Hutmacher, *Adv Mater* **2021**, 33, e2100519.

[15] N. Fischhaber, J. Faber, E. Bakirci, P. D. Dalton, S. Budday, C. Villmann, N. Schaefer, *Adv Healthc Mater* **2021**, 10, e2100830.

[16] M. Vernon, J. Lu, B. Padman, C. Lamb, R. Kent, P. Mela, B. Doyle, A. R. Ihdayhid, S. Jansen, R. J. Dilley, E. M. De-Juan-Pardo, *Advanced Healthcare Materials*, n/a, 2201028.

[17] J. Visser, F. P. W. Melchels, J. E. Jeon, E. M. van Bussel, L. S. Kimpton, H. M. Byrne, W. J. A. Dhert, P. D. Dalton, D. W. Hutmacher, J. Malda, *Nature Communications* **2015**, 6, 6933.

[18] M. Javadzadeh, J. del Barrio, C. Sánchez-Somolinos, *Advanced Materials*, n/a, 2209244.

[19] F. M. Wunner, P. Mieszczanek, O. Bas, S. Eggert, J. Maartens, P. D. Dalton, E. M. De-Juan-Pardo, D. W. Hutmacher, *Biofabrication* **2019**, 11, 025004.

[20] J. Ko, S. Jun, J. K. Lee, P. C. Lee, M. B. Jun, *Journal of the Korean Society of Manufacturing Technology Engineers* **2015**, 24, 160.

[21] G. Taylor, *Proceedings of the Royal Society of London* **1969**, 313, 453.

[22] F. M. Wunner, M. L. Wille, T. G. Noonan, O. Bas, P. D. Dalton, E. M. De-Juan-Pardo, D. W. Hutmacher, *Adv Mater* **2018**, 30, e1706570.

[23] A. Hrynevich, University of Wuerzburg PhD Thesis, 2021.

[24] H. Lu, Y. Sun, Y. Chen, L. Nie, L. Yang, L. Du, H. Xu, *Materials Letters* **2023**, 334, 133738.

[25] N. Ristovski, N. Bock, S. Liao, S. K. Powell, J. Ren, G. T. S. Kirby, K. A. Blackwood, M. A. Woodruff, *Biointerphases* **2015**, 10.

[26] E. Bakirci, N. Schaefer, O. Dahri, A. Hrynevich, P. Strissel, R. Strick, P. D. Dalton, C. Villmann, *Adv Biosyst* **2020**, 4, e2000077.

[27] N. T. Saidy, T. Shabab, O. Bas, D. M. Rojas-González, M. Menne, T. Henry, D. W. Hutmacher, P. Mela, E. M. De-Juan-Pardo, *Frontiers in Bioengineering and Biotechnology* **2020**, 8.

[28] a)J. Kim, E. Bakirci, K. L. O'Neill, A. Hrynevich, P. D. Dalton, *Macromolecular Materials and Engineering* **2021**, 306, 2000685; b)H. Ding, K. Cao, F. Zhang, W. Boettcher, R. C. Chang, *Materials & Design* **2019**, 178, 107857; c)K. Cao, F. Zhang, A. Zaeri, R. Zgeib, R. C. Chang, *Advanced Materials Technologies* **2021**, 6, 2100251.

[29] G. Hochleitner, J. F. Hummer, R. Luxenhofer, J. Groll, *Polymer* **2014**, 55, 5017.

[30] C. Blum, *3D Printing and Additive Manufacturing* **2021**, 0, null.

[31] A. Hrynevich, P. Achenbach, T. Jungst, G. A. Brook, P. D. Dalton, *Macromolecular Bioscience* **2021**, 21, 2000439.

[32] M. Putti, M. Simonet, R. Solberg, G. W. M. Peters, *Polymer* **2015**, 63, 189.

[33] S. Liao, B. Langfield, N. Ristovski, C. Theodoropoulos, J. Hardt, K. A. Blackwood, S. D. Yambem, S. D. Gregory, M. A. Woodruff, S. Powell, *BioNanoMaterials* **2016**, 17, 173.

[34] M. Liu, Z. Lin, X. Wang, W. Yan, *Matter* **2022**, 5, 3576.

[35] Q. C. Peiffer, M. de Ruijter, J. van Duijn, D. Crottet, E. Dominic, J. Malda, M. Castilho, *Materials & Design* **2020**, 195, 109025.

[36] T. L. Brooks-Richards, N. C. Paxton, M. C. Allenby, M. A. Woodruff, *Materials & Design* **2022**, 215, 110466.

[37] B. L. Farrugia, T. D. Brown, Z. Upton, D. W. Hutmacher, P. D. Dalton, T. R. Dargaville, *Biofabrication* **2013**, 5, 025001.

[38] J. C. Kade, P. F. Otto, R. Luxenhofer, P. D. Dalton, *Polymers for Advanced Technologies* **2021**, 32, 4951.

[39] H. Haag, D. Sonnleitner, G. Lang, P. D. Dalton, *Polymers for Advanced Technologies* **2022**, 33, 1989.

[40] I. Liashenko, A. Hrynevich, P. D. Dalton, *Adv Mater* **2020**, 32, e2001874.

[41] A. Omidinia-Anarkoli, S. Boesveld, U. Tuvshindorj, J. C. Rose, T. Haraszti, L. De Laporte, *Small* **2017**, 13.

[42] F. Eberle, A.-K. Gruska, B. Filippi, P. Stahlhut, G. G. Wallace, P. D. Dalton, S. Beirne, *Advanced Engineering Materials* **2022**, 24, 2100750.

[43] M. Ryma, T. Tylek, J. Liebscher, C. Blum, R. Fernandez, C. Böhm, W. Kastenmüller, G. Gasteiger, J. Groll, *Advanced Materials* **2021**, 33, 2101228.

[44] J. N. Haigh, Y. M. Chuang, B. Farrugia, R. Hoogenboom, P. D. Dalton, T. R. Dargaville, *Macromolecular Rapid Communications* **2016**, 37, 93.

[45] S. Bertlein, G. Hochleitner, M. Schmitz, J. Tessmar, M. Raghunath, P. D. Dalton, J. Groll, *Advanced Healthcare Materials* **2019**, 8, 1801544.

[46] N. Abbasi, A. Abdal-hay, S. Hamlet, E. Graham, S. Ivanovski, *ACS Biomaterials Science & Engineering* **2019**.

[47] N. Schaefer, D. Janzen, E. Bakirci, A. Hrynevich, P. D. Dalton, C. Villmann, *Advanced Healthcare Materials* **2019**, 8, 1801226.

[48] S. Florczak, T. Lorson, T. Zheng, M. Mrlik, D. W. Hutmacher, M. J. Higgins, R. Luxenhofer, P. D. Dalton, *Polymer International* **2019**, 68, 735.

[49] J. N. Haigh, T. R. Dargaville, P. D. Dalton, *Materials Science and Engineering: C* **2017**, 77, 883.

[50] G. Hochleitner, E. Fürsattel, R. Giesa, J. Groll, H. W. Schmidt, P. D. Dalton, *Macromol Rapid Commun* **2018**, 39, e1800055.

[51] R. Sanchez Diaz, J. R. Park, L. L. Rodrigues, P. D. Dalton, E. M. De Juan Pardo, T. R. Dargaville, *Advanced Materials Technologies* **2021**, in press.

[52] J. Meng, F. Boschetto, S. Yagi, E. Marin, T. Adachi, X. Chen, G. Pezzotti, S. Sakurai, H. Yamane, H. Xu, *Materials & Design* **2021**, 210.

[53] M. Castilho, R. Levato, P. N. Bernal, M. de Ruijter, C. Y. Sheng, J. van Duijn, S. Piluso, K. Ito, J. Malda, *Biomacromolecules* **2021**, 22, 855.

[54] D. Nahm, F. Weigl, N. Schafer, A. Sancho, A. Frank, J. Groll, C. Villmann, H. W. Schmidt, P. D. Dalton, R. Luxenhofer, *Materials Horizons* **2020**, 7, 928.

[55] C. Xie, Q. Gao, P. Wang, L. Shao, H. Yuan, J. Fu, W. Chen, Y. He, *Materials & Design* **2019**, 181, 108092.

[56] M. Lanaro, A. Luu, A. Lightbody-Gee, D. Hedger, S. K. Powell, D. W. Holmes, M. A. Woodruff, *The International Journal of Advanced Manufacturing Technology* **2021**, 113, 2539.

CHAPTER 3: VISUALIZING FIBER PATH AND GENERATING G-CODE FOR MELT ELECTROWRITING OF TUBULAR SCAFFOLDS USING GRASSHOPPER SOFTWARE

O'Neill KL, McLoughlin T, Van der Linden G, Buson IL, Paxton NC, Polites M, Dalton PD. (2025) Visualizing fiber path and generating G-code for melt electrowriting of tubular scaffolds using Grasshopper software. *Visual and Virtual Prototyping*, **20**, e2466190.

This chapter presents a computational design framework that integrates Grasshopper and Rhinoceros software with MEW to visualize, predict, and generate toolpaths for tubular scaffold fabrication. The work demonstrates how algorithmic design principles can be applied to microfabrication, addressing a substantial challenge in MEW: the absence of predictive modeling and "slicing" software to translate digital scaffold designs into fabrication-ready code. By combining digital visualization with automated G-code generation, this study establishes a distinct workflow that merges computational modeling and geometry to enhance scaffold design prediction and accessibility. The platform provides an accessible foundation for rapid design iteration and parameter optimization, enabling users to directly link virtual scaffold geometry with physical MEW fabrication, thus connecting the digital and physical aspects of scaffold design and fabrication for TE.

Scientific Contribution and Advancement of Knowledge

This chapter expands the scientific and technological framework of MEW by introducing a visual algorithmic tool for scaffold design that connects computational geometry with electrohydrodynamic processing. The use of Grasshopper enables the generation of continuous and mathematically precise toolpaths that predict fiber placement on tubular collectors, addressing the challenge of visualizing three-dimensional deposition paths before printing. The study

demonstrates how user-defined parameters such as winding angle, inter-fiber spacing, tube diameter, and number of layers can be computationally linked to physical scaffold outcomes, providing quantitative validation between virtual predictions and printed structures. By achieving close correspondence between simulated and experimental fiber architectures, this work establishes a new standard for predictive modeling in MEW. The introduction of logic-based G-code generation represents a critical step forward in automating and standardizing MEW fabrication, facilitating reproducibility across research labs and opening avenues for hypothesis-driven scaffold design based on computational parameter control.

Broader Implications and Future Directions

This work contributes broadly to the fields of computational virtual prototyping, additive manufacturing, and scaffold design. It exemplifies how design tools originally developed for architecture and engineering can be repurposed to address challenges in additive manufacturing for biomedical applications. The parametric workflow established here provides a scalable framework for integrating mathematical modeling, visualization, and fabrication for MEW tubular structure. Future directions include coupling this approach with multi-material MEW systems and developing libraries of scaffold geometries optimized for specific tissue applications. Collectively, this chapter advances the field toward digital precision biofabrication, supporting the long-term objective of creating customizable, high-fidelity, and clinically translatable scaffolds for TE applications.

Visualizing Fiber Path and Generating G-code for Melt Electrowriting of Tubular Scaffolds Using Grasshopper Software

Kelly L. O'Neill[1#], Taite McLoughlin[1,2#], Georgia Van der Linden[1], Ignacio Lopez Buson[3], Naomi C. Paxton[1,4], Mary Polites[2], Paul D. Dalton[1*]*

1. Phil and Penny Knight Campus for Accelerating Scientific Impact, University of Oregon, 1505 Franklin Boulevard, Eugene, OR 97403-6231, USA

2. College of Design, School of Architecture & Environment, 5249 University of Oregon, Eugene, OR 97403-5249, USA

3. College of Design, School of Landscape Architecture, 5249 University of Oregon, Eugene, OR 97403-5249, USA

4. Centre for Biomedical Technologies (CBT), Queensland University of Technology (QUT), Brisbane 4000, Australia

# These authors contributed equally to this publication.

Corresponding authors: Paul D. Dalton pdalton@uoregon.edu; Mary Polites* mpolites@uoregon.edu.

Key words: additive manufacturing, melt electrospinning writing, poly(ε-caprolactone), G-code generation, tubular scaffolds, grasshopper, computational design

Abstract for “Visualizing Fiber Path and Generating G-Code For Melt Electrowriting of Tubular Scaffolds Using Grasshopper Software”

Melt electrowriting (MEW) produces high-resolution, highly porous microfiber scaffolds that are consistently replicable. While typically used to produce planar scaffolds, tubular microfiber structures are increasingly needed for tissue engineering (TE) applications (e.g. vascular TE). Designing such microfiber tubes is challenging due to the continuous fiber deposition required by MEW, and the difficulty of coding a three-dimensional geometry without the ability to previsualize it. This study introduces a new design approach that simplifies programming, provides a digital scaffold preview, and rapidly generates G-code iterations in AeroBasic script (compatible with Aerotech axis system) by using Rhinoceros, a well-known CAD 3D modeling software, and its built-in algorithmic design plugin, Grasshopper. The resulting 1 mm and 3 mm inner diameter MEW tubes consisted of fiber diameters 10.8±0.7 μm or 20.7±0.9 μm and matched the programmed design. This visual prototyping platform through Rhinoceros and Grasshopper offers a new method in predicting fiber paths and incorporating scaffold design parameters, meeting the need for diverse tubular scaffolds in fields such as biofabrication, TE, cancer research, and 3D *in vitro* models of injuries and diseases. In this study, we investigate whether a digital preview of tubular scaffolds and corresponding G-code generation system can enhance the accuracy and efficiency of designing tubular microfiber scaffolds for biofabrication applications.

1. Introduction

Three-dimensional (3D) environments, such as matrices and scaffolds, have been engineered to more accurately replicate native tissue in response to 2D systems being unable to accurately replicate *in vivo* situations [1]. To overcome the limitations of 2D cell culture, additive manufacturing has become part of the growing initiative to produce porous materials, termed scaffolds, which play an important role in 3D cell culture. For some 3D printing applications for tissue engineering (TE), Rhinoceros (or simply, Rhino) and Grasshopper have been utilized early in the design phase to control patterning, grid structures, and build onto a 3D model [2, 3]. As a parametric design tool, Grasshopper is a visual programming environment that allows for shape generation of digital models through algorithms. The user interface provides a logic structure that utilizes multiple user-controlled inputs flowing into geometric commands allowing for micro-control and rapid iteration of design. In its traditional use for additive manufacturing, this process results in 3D models as stereolithography (STL) files that must then be "sliced" by additional software to generate a set of instructions, or G-code, that are translated by the printer into axis movements.

In TE, scaffolds are used to create cell instructive microenvironments to study different tissues [4-6]. To more closely resemble native tissue, scaffold features must be small and precise. Melt electrowriting (MEW) has been employed to fabricate such high-resolution scaffolds from microscale polymer fibers [7]. This is achieved by electrifying an extruded polymer melt to establish a thin jet between the nozzle and the collector. When the polymer jet is properly controlled, MEW allows for the creation of high-resolution, highly porous, and well-organized scaffolds. MEW scaffolds are used to approximate or resemble native tissue architecture, either alone or by combining with a range of biofabrication techniques [5, 8].

MEW is a direct writing approach that uses a repeated tool path over a substrate to deposit microfibers in a controlled manner. The fiber diameters produced by MEW can be as small as 0.35 μm [9], which is significantly smaller than what is possible with conventional melt-extrusion 3D printing [10]. Enhancing its relevance to biomedical applications, medical grade poly(ε-caprolactone) (PCL) is the current favored material for MEW. Featuring a low melting point (60 °C) and high thermal stability, it has been demonstrated that continuously heated PCL can be stably processed through MEW for up to 25 days [11]. PCL degrades slowly over approximately 2-3 years, serving both as a stable substrate for typical 3D *in vitro* research and offering degradable properties appealing in biomaterials research [12]. More recently, MEW has been used to create tubular scaffolds with unique and tailorable mechanical properties, including for heart valves [6, 13, 14] and blood vessels [15].

Historically, the writing of G-code, movement-based instructions of 3D printers, has been composed line by line by the user, requiring changes that are vulnerable to human error. To streamline this workflow, G-code generators are often used to globally alter G-code based on scaffold parameters chosen by the user. Such parameters include scaffold dimensions, distance between fibers (called inter-fiber distance), and/or intersection angles. G-code generators are often, but not always, paired with a digital prediction of the scaffold design that predict visuals for much more rapid iteration between designs since the user can bypass the realization of a physical prototype. Existing G-code generators developed for Computer Numerical Control (CNC) machines, such as Mach 3, have been used to generate flat scaffold designs [19-21]. An online G-code generator for MEW tubes designed by McColl *et al.* was useful in predicting fiber path and G-code output [22]. **Supplementary Figure S2.1** summarizes the differences and similarities of these digital environments to our workflow.

The workflow for MEW has not yet adopted approaches common to other 3D printing technologies. Primarily, MEW scaffolds lack "slicing" software, which is common in digital fabrication as a process that translates digital models into G-code for fabrication. This lack of slicing software has kept the fabrication of MEW scaffolds to lines of code rather than digital models which results in inaccurate representation of scaffold structure and lack of alternative designs. In this paper we utilize AeroBasic script which is compatible with our printers' Aerotech axis system. The AeroBasic script is a parameter-based coding structure where variables can be defined early on and then called into the code at various points throughout the printing process. To weave user defined inputs in a G-code framework, Grasshopper definitions were developed and informed by the book *Advanced 3D Printing with Grasshopper,* a reference using design of toolpaths for fabrication in clay 3D printing[16]. This research paper aims to establish foundational printing principles toward the goal of generating representational models of tool paths for MEW 3D printing with Grasshopper. Grasshopper was selected as it is a tool used in the design industry for facilitating rapid visual iterations and enables users to design *definitions: a series of input steps that provide an output as a result.* The term "*definition"* is the generally accepted term for a Grasshopper visual code. Although Grasshopper is already well-established in several industries, it has yet to be fully explored for scaffold design within TE. Previous work includes using Grasshopper to run the coordinate-based G-code virtually to visualize the resulting scaffold [17]. For this, researchers needed an already working G-code to run their preview. In a separate line of research, Rhino 7 has been employed to create a fiber path pattern [17, 18]. In this current work, we developed a platform which simultaneously creates a virtual model of a calculated approximation of the scaffold based on the user input parameters and generates its corresponding G-code. Our platform differs from existing work because AeroBasic language enables use of logic

loops (hereby going beyond a traditional coordinate-based system) to create more succinct G-codes.

When considering tubular printing, in addition to the inherent need of producing a continuous path, there is a need to incorporate collector speed changes that match an angular speed when printing onto a cylindrical mandrel [22]. We demonstrate that Grasshopper is effective to design, visualize, and generate G-code for MEW microfiber scaffolds considering these constraints as part of definition (**Figure 3.1**). As AeroBasic was the required language of output for printing, Grasshopper was adopted since it allows for a multitude of different formats of G-codes for other linear stage platforms. We developed our G-code generator to print MEW fibers parallel to the length of the tube and wind fibers onto the cylindrical collector in a crosshatch pattern. This design builds on the traditional flat scaffold design ("boxed"), which corresponds to the industry standard structure for TE scaffolds intended for cell-seeding. Compared to the current standard which requires physically printing the scaffold to visualize the resulting fiber path, our platform allows for rapid exploration of individual variable changes on final print. For example, the user can explore the "turn count" parameter and promptly visualize a digital version of a tube with different fiber spacing and angle. We further propose a set of printing parameters for the different designs and chosen fiber diameters to assist MEW adoption by new users.

2. Experimental Section

2.1. Materials

Medical grade PCL (Corbion, Netherlands, PURASORB, PC12, Lot nr: 2007001461) was used for all experiments. To prevent the long-term degradation of the polymer, the PCL was transferred into 50 mL Falcon tubes and kept at -20 °C for long-term storage.

2.2. Custom-built MEW printer

Scaffolds were fabricated on a custom-built MEW printer, with the configuration and the parameter settings highlighted in **Figure 3.1**. Operating with AeroBasic language, the printer movements are combined with independent temperature control using two heaters and thermocouples, enclosed in a high-temperature-resistant polyether ether ketone (PEEK) housing. Hardware controls include high voltage (AU-20P1.5-LC, Matsusada, Japan), applied air pressure (SMC Corporation, Japan), and temperature interfaces (Bach Resistor Ceramics GmbH, Germany). Digital control of voltage and pressure is achieved through wiring connections to the Aerotech X axis control tower, enabling remote control over printing parameters. This remote-control feature is valuable when combined with G-code generator platforms since the printing parameters can be independently programmed in the G-code script of choice. The MEW printer also features a grounded tubular collector with a custom-built brass piece to stabilize the mandrel, ensuring precise fiber placement. Stabilization of the jet is performed on the same collector where the scaffolds are printed.

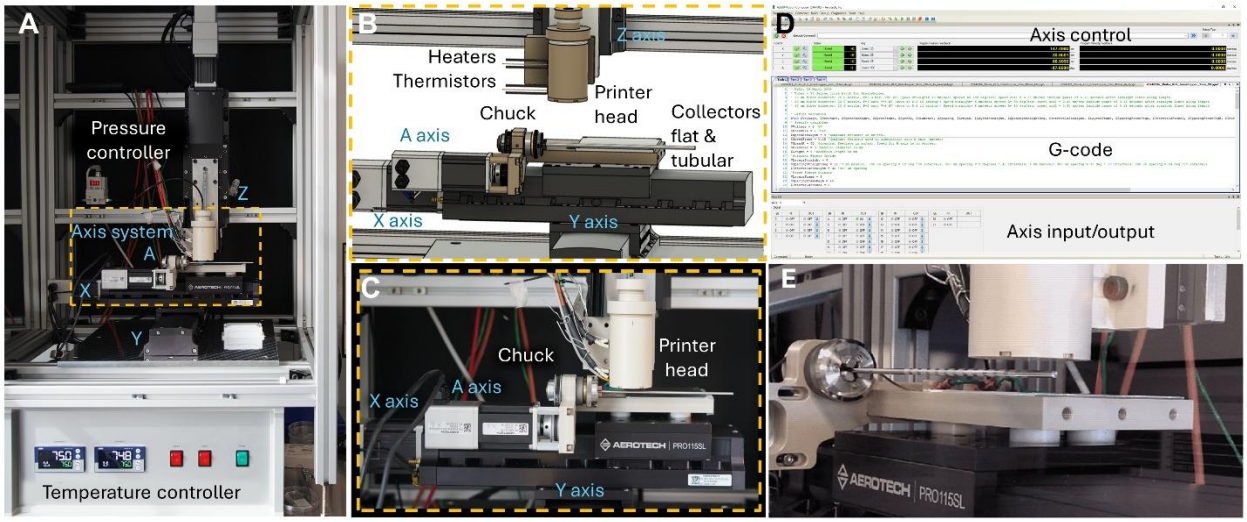

Figure 3.1. Custom-built MEW printer 4-axis system. A) Photograph of MEW printer and components. B) close-up of the Fusion 360 render of MEW printer with axis system, printer head and components and flat plus tubular dual collector configurations. C) Photograph of close-up of MEW printer. D) Screenshot of software interface A3200 Motion Composer, with different regions of the interface indicated. E) Photograph of tubular collector with a series of fabricated MEW scaffolds. A high-resolution image of D) is supplied in the ***Supplementary Figure S3.2****.*

2.3. MEW processing parameters

MEW scaffolds were printed on a custom-built printer. PCL (PC-12, Corbion) polymer pellets were loaded into a 3 mL glass syringe with a nozzle cut to protrude 1 mm from the MEW printer head. The syringe was placed inside the printer head and heated to 75 °C until the polymer fully melts (first time at least 1 h, future uses require approximately 20 min). Air pressure (1.5 bar) applied to the syringe extruded the polymer melt through the nozzle at rates where the resulting target diameters are either 10 µm or 20 µm. The collector distance (the distance between the nozzle tip and grounded collector) was kept constant at 3 mm for all experiments. Other parameters kept constant were an applied voltage of 5.5 ± 0.5 kV, ambient temperature of 20.5 ± 1 °C and relative

humidity of 35 ± 1%. Temperature and relative humidity were measured continuously over the course of printing with a wireless device (Tempy2, USA). When targeting the different fiber diameters of 10 or 20 μm, different gauge nozzles (25G and 23G, respectively) and processing conditions were used. Other variable processing conditions such as pressure (bar), and discrete speeds (mm/sec or deg/sec) are listed in **Figure 3.5**.

2.4. Scaffold design

Grasshopper (version 09/2023) was used to create a visual code for MEW scaffold visualization and G-code generation. Mathematical equations were applied, and parameter selection was incorporated into Grasshopper definition (outlined in **Supplementary Video S3.1**) (see section 3.1.). The G-code was loaded onto A3200 Motion Composer Version 6.04.005 (Aerotech, USA) (see section 3.2.) while screenshots of the AeroBasic software interface show a model code (**Figure 3.1D**), with a high-resolution image provided as **Supplementary Figure S3.1**.

2.5. Characterization of scaffolds

Scaffolds were characterized for their fiber placement, fiber morphology, fiber diameter and fiber spacing using Keyence light microscope and SEM (Helios SEM, Thermo Fisher) using the Everhart-Thornley detector (ETD) under Secondary Emission (SE). Prior to SEM imaging, MEW scaffolds were sputter coated with gold of approximately 10 nm thickness using a chamber pressurized with argon (Hummer II, Technics, USA). Inter-fiber distance was measured perpendicular to fiber direction by identifying the edge of one fiber to the further edge of the adjacent fiber to reduce human error in trying to identify the mid-fiber point. SEM images were acquired at a current of 1.4 nA and voltage of 2 kV. Photographs and videos were taken on a SONY SteadyShot α7III camera with lenses SONY FE4/24-105 G OSS and Canon macro lens EF 180

mm 1:1.5 ultrasonic adapted with Fotodiox Pro EF-Sny (E) Fusion. Videos were edited using Adobe Premier Rush version 2.10.0 (Build 30) (Adobe Creative Cloud, USA).

3. Results and Discussion

The purpose of this study is to demonstrate the efficacy of using an algorithmic design platform like Grasshopper to generate both the virtual and physical scaffold prototypes and compare their similarity to validate the utility of this approach. This brings together a well-known software from the design industry and applies it to microfiber scaffold formation at millimeter length scales.

3.1. Developing a user-friendly platform for MEW tube design prediction

Although Grasshopper's user-friendly interface made visual programming mainstream in the design industry (product design or architecture), developing a robust parametric tool (or definition in Grasshopper's terms) for a particular objective like the one explained in this paper, requires knowledge of algebra, geometry, and trigonometry, in addition to understanding the basic logic of the Grasshopper's language. Nevertheless, the potential of a definition relies on the ease to change its parameters which allows the user to explore endless iterations. In addition, once a definition has been created and properly labeled, it can be operated by a user without previous knowledge of Grasshopper, provided they understand how to enter the necessary parameters and how to export the resulting outcome.

Every Grasshopper definition begins with user input parameters that control the final output MEW tube visualization as shown in **Figure 3.2**. These parameters pass through a series of geometric and algebraic formulas that allow for user generated shifts and changes, which display the parametric tube iterations. **Supplementary Video S3.1** demonstrates interaction with the

software to generate MEW fiber path by drafting an initial spiral and looping the building system off itself to display a digital model.

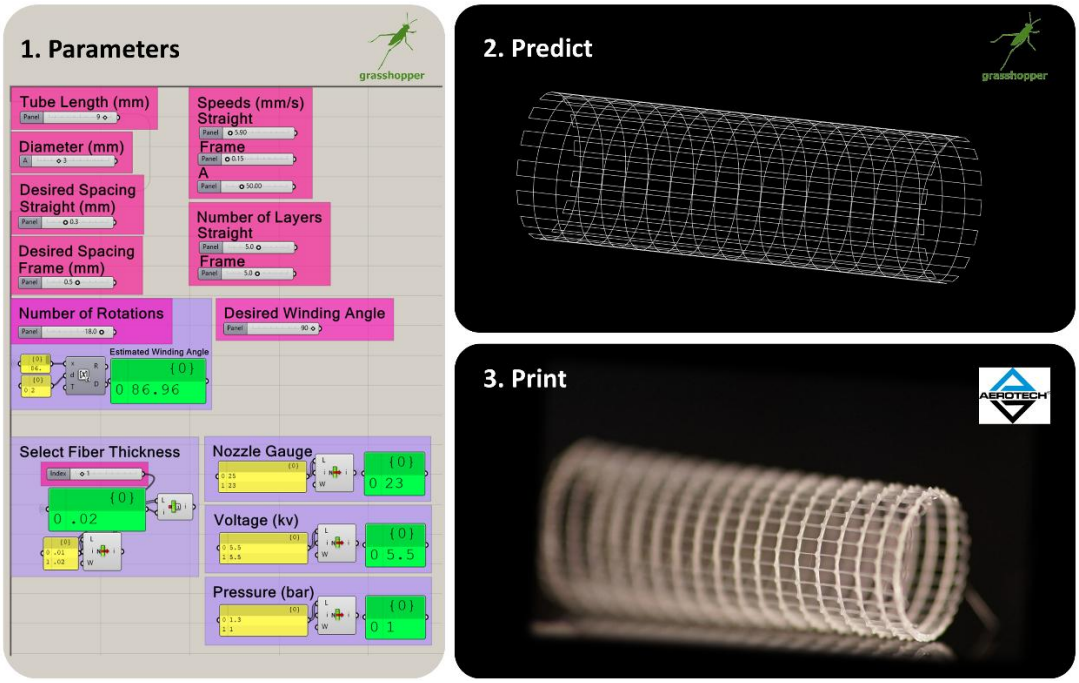

Figure 3.2. Flow chart of MEW path prediction and tube printing: 1. Choose parameters on Grasshopper platform with pink identifying user-controlled inputs and purple grouping calculations for green calculated inputs; 2. Use Grasshopper to generate fiber path prediction. This platform also outputs G-code in AeroBasic script (not shown here); 3. Load G-code onto Motion Composer A3200 connected to custom MEW printer to execute printing operations onto a tubular collector, resulting in tubular scaffold. Printing parameters (shown in 1), fiber path prediction (shown in 2) and final print (shown in 3) correspond to scaffold with 3 mm inner diameter, 20 µm fiber diameter, 300 µm spacing along length and 90° crosshatch pattern. ***Supplementary Figure S3.3*** *is provided for improved visualization of the numerical content.*

For the purpose of guiding the new MEW user, we isolated parameters that impacted scaffold design and functionality the most significantly (**Figure 3.2**) [7]. To facilitate ease of use,

parameters that require user input are highlighted in pink. Any parameter that the user should double check, but they cannot directly edit, is highlighted in green, e.g. the winding angle is highlighted in green as it is calculated based on the user input number of rotations which is highlighted in pink. These parameters feed directly into the G-code (see section 3.2) and they also control the visualization of the tube prototype. Select equations needed to convert base parameters to necessary variables are included in the visualization section of this code, though they may be used in the G-code as well.

Tubes are designed beginning with a base layer of aligned fibers, fibers which run parallel to the mandrel. The user inputs a desired distance between these fibers (straight), here (see **Figure 3.2**) being a 300 μm separation, and the Grasshopper definition converts that to a certain number of intervals that the circumference of the tube is divided into. From there fibers are drawn connecting these interval points at alternating ends of the tube structure. For this to be a closed layer, the number of intervals must be a factor of 360, a limit which is embedded into the code so that it cannot be accidentally broken by the user. However, this means that desired fiber spacing can be subject to slight deviations to account for an even distribution of fibers around the circumference.

After the first layer of aligned fibers, we addressed the spiralized geometry of a tubular print. As the feed nozzle of the MEW printer is moving with a stable molten jet, the crosshatch fibers are more accurately visualized as layered spirals that travel the length of the tube. The most straight forward way for users to control the visuals of the tube is to choose a certain number of rotations of the mandrel to complete one layer of the tubular scaffold. The Grasshopper definition provides the calculated angle between the aligned fibers and the crosshatch, named in this work as “winding angle”. The definition also allows users to input a desired winding angle which will be noted with

the calculated angle in the final G-code for user analysis. Once the initial spiral path has been completed (**Figure 3.3C**), a looping pattern is established to repeat the curve at calculated intervals around the tube. The equation that produces this interval, N, is $N = \frac{360}{\left(\frac{4}{D} \cdot \omega\right)}$ where ω is the winding angle, D is the diameter of the mandrel. After the loop runs N times, the code has produced a closed loop of crosshatch spirals around the tube.

There are several ways to visualize these tubes in Grasshopper and we have included the most relevant pictured in **Figure 3.3E**. These three methods include a simple curve, a pipe structure, and a curve with thickness and color. The curve and pipe structures can be output as geometry or "baked" into Rhino's workspace to be manipulated and analyzed independently as objects. Alternatively, the material-based curve is best for rapid iteration within the Grasshopper definition as the user is making micro-adjustments to parameters. Since the Grasshopper interface is a large working screen with Zoom in/out functionality, we have provided the full resolution image as **Supplementary Figure S3.4**.

The digital models serve the user as both iterative records of scaffold designs and can be imported into the main workspace of Rhino and be explored further through visualization tools used to approximate materiality, element exposure, and more. In this work, we define a translational workflow which combines mathematical modelling, geometric prediction, and post processing in a way that is unique and currently not possible in other generators or workflows.

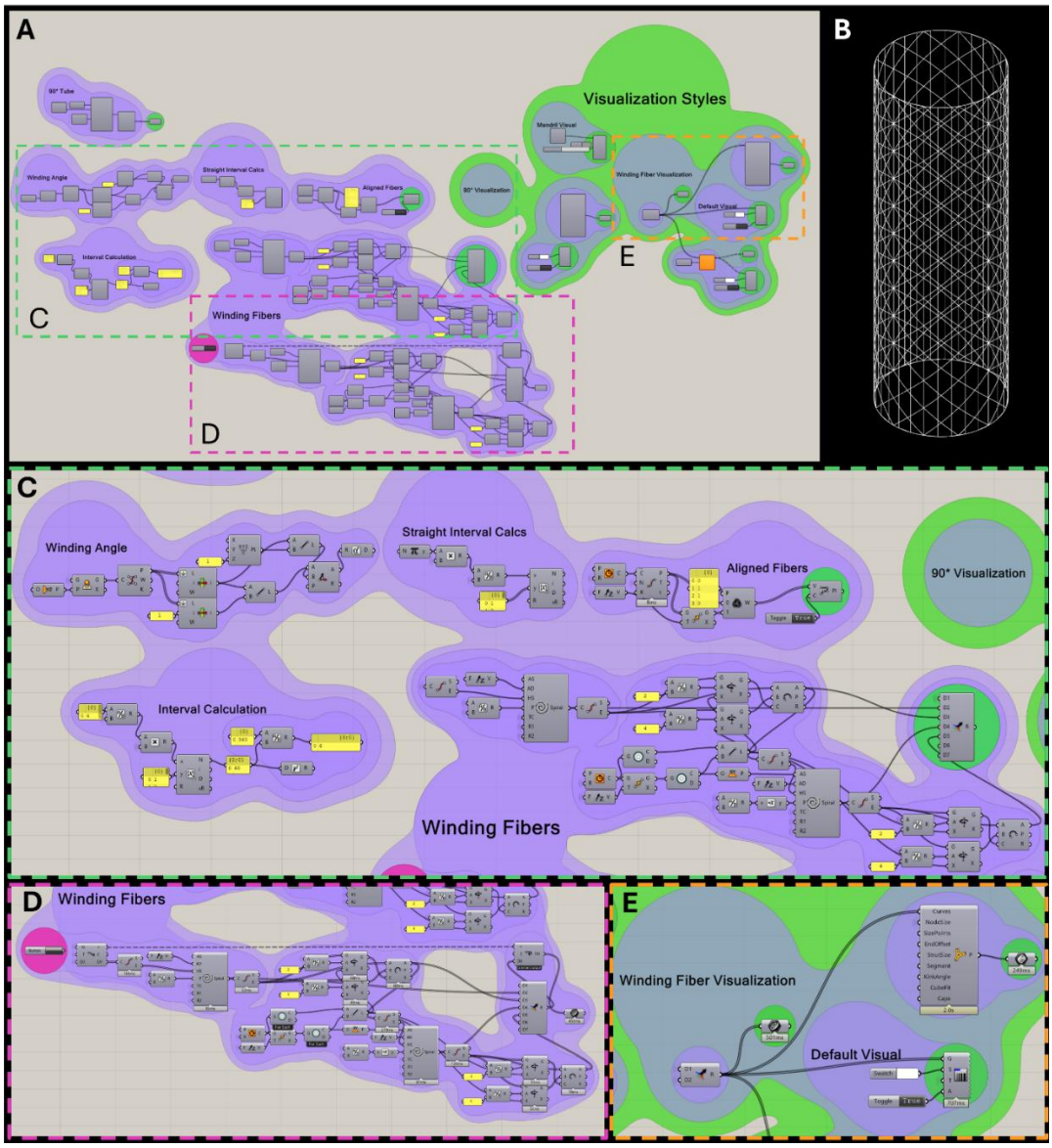

Figure 3.3. Grasshopper definition for predicted MEW tube visualization. A) Screenshot of visualization section of Grasshopper definition. B) Close up of model of predicted tube structure. C) Screenshot of Grasshopper definition of initial path calculations and simulations. D) Screenshot of Grasshopper definition looping system to model final structure. E) Screenshot of Grasshopper definition of winding fiber visualization. ***Supplementary Video S3.1*** *demonstrates the process of generating the MEW tube visualization tool path.* ***Supplementary Figure S3.4*** *shows the entirety of the Grasshopper definition in high resolution.*

3.2. Developing G-code generator to match predicted fiber path

Grasshopper was used to create a G-code generator, automatically applying algebra and adjustment to parameters that would normally require multiple iterations from the user. The Grasshopper definition that converts parameters into text G-code can be seen in **Figure 3.4**. Since AeroBasic utilizes a define and call system for G-code parameters, the parameters input into Grasshopper can be easily plugged in to update G-code as necessary. The one difference in this code generator stems from our rotation-based modelling approach which requires a change in the body of the code adjusted by our input parameters. The date and pertinent calculations are automatically commented into the code for easy user review and data tracking. Additionally, there is a panel highlighted in pink with an example comment where users can input their own desired comments and data. To retrieve the code once all parameters are in place, the user simply right clicks on the final code panel and clicks "copy data only." The code can then be pasted into a text file for storage/editing or copied directly to AeroBasic for printing. This platform provides an AeroBasic script based on user input parameters, although variations can be made to fit parameters into any preferred coding language. To validate the predicted fiber path, MEW tubes were printed. **Supplementary Video S3.2** shows interaction with the software to generate G-code in AeroBasic language. To demonstrate the similarities between the Grasshopper visualization and MEW printing, we compiled the visualization and corresponding tubular printing side-by-side in **Supplementary Video S3.3**.

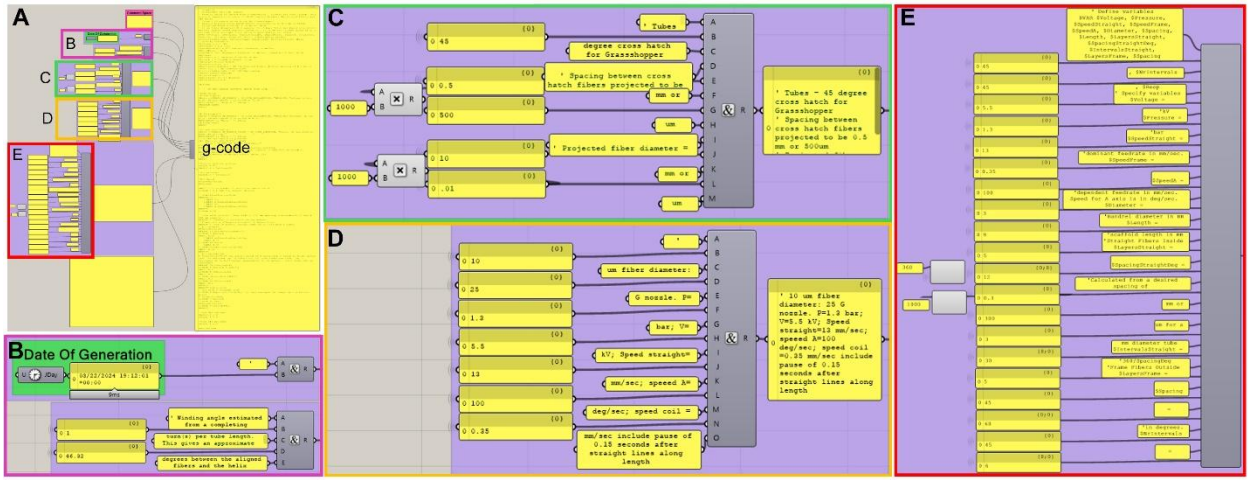

Figure 3.4. Screenshot of Grasshopper definition of MEW G-code generator for tubes in AeroBasic language. A) Overview of code writing structure. B) Output of code: generated G-code. C) Close-up screenshot of variable definition section pulling from user parameters with user comment section. D) Close-up of defined variables section of G-code E) Close-up screenshot of compiling structure for main code block with user input parameters pulled into variable definitions. Supplementary Figure S3.4 shows the entirety of the Grasshopper definition in high resolution.

3.3. Design space

The tube design space for this study is summarized in **Table 3.1**. Based on existing G-codes, we introduced design parameter sliders to be used by users to create unique designs. The need for this is demonstrated in several previous studies on using MEW tubes for TE applications, including blood vessels [23], cell therapy containers for Type 1 diabetes [24], and nerve guides. To provide structure and framework to this program, key winding angles were chosen, and the Grasshopper definition was built from these examples. Using this platform, the user has a digital preview of tubes based on their input parameters. Further, the user is offered a list of pre-set parameters for

predicted fiber diameter. Printed tubes from Grasshopper generated G-code codes are shown in **Sections 2.4** and **2.5**.

Table 3.1. Design space for MEW tubular scaffolds. Using two target diameters of 10µm and 20 µm, a spectrum of MEW tubes was designed and fabricated with the following properties.

Target fiber diameter (µm)	Tube diameter (mm)	Tube length (mm)	Number of layers	Winding angle (°)	Spacing parallel to length (µm)	Spacing of crosshatch (µm)
10	1	3	4	90, 67.5 and 45	300	500
	3	9	10	90, 67.5 and 45	300	500
20	3	9	10	90, 67.5 and 45	300	500

3.4. Scaffold characterization

To validate our G-code generation program, the G-code output from the Grasshopper program was then initiated once the stabilization stage is complete (approx. 2 min). After stabilization is complete, our designs begin with printing of MEW fibers along the length of the tube (**Supplementary Video S3.4**). Then, the second layer creates a winding angle in reference to the previously deposited fibers. The proposed library of tubes ranging different fiber spacing and winding angles is shown in **Table 3.1**, while the corresponding visual paths and stereomicroscope images of MEW scaffolds are shown in **Figure 3.5**. **Supplementary Video S3.5** summarizes the comparison between the Grasshopper predicted fiber path, the video of MEW printing to create different winding angles (45°, 67.5° and 90°), and corresponding light microscope images of the complete resulting scaffold. It is important to note that the ends of the tubes shown in **Figure 3.5** exhibit some defects (yellow arrows) which are not shown in the generated tool path. This is

because the MEW technology has jet lag associated with it, and any small changes in the speed of the jet will affect the fiber lay-down, especially where there is directional change.

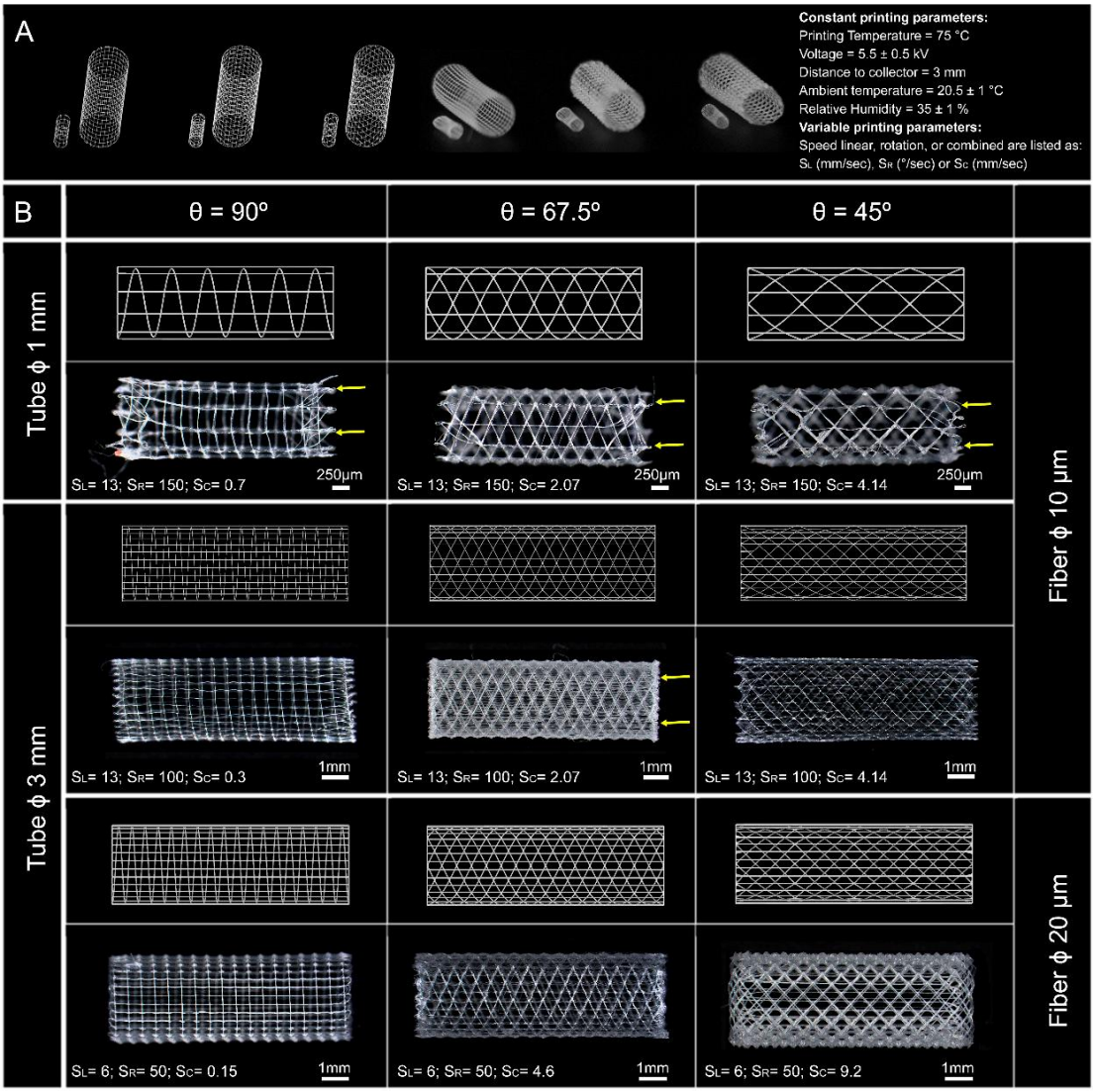

Figure 3.5. Summary of library of tubes printed compared to Grasshopper rendering. A) Render of tubes with inner diameter of 1 and 3 mm with different crosshatch angles (90°, 67.5° and 45°) (left), and photograph of corresponding printed tubes (right). B) Side-by-side comparison of Grasshopper render (top) and corresponding printed scaffold (bottom). Render and corresponding scaffolds are organized by diameter: 1 mm (top) and 3 mm (bottom); and by fiber

size: 10 µm (top) and 20 µm (bottom). Yellow arrows indicate defects from a directional change. Scale bars of 1 mm diameter tubes: 250 µm. Scale bars of 3 mm diameter tubes: 1 mm.

Fiber spacing between parallel lines

Two different fiber spacings for the toolpath were chosen: 200 and 300 µm while the number of intervals approximately is as described by **Equation 1**. Fiber distance between the crosshatch fibers was programmed to be consistent throughout all scaffold designs: 500 µm.

Equation 1

$$Number\ of\ aligned\ fibers\ =\ \left(360 * \frac{diameter}{spacing}\right),\ rounded\ to\ the\ nearest\ factor\ of\ 360.$$

For example: 1) For 3 mm mandrel: For 300 spacing - 12 deg * 30 intervals; for 200 spacing - 8 degrees * 45 intervals.

2) For 1mm mandrel: For 300 spacing - 36 deg * 10 intervals; for 200 spacing - 24 degrees * 15 intervals.

Winding angle

Winding angle refers to the angle the crosshatch fiber makes with lines parallel to the tube length. For demonstration purposes, we chose three different angles: 45°, 67.5° and 90°. Different angles are dependent on the number of rotations per tube length. For a 45° winding angle, the mandrel was rotated once, which is equivalent to 360° x 1. Similarly, for a 67.5° winding angle, we rotated the mandrel twice for the same length (i.e., 360° x 2). Alternatively, to create a design in which the fibers were placed perpendicular to each other, (i.e. 90° winding), we divided the length of the scaffold by the desired spacing to know the number of turns necessary. Specifically,

for a length of 9 mm and desired spacing of 500 μm, we rotate the mandrel 18 times along the length. Similarly, if the tube length is set at 3 mm for the same desired spacing (500 μm), we program the mandrel to rotate 6 times along the length.

Fiber spacing between crosshatch

The toolpath for fiber placement on the crosshatch design was calculated to be uniform across both diameters and all winding angles. We aimed for 500 μm spacing, which is calculated by a rotation distance on either end of the tube. Similarly to the fibers that lie parallel to the length of the tube, the distance between them was calculated by Equation 1. For 500 μm spacing on a 3 mm mandrel, we program the printer to rotate 30° on the A axis for an adjusted spacing of 517 μm. For a 1 mm mandrel, we program a movement of 60° which theoretically predicts 524 μm. After printing with these programmed distances, we measured the inter-fiber distance of 513±13 μm (**Supplementary Figure S3.3**) (see section 2.6.1).

Fiber diameter

To yield the target fiber diameters, scaffolds were printed with varying parameters to yield these sizes. Using a target diameter of 10- and 20-μm, the actual fiber diameter was measured using SEM (Thermo Fisher Scientific, USA). On average, fibers were measured to have a diameter of 10.8±0.7 μm and 20.7±0.9 μm, respectively. Close up images of the fibers can be seen in **Figure 3.6A**.

Number of layers

Our G-code generator platform allows the user to choose the number of layers, retaining necessary functionality as previously described [22]. For 10 μm target fiber diameter, we chose to print 4 layers (2 layers parallel to the tube length and 2 layers crosshatch, alternating). For 20 μm

target fiber diameter, we chose to print 10 layers (5 parallel to the tube length and 5 crosshatch, also alternating). The number of fibers on each design can be independently controlled (**Figure 3.6**) and allow an extensive range of different MEW scaffolds.

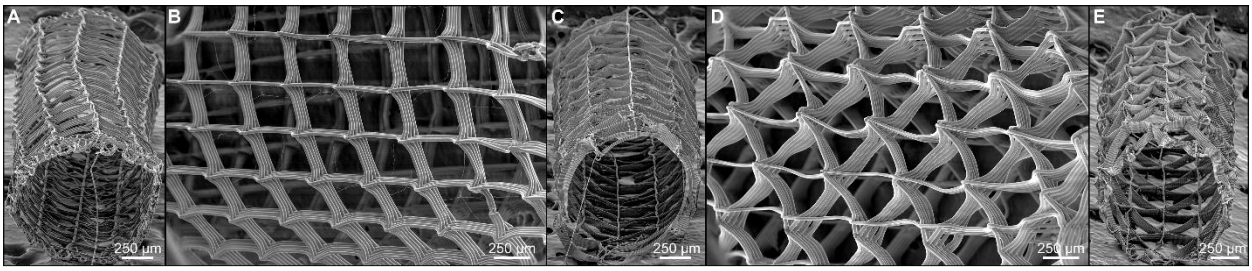

Figure 3.6. Scanning electron microscopy (SEM) of MEW tube scaffolds printed using generated G-code. A) 1 mm tube with a 90° winding angle, B) a 3 mm tube with a 90° winding angle viewed looking at its long axis, C) a 1 mm tube made with a 67.5° winding angle D) a 3 mm tube made with 45° winding angle viewed looking at its long axis and E) a 1 mm tube made with a 45° winding angle.

Together, **Figures 3.5** and 3.**6** demonstrate that the Grasshopper software is effective to produce tubular microfiber scaffolds that match the intended design, down to a 1 mm mandrel diameter and is therefore a viable software platform to generate both virtual and physical scaffold prototypes. This adapts a widely recognized software from the architecture sector for use in creating microfiber scaffolds at significantly smaller scales than is typically employed.

4. Conclusion

We have designed a G-code generator for tubular MEW scaffolds with the ability to iterate and visualize fiber paths using Rhino and Grasshopper. This software was selected as it has a large user community and user-friendly interface with accessible controls for parametric design. In tubular fabrication for MEW, geometric parameters such as tube dimensions, fiber spacing, and the

number of layers, are not commonly controllable by the user in existing modeling systems. Through use of a set of initial printing parameters to help the user achieve a specific fiber diameter, the generator holds the potential to translate MEW designs into different G-code printing languages for a variety of printing platforms.

Since MEW requires a single, continuous fiber to be deposited onto a collector, the ability to properly and accurately visualize what a final print will look like can be challenging and is often achieved by tediously test printing each iteration and seeing its physical presence. By utilizing parametric tools, the user would only need to input minimal and impactful parameters (scaffold length and diameter, fiber diameter, etc.) and an accurate model of the finished scaffold could be digitally rendered. As observed throughout this research, the methods explored allowed for increased variety of tubular design via the incorporation of parallel fibers and a revolution based winding angle. With these differences, our workflow offers a significant reduction in production time and in producing variable outcomes. In addition, tools developed with Grasshopper can be easily shared with a wider community by uploading them to public online repositories, such as Food4Rhino (https://www.food4rhino.com/) for a design users, or GitHub (https://github.com/), a popular platform where developers store and share their code.

MEW users currently face the challenge of designing and producing scaffolds without the convenience of slicing software, as is provided by other 3D fabrication methods. These challenges in design and production are amplified for MEW of tubular structures, where calculation of translational speed of the axis requires complex calculations. Further, additional verification by physical prototype iteration is required to ensure the continuous polymer thread is accurately placed and of desired fiber diameter. Our work addresses these limitations by providing dimensionally accurate 3D renders of tubular scaffolds via the creation of a G-code generator

developed on software that have substantial use in other industries, such as design and architecture. This work contributes to the AM field by demonstrating that predicted tubular designs correspond to accurately positioned fibers onto tubular collectors, resulting in well-formed MEW tubes.

5. Acknowledgements

The technical assistance of Simon Luposchainsky and Dr. Biranche Tandon is greatly appreciated. The project was funded by the Environmental Initiative Curriculum Award from the University of Oregon. P.D.D. is supported by the Bradshaw and Holzapfel Research Professor in Transformational Science and Mathematics Fund. G.VdL. is funded by the Knight Campus Undergraduate Research Program (KCUS). K.L.O. appreciates the KCUS fund. N.C.P acknowledges funding support from the Knight Campus-PeaceHealth Postdoctoral Fellowship Program and Advance Queensland Industry Research Fellowship (AQIRF2020).

6. Conflict of Interest

The authors declare no conflict of interest.

7. Author Contributions

K. L. O. and T. M. contributed equally to this publication.

8. Data Availability Statement

The data that support the findings of this study are openly available in ScholarsArchive@OSU at https://ir.library.oregonstate.edu/concern/articles/vt150s729, reference number vt150s729.

8. References

[1] S. Zhang, *Nature Biotechnology* **2004**, 22, 151.

[2] M. Laubach, B. Herath, N. Bock, S. Suresh, S. Saifzadeh, B. L. Dargaville, J. McGovern, M.-L. Wille, D. W. Hutmacher, F. Medeiros Savi, *Frontiers in Bioengineering and Biotechnology* **2023**, 11.

[3] B. Herath, M. Laubach, S. Suresh, B. Schmutz, J. Paige Little, P. K. D. V. Yarlagadda, D. W. Hutmacher, M.-L. Wille, *Virtual and Physical Prototyping* **2023**, 18, e2246434.

[4] H. Haag, P. D. Dalton, V. Bloemen, *Advanced Functional Materials* **2022**, 32, 2201414.

[5] F. Girard, C. Lajoye, M. Camman, N. Tissot, F. B. Pedurand, B. Tandon, D. Moedder, I. Liashenko, S. Salameh, P. D. Dalton, M. Rielland, *Advanced Functional Materials* **2024**, n/a, 2314757,

[6] N. T. Saidy, A. Fernández-Colino, B. S. Heidari, R. Kent, M. Vernon, O. Bas, S. Mulderrig, A. Lubig, J. C. Rodríguez-Cabello, B. Doyle, D. W. Hutmacher, E. M. De-Juan-Pardo, P. Mela, *Advanced Functional Materials* **2022**, 32, 2110716.

[7] K. L. O'Neill, P. D. Dalton, Small Methods 2023, 7, e2201589.

[8] I. Pennings, E. E. van Haaften, T. Jungst, J. A. Bulsink, A. J. W. P. Rosenberg, J. Groll, C. V. C. Bouten, N. A. Kurniawan, A. I. P. M. Smits, D. Gawlitta, *Biofabrication* **2019**, 12, 015009.

[9] K. F. Eichholz, I. Gonçalves, X. Barceló, A. S. Federici, D. A. Hoey, D. J. Kelly, *Additive Manufacturing* **2022**, 58, 102998.

[10] D. W. Hutmacher, *Biomaterials* **2000**, 21, 2529.

[11] C. Böhm, P. Stahlhut, J. Weichhold, A. Hrynevich, J. Tessmar, P.D. Dalton, *Small* **2021** 18, 202104193.

[12] M. A. Woodruff, D. W. Hutmacher, *Progress in Polymer Science* **2010**, 35, 1217.

[13] N. T. Saidy, F. Wolf, O. Bas, H. Keijdener, D. W. Hutmacher, P. Mela, E. M. De-Juan-Pardo, *Small* **2019**, 15, 1900873.

[14] N. T. Saidy, T. Shabab, O. Bas, D. M. Rojas-González, M. Menne, T. Henry, D. W. Hutmacher, P. Mela, E. M. De-Juan-Pardo, *Frontiers in Bioengineering and Biotechnology* **2020**, 8.

[15] E. Pickering, N. C. Paxton, A. Bo, B. O'Connell, M. King, M. A. Woodruff, *Advanced Engineering Materials* **2022**, 24.

[16] F. M. Wunner, M. L. Wille, T. G. Noonan, O. Bas, P. D. Dalton, E. M. De-Juan-Pardo, D. W. Hutmacher, *Adv Mater* **2018**, 30, e1706570.

[17] O. Bas, S. Lucarotti, D. D. Angella, N. J. Castro, C. Meinert, F. M. Wunner, E. Rank, G. Vozzi, T. J. Klein, I. Catelas, E. M. De-Juan-Pardo, D. W. Hutmacher, *Chemical Engineering Journal* **2018**, 340, 15.

[18] J. C. Kade, P. F. Otto, R. Luxenhofer, P. D. Dalton, *Polymers for Advanced Technologies* **2021**, 32, 4951.

[19] E. McColl, J. Groll, T. Jungst, P. D. Dalton, *Materials & Design* **2018**, 155, 46.

[20] D. D. G. Cuevas, D. G. Puglliese, Advanced 3D Printing with Grasshopper®: Clay and FDM, *Independently Published*, **2020**.

[21] K. A. van Kampen, T. ten Brink, C. Mota, L. Moroni, *Small Structures* **2024**, 5, 2300399.

[22] S. Ashour, L. Du, X. Zhang, S. Sakurai, H. Xu, *European Polymer Journal* **2024**, 204, 112675.

[23] Y. Chen, Z. Zou, T. Fu, Z. Li, Z. Zhang, M. Zhu, Q. Gao, S. Wu, G. Fu, Y. He, J. Fu, *International Journal of Extreme Manufacturing* **2024**, 6, 035503.

[24] A. R. Mridha, T. R. Dargaville, P. D. Dalton, L. Carroll, M. B. Morris, V. Vaithilingam, B. E. Tuch, *Tissue Eng Part A* **2022**, 28, 212.

CHAPTER 4: HIGH PRECISION FIBER PRINTING OF SEMI-CRYSTALLINE AND AMORPHOUS POLYMER MATERIALS TO CREATE 3D PRINTED TUBULAR SCAFFOLDS PRODUCED BY MELT ELECTROWRITING

This chapter presents the development of a high-precision MEW printer capable of producing tubular scaffolds from PCL and PLCL. The research integrates advanced manufacturing and design to fabricate multi-material tubes that combine design with biological purpose.

Scientific Contribution and Advancement of Knowledge

This work outlines how MEW can be adapted to fabricate high-resolution tubular architectures from different materials. By designing and constructing a custom four-axis MEW system with digitally synchronized control of voltage and pressure, the research introduces a robust platform for printing both semi-crystalline and amorphous polymers. The successful direct printing of PLCL, an elastomeric copolymer, demonstrates an advance in MEW processability by overcoming previous limitations that required thermal preconditioning. Furthermore, the introduction of multi-material tubular scaffolds made by combining aligned PLCL fibers for axial compliance with PCL crosshatches for radial reinforcement represents a significant innovation in scaffold design.

Broader Implications and Future Directions

Inspired by tissue architecture and function, this work demonstrates how precise fiber deposition and material selection can be leveraged to achieve complex multi-material geometries via MEW. Through these advances, the work contributes to the long-term vision of producing clinically viable, patient-specific conduits for applications in TE.

Abstract for “High Precision Fiber Printing of Semi-Crystalline and Amorphous Polymer Materials to Create 3D Printed Tubular Scaffolds Produced by Melt Electrowriting”

MEW enables the production and deposition of polymer microfibers for architected scaffolds which have been applied to TE applications. In this chapter, we describe a high-resolution custom four-axis MEW system based on an Aerotech motion platform with digitally synchronized pressure and voltage control, a high-temperature printhead, and a dual-collector assembly for rapid switching between planar and tubular modes. Using PCL and PLCL, we precisely place fibers onto tubular collectors, focusing on scaffold design for unique mechanical properties. This includes 1) aligned PLCL fibers along the length of the tube that maintain longitudinal flexibility while providing topographical cues together with 2) wound PCL microfibers that resist compression of tube during manipulation. We demonstrate direct tubular printing of PLCL without extended pre-conditioning and establish a multi-step workflow to fabricate multi-material tubes with aligned PLCL for alignment cues and axial compliance followed by PCL crosshatches for radial reinforcement. This chapter offers a section on future work which proposes studying the mechanical profile of multi-material tubular constructs evaluated via tension and compression. Future work could also explore how Schwann cells align along PLCL fibers. This platform expands the accessible design space for MEW tubular scaffolds towards TE applications.

1. Introduction

Melt electrowriting (MEW) is a high-resolution 3D-printing technology developed over a decade ago [1]. As the technology continues to develop, studies have focused on several processing achievements and limitations, including when flat, tubular and non-planar collectors are used. While flat MEW scaffolds predominate in the literature, tubular scaffolds have been studied for their mechanical properties [2,3,4]. Limitations occur, for example, when fibers are positioned parallel and near each other leading to imperfections called fiber bridging. Fiber bridging depends on several factors including the fiber diameter and number of fibers already deposited. This minimal inter-fiber distance was reported by Kim *et al.* 2021 onto flat collectors [5], and there remains a knowledge gap of how fiber bridging occurs on tubular MEW scaffolds. This is important for several applications within tissue engineering (TE) for MEW tubes where the resolution limits of MEW processing limit the possible design space. To quantify these limitations, there is a requirement for a high-resolution printer to achieve the level of toolpath design necessary to induce or avoid fiber bridging.

In this work, we designed, built and fully described a custom-built MEW printer using a high-resolution Aerotech axis system. The advantages of this system include a ceramic-heater printer head designed for glass syringes which withstand higher temperatures needed to MEW-process different materials. Indeed, the use of custom-built MEW printers has driven the growth in demonstrating the polymers that can be processed with this technology [6]. While the gold standard material for MEW processing is PCL due to its low melting point and high processability, almost all commercial MEW printers are designed and limited to process this specific polymer. This paper focuses on studying minimal inter-fiber distance (without fiber bridging) by varying

winding angle and end-loop design while maintaining overall scaffold dimensions (inner diameter and length) and fixed fiber diameter and layer number (wall height) of PCL constructs.

In parallel, PLCL is of interest for the field of biomedical engineering due to its more elastic material properties. However, processing PLCL with MEW using a syringe requires a prolonged (24-48 h) and elevated temperature of (150 °C) [7] which results in hydrolytic degradation affecting the viscosity and resulting processing outcomes. In this study, PLCL tubes with aligned fibers are made by printing at 165 °C using pellets that have undergone a drying step to reduce their water content.

Minimum mechanical properties of a nerve guide are fundamental to its success after implantation. A conduit must maintain structural integrity throughout the regeneration period while remaining flexible enough to accommodate movement of the surrounding tissue. If the conduit is too rigid, it may cause irritation or further damage the surrounding tissue, leading to fibrosis or impaired regeneration. Alternatively, insufficient stiffness can result in collapse or kinking that obstructs axonal growth. Therefore, achieving a balance between elasticity and compressive strength is crucial to preserving lumen patency and guiding axonal extension over the injury gap.

In this work, a multi-step print is employed to tackle a multi-material approach that combines the semi-crystalline and amorphous materials of PCL and PLCL respectively. We design and manufacture tubular scaffolds to have aligned PLCL fibers along the tube length, allowing stretchability and shape recovery following tensile strain. The PLCL aligned fibers are subsequently reinforced with a crosshatch PCL that improves resistance to compression.

Beyond mechanical stability, the topographical alignment of fibers provides essential biological guidance for cellular organization. In peripheral nerve repair, aligned microstructures have been shown to direct Schwann cell elongation and orientation along fibers. Therefore,

scaffolds designed to present longitudinally aligned fibers offer topographical cues to promote cellular alignment.

Together, these design considerations and processing strategies evaluate how printer components and modifications, printing parameters, material combinations, and scaffold architecture influence the fiber placement and structural fidelity of a MEW-printed tubular scaffold.

2. Results and Discussion

2.1. Design, development and assembly of high-end MEW printer

2.1.1. Motion System and Frame

The printer frame is constructed from 40 mm square aluminum t-slot extrusions with a square 730 mm footprint. A square aluminum plate serves as the base plate for the orthogonal Y-X axis assembly and custom rotational A axis components. The Z axis and printhead assembly are mounted directly to two aluminum crossbeams which run parallel to the X axis and form the gantry of the device.

Linear stages X-Y-Z consist of PRO115SL Ballscrew stages and closed-loop BMS60 servo motors with the Z axis motor BMS60-M2 containing an additional brake (Aerotech, USA). The rotational A axis consists of a closed-loop BMS35 servo motor (Aerotech, USA) on a custom machined PEEK mount, ball bearings and transmission using a 2 mm pitch timing belt to the rotating mandrel. All motors and linear stages form the Aerotech motion system and are controlled with four Automation1-XC4 PWM drives from a desktop using A3200 software and programmed in AeroBasic language (Aerotech Inc., USA). The printer further features a synchronous control of printing parameters including voltage and pressure, as described in Section 2.1.5.

2.1.2. Custom designed print head

The printhead consists of a PEEK housing surrounding a ceramic plate assembly with two zones of resistive ceramic heaters and K-type thermocouples. Inside this stack, a 3 mL glass syringe and needle can be inserted and fixed with a threaded end cap, connecting the nozzle to the brass HV electrode and sealing the pneumatic connection to pressurize the system for printing. The high voltage connection is made directly to the brass plate via high temperature solder, and the cable held by the PEEK end cap at the bottom of the print head, which is fastened with M2 PEEK screws. A complete schematic of the printer head is shown in **Figure 4.1**.

2.1.3. Dual collector design

Flat collector

The flat collector was grounded via a wire secured beneath the aluminum plate to ensure stable electrostatic conditions during MEW. The placement and distance relative to the A-axis mount were carefully optimized to minimize potential arcing or voltage interference that can naturally occur during high-voltage operation.

Tubular collector

A key feature of the printer design is the dual-collector system, which enables switching between flat and tubular collection modes. The tubular collector was refined through the incorporation of a custom-fabricated brass support that stabilizes the mandrel during rotation by the chuck. This configuration effectively eliminates mandrel wobble, ensuring precise alignment and highly consistent fiber deposition on the curved surface of the tubular collector.

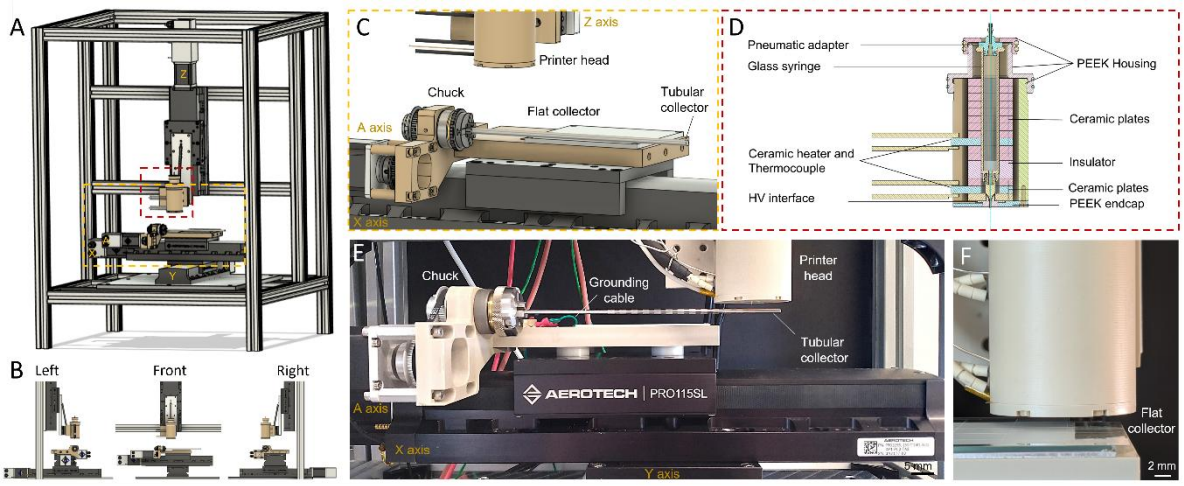

Figure 4.1. Custom built Aerotech printer system. A) Fusion 360 render of MEW printer using Aerotech axis system. B) Left, front and side views of render. C) Close up of render of axis system and collectors. D) Render of printer head components. More detailed schematic is shown in Supporting Figure S4.1. E) Photograph of printer for tubular printing. F) Close up photograph of printer for flat collector.

2.1.4. Hardware to control voltage, pressure and temperature

Voltage was regulated through an interface supplied by Matsusada Precision Inc. (Japan). Air pressure was controlled using an electro-pneumatic regulator (SMC Corporation, Japan). Independent temperature regulation for both the syringe barrel and nozzle tip was achieved via a dual-channel heating system from Bach Resistor Ceramics GmbH (Germany). This configuration provided precise and stable thermal, electrical, and pneumatic control, ensuring consistent material flow and fiber deposition throughout the printing process.

2.1.5. Digital integration for voltage and pressure control

Digital control of the applied voltage and air pressure was achieved by interfacing each respective controller with the X-axis drive of the Aerotech motion system. A 21-pin cable connected to the rear of the voltage supply contained a dedicated soldered pin linked directly to

the X-axis drive. In parallel, the pressure controller was similarly connected to enable synchronized communication and control. This configuration allowed programmable, real-time adjustment of voltage and pressure parameters through the motion control software. Such integration facilitates precise tuning of printing conditions during the fabrication of multi-layered or tall structures. By enabling progressive adjustments such as incrementally increasing voltage in tandem with rising scaffold height, the system maintains stable jet formation and deposition accuracy throughout extended print durations.

2.2. Scaffold design

PCL scaffolds were fabricated using mandrels with diameters of 3 mm and 1 mm. The rotation angle was adjusted based on pivot points described in prior studies by McColl *et al.* [2] and Pickering *et al.* [4], with the present design exhibiting significantly higher angular density (approximately 60° compared to 18° in previous works). Variations in end-loop geometry were also explored to evaluate their influence on structural continuity and ease of fabrication. Future iterations of scaffold design could benefit from the integration of parametric modeling tools, such as G-code generation using Rhinoceros/Grasshopper, which would facilitate real-time visualization and optimization of print paths prior to fabrication [8].

2.2.1. Investigating minimal inter-fiber distance of PCL fibers on tubular mandrels

To assess the resolution limits of the MEW process on curved surfaces, PCL fibers with diameters of approximately 10 μm were deposited on tubular mandrels of 3 mm and 1 mm diameter (**Figure 4.2**). These conditions replicate those used in previous studies on fiber bridging while extending the analysis to tubular geometries. The resulting structures demonstrated precise fiber placement with minimal inter-fiber spacing.

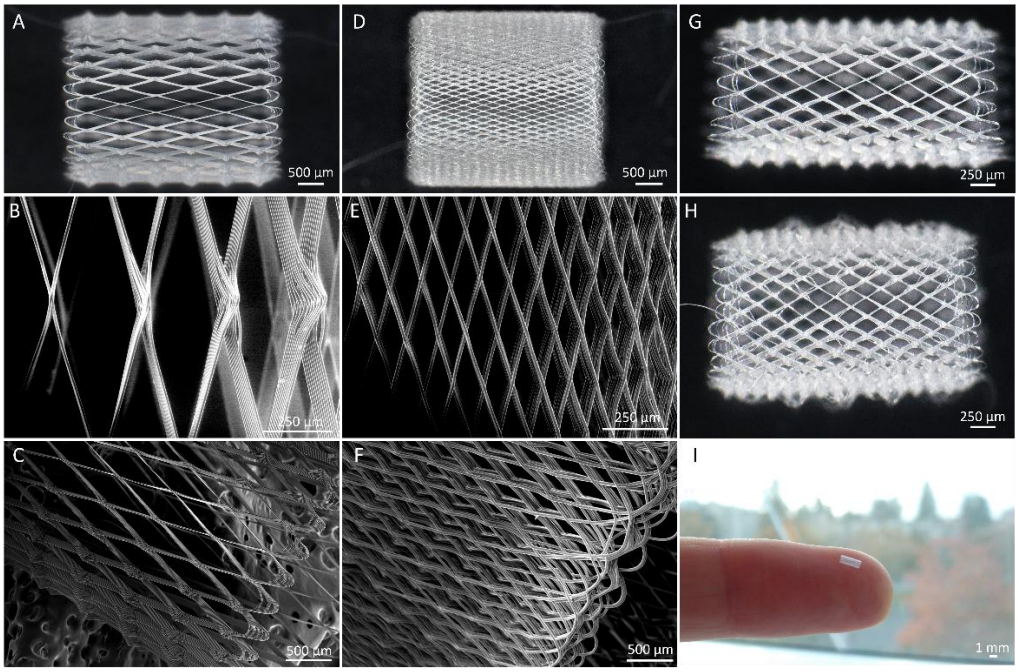

Figure 4.2. Evaluation of minimal inter-fiber distance with PCL achieved on tubular collector of 3 mm and 1 mm diameter for 10-layer scaffolds of 10 µm fibers. A) Optical microscope images of PCL scaffolds with 385 µm spacing; B and C) corresponding SEM images. D) Optical microscope images of PCL scaffolds with 159 µm spacing; E and F) corresponding SEM images. G and H) Optical microscope images of PCL scaffolds of 1 mm inner diameter with 157 µm and 120 µm inter-fiber spacing, respectively. I) Photograph of 1 mm tube on a finger. Scale bars: A, C, D and F) 500 µm; B, E, G and H) 250 µm; I) 1 mm.

2.2.2. Achieving tubular constructs with PLCL

Tubular scaffolds were also fabricated using PLCL to evaluate the feasibility of printing highly elastic structures. PLCL was selected for its favorable mechanical properties, including enhanced flexibility and elongation at break. Tubes were fabricated on 3 mm diameter mandrels using optimized processing parameters to ensure uniform fiber deposition and smooth layer transitions. The resulting PLCL scaffolds (**Figure 4.3**) demonstrated fiber continuity and conformal wrapping around the mandrel, confirming the material's suitability for stable jet

formation under MEW conditions. **Figure 4.3** shows tubes with midrange-to-midrange fiber spacings of 935 µm and 525 µm. The individual fiber diameter was measured at 17.5 ± 1.2 µm.

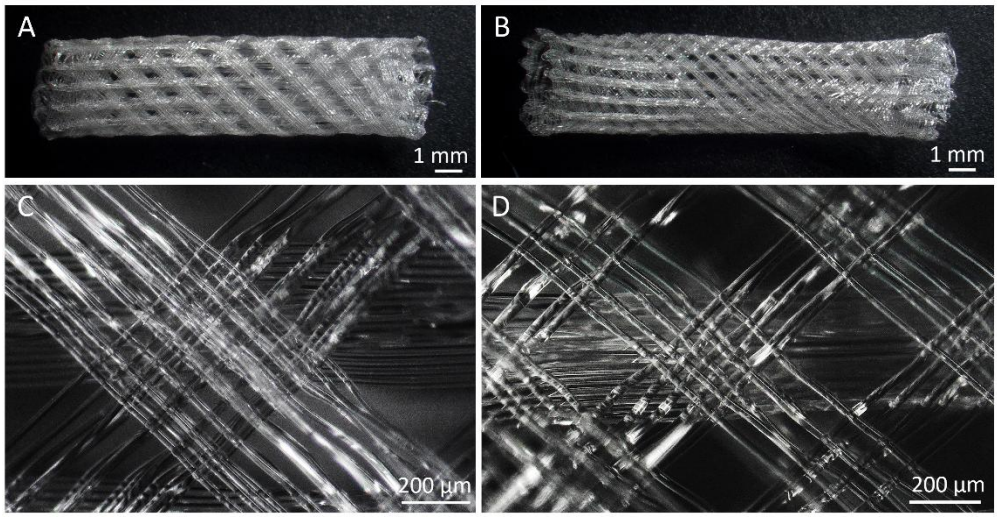

Figure 4.3. Light microscope images of PLCL tubes printed onto a 3 mm diameter mandrel showing A) midrange to midrange spacing of fibers at 935 µm spacing, and B) midrange to midrange spacing of fibers of 525 µm spacing with close-up in C and D) respectively. Individual fiber diameter: 17.5 ± 1.2 µm. Scale bars: A and B) 1 mm; C and D) 200 µm.

2.3. Multi-step prints for multi-material scaffolds

The accuracy of multi-material deposition was evaluated using light microscopy to assess fiber alignment, layer registration, and material interfaces. Representative images of printed PCL and PLCL tubes confirmed that both polymers maintained uniform fiber morphology and consistent deposition throughout the print. The alignment of PLCL fibers within the inner layer and the crosshatch configuration of PCL in the outer layer were well preserved, demonstrating high spatial precision and minimal distortion during material switching.

Figure 4.4 illustrates the design and outcome of the multi-material tubular scaffolds. Panel A presents a digital render showing the intended architecture, with PLCL fibers represented in

orange and PCL fibers in blue. Panel B displays a light microscope image of the printed construct, highlighting the distinct layers: aligned PLCL fibers (enlarged in C) and the outer PCL crosshatch (enlarged in D).

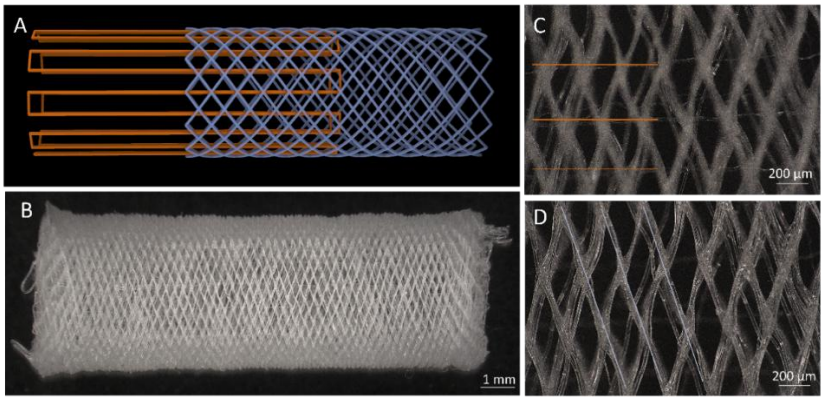

Figure 4.4. Multi-material tubular prints. A) Digital render with PLCL (orange) and PCL (blue). B) Light microscope image of printed tube with PLCL aligned fibers (enlarged in C) and PCL crosshatch (enlarged in D). Scale bars: B) 1 mm; C and D) 200 µm.

3. Experimental section

3.1. MEW processing of PCL and PLCL

Scaffolds were fabricated using a custom-built MEW printer as described in the results section. PCL polymer pellets were loaded into a 3 mL glass syringe (Fortuna Optima, Poulten & Graf GmbH, Germany) fitted with a stainless-steel nozzle (brand, country to be completed later) connected via a Luer lock system. The nozzle tip was trimmed to protrude approximately 1 mm beyond the printhead to ensure a stable electrohydrodynamic jet.

For PCL, the syringe was inserted into the MEW printhead and heated to 75 °C until the polymer was fully molten (approximately 1 h for initial heating and 20 min for subsequent uses). An air pressure of 1.5 bar was applied to extrude the molten polymer through the nozzle at controlled rates, producing target fiber diameters of either 10 µm or 20 µm. The collector distance

(the distance between the nozzle tip and the grounded collector) was maintained at 3 mm for all experiments. A constant voltage of 5.5 ± 0.5 kV was applied throughout all printing sessions, with ambient conditions maintained at 20.5 ± 1 °C and relative humidity at 35 ± 1%. Temperature and humidity were continuously monitored using a wireless sensor (Tempy2, USA). To achieve the different fiber diameters, specific nozzle gauges and parameters were used: 25G for 10 μm fibers used to study minimal inter-fiber distance while reinforcement fibers of approximately 20 μm were printed using a 23 G nozzle.

For PLCL, polymer pellets were dried overnight at 60 °C before loading into glass syringe fixed with a 23 G nozzle. MEW processing was equivalent to PCL, but with different printing parameters: printing temperature: 165 °C, applied pressure of 0.75 bar, collector speed of 4.25 mm/second, voltage applied of 4.5 kV. Printing parameters will be finalized and then included in this manuscript.

3.2. Light microscopy

Scaffold morphology and fiber alignment were examined using a digital light microscope (Keyence, Japan). Samples were imaged under brightfield illumination at multiple magnifications to assess overall structural integrity and uniformity.

3.3. Scanning Electron Microscopy (SEM)

Samples were sputter-coated with a 7 nm titanium layer before imaging using a Thermo Fisher Apreo 2 scanning electron microscope (Thermo Fisher Scientific, USA) equipped with an Everhart-Thornley secondary electron detector (ETD). Representative regions were imaged at varying magnifications to assess fiber morphology and uniformity.

4. Conclusion

This work opens new design possibilities for customizable, high-fidelity tubular scaffolds tailored to bioengineering applications by incorporating multi-material tubular printing via MEW.

5. Future work

Future work includes inspection of fiber-fiber morphology of the presented multi-material constructs using SEM, quantifying mechanical performance and assessing SC responses to aligned topographical cues. Mechanical properties of the MEW tubular scaffolds could be evaluated using a dynamic mechanical analyzer. The biological evaluation of the printed scaffolds could focus on how the aligned PLCL fibers offer topographical features to study the influence on SC behavior.

6. References

[1] K. L. O'Neill, P. D. Dalton, *Small Methods* **2023**, 7, e2201589.

[2] E. McColl, J. Groll, T. Jungst, P. D. Dalton, *Materials & Design* **2018**, 155, 46.

[3] N. C. Paxton, R. Daley, D. P. Forrestal, M. C. Allenby, M. A. Woodruff, *Materials & Design* **2020**, 193.

[4] E. Pickering, N. C. Paxton, A. Bo, B. O'Connell, M. King, M. A. Woodruff, *Advanced Engineering Materials* **2022**, 24.

[5] J. Kim, E. Bakirci, K. L. O'Neill, A. Hrynevich, P. D. Dalton, *Macromolecular Materials and Engineering* **2021**, 306.

[6] J. C. Kade, P. D. Dalton, *Adv. Healthcare Mater*. **2020**, 202001232.

[7] R. Sanchez Diaz, J. R. Park, L. L. Rodrigues, P. D. Dalton, E. M. De-Juan-Pardo, T. R. Dargaville, *Advanced Materials Technologies* **2021**, 7.

[8] K. L. O'Neill, T. McLoughlin, G. Van der Linden, I. Lopez Buson, N. C. Paxton, M. Polites, P. D. Dalton, *Virtual and Physical Prototyping* **2025**, 20.

CHAPTER 5: TAILORING CELL ATTACHMENT ONTO MELT ELECTROWRITTEN SCAFFOLDS VIA A PHASE-SEPARATED HYDROGEL COATING WITH PEPTIDE FUNCTIONALIZATION

O'Neill KL, Kurtz A, Liashenko I, Rocha G, Paxton NC, Dalton PD. (2024) Tailoring Cell Attachment onto Melt Electrowritten Scaffolds via a Phase Separated Hydrogel Coating with Peptide Functionalization. *Advanced Interface Technologies*, **12**, 2400692.

This chapter presents a novel strategy to biofunctionalize MEW scaffolds through the integration of phase-separated pHEMA hydrogels, enabling precise control of cell attachment via peptide modification. The work demonstrates how phase separation and peptide functionalization can be harnessed to introduce hydrophilic, bioactive interfaces onto microscale PCL scaffolds without compromising structural fidelity. By capturing pHEMA droplets during polymerization and functionalizing them with cysteine-terminated RGD peptides, this approach establishes a tunable system for directing cell attachment.

Scientific Contribution and Advancement of Knowledge

This chapter combines microscale fiber architecture with hydrogel-based biochemical functionality. The phase-separated pHEMA coating introduces a hydrated, porous interface on PCL fibers, increasing surface area while reducing nonspecific protein adsorption. Functionalization with the RGD peptide sequence restores cell adhesion through integrin-mediated interactions, as demonstrated by enhanced fibroblast metabolic activity and increased cellular processes compared to unmodified controls. The work elucidates how reaction timing, water content, and peptide concentration govern coating morphology and biological response, revealing new physicochemical principles for peptide incorporation within hydrogels. By integrating polymer

chemistry and 3D printing, the study provides a framework for designing scaffolds with programmable surface bioactivity.

Broader Implications and Future Directions

This work contributes broadly to the fields of biofabrication, biomaterials science, and regenerative medicine. The demonstrated integration of phase-separated hydrogel chemistry with MEW scaffolds introduces a versatile strategy for modulating cell-material interactions in 3D scaffolds. The methodology could be extended to various peptide sequences and cell types, offering opportunities to design scaffolds that elicit customized biological responses.

Tailoring Cell Attachment onto Melt Electrowritten Scaffolds via a Phase Separated Hydrogel Coating with Peptide Functionalization

*Kelly L. O'Neill[1], Amanda Kurtz[1], Ievgenii Liashenko[1], Guilherme Rocha[1], Naomi C. Paxton[1,2], Paul D. Dalton[1,] **

1. Department of Bioengineering, Phil and Penny Knight Campus for Accelerating Scientific Impact, University of Oregon, 1505 Franklin Boulevard, Eugene, OR 97403-6231, USA

2. Centre for Biomedical Technologies (CBT), Queensland University of Technology (QUT), Brisbane 4000, Australia

** Corresponding author: Paul D. Dalton pdalton@uoregon.edu

Keywords: melt electrowriting, poly(ε-caprolactone), poly(2-hydroxyethyl methacrylate), 3D cell culture, RGD peptide

Abstract for “Tailoring Cell Attachment onto Melt Electrowritten Scaffolds via a Phase Separated Hydrogel Coating with Peptide Functionalization”

Highly porous scaffolds with a high surface area can be designed and fabricated via melt electrowriting (MEW). Here, we introduce morphological features onto the MEW microfibers via a hydrogel coating of phase-separated poly(2-hydroxyethyl methacrylate) (pHEMA). This coating is achieved by capturing phase separated droplets of pHEMA onto poly(ε-caprolactone) (PCL) microfibers via dip-coating, resulting in a hydrogel coating with webbed structures across pores of the MEW scaffold. Excess pHEMA droplets are removed and phase separation is quenched by washing in water, and then functionalized by dipping the pHEMA coated scaffold into a buffered peptide solution. We demonstrate that a cysteine-terminated peptide sequence (Cys-Gly-Arg-Gly-Asp-Ser-Gly (CG-RGD-SG)) promotes fibroblast adhesion on the hydrogel-coated MEW scaffolds compared to unmodified pHEMA and compared to scrambled peptide sequence. Due to the protein resistant nature of pHEMA, the hydrogel-coated scaffolds show less cell attachment than non-coated PCL scaffolds, while RGD-functionalized pHEMA scaffolds achieve 2.8-fold increase in cell attachment ($p=0.02$) when compared to non-functionalized pHEMA. We therefore present a platform which combines PCL scaffolds of microscale fibers with a phase-separated pHEMA hydrogel coating that maintains the high porosity of MEW scaffolds yet increases surface area and, importantly, introduces the capability for tailoring cell attachment via peptide functionalization.

1. Introduction

Melt electrowriting (MEW) is a high-resolution 3D printing technology first described over a decade ago[1]. Used primarily for fabricating biomedical materials, MEW deposits microscale polymer fibers layer-by-layer to create high resolution and well-organized porous scaffolds, often intended to resemble the microarchitecture of native tissue. MEW products are of interest for a wide range of applications including tissue engineering (TE) and cancer research. Medical-grade poly(ε-caprolactone) (PCL) is the current gold standard material for MEW due to high processibility: low melting point (60 °C) and high thermal stability (up to 160 °C). However, like most thermoplastics, PCL is hydrophobic, inducing unspecific protein adsorption and consequently uncontrolled cell attachment[2]. Controlled and defined cell-biomaterial interactions are desired both *in vitro*[3, 4] and *in vivo*[5, 6], and therefore facilitating biological function with reduced protein adsorption is a widely appreciated approach for the development of scaffolds for biomedical applications.

Studies combining MEW with hydrogels have primarily focused on the mechanical properties of the constructs through fiber reinforcement[7-9]. Early research using MEW scaffolds to reinforce gelatin methacrylate (GelMA) discovered that the mechanical properties of the scaffold/gel combination increased by up to 54-fold compared with either of its components alone[7]. This combination of highly porous MEW scaffolds reinforced with GelMA was tailored to match the mechanical properties of native cartilage. In the context of cardiac TE, Saidy *et al.* embedded a heart valve MEW scaffold in an elastin-like hydrogel to develop a soft-network composite favoring cell infiltration and ensuring hemocompatibility[10]. Similarly, for neural TE, Janzen *et al.* used thiolated hyaluronic acid reinforced PCL mesh in an ultra-soft matrix to co-culture neurons and astrocytes to promote neuronal viability[11]. Taking advantage of the topographical cues,

microfibers can be used to guide directed cell growth. Kriebel *et al.* showed aligned fibers embedded in collagen orient neural cells along the fibers[12]. Further, oriented fibers have been used to overcome barrier-like characteristics in neural studies[13].

Hydrogels can be combined with cell-specific biofunctional molecules such as peptides that promote cell attachment and growth. Current approaches for development of such modified platforms are highly dependent on click chemistry onto synthetic hydrogels such as poly(ethylene glycol) (PEG), where peptide sequences are introduced within the bulk hydrogel[14].

The advantages of combining MEW scaffolds with hydrogels can be broken down into 1) reinforcement and tailorable mechanical properties, 2) cell alignment within soft hydrogel environment and 3) reservoir for water-soluble biomolecules. In a more recent study, MEW scaffolds were biofunctionalized via coating with six-arm star-shaped NCO-poly(ethylene oxide-stat-propylene oxide) (sP(EO-stat-PO)) which minimizes unspecific interactions with proteins and cells[15]. However, even though this process allows for the incorporation of large proteins (streptavidin and collagen) that introduce specific functionalities onto the surface of MEW fibers, coating required glove boxes to work with sP(EO-stat-PO), while the specialty polymer is not commercially available.

First discovered in the 1960's[16], poly(2-hydroxyethyl methacrylate) (pHEMA) was initially found to be an ideal material for contact lenses and intraocular lens[17] due to its transparency and mechanical properties[18]. PHEMA has been used in FDA cleared products as a biomaterial in TE applications as a delivery system[19] and has a history of pre-clinical and clinical trials[20, 21]. Due to technical challenges in fully removing ethylene dimethacrylate crosslinker[22, 23], pHEMA almost always forms crosslinked hydrogels[24]. When HEMA is polymerized in excess water, phase separation occurs due to micro- or macro-syneresis, depending on the water ratio[25]. At H_2O:HEMA

ratios greater than 3:1, macro-syneresis occurs, resulting in a porous hydrogel scaffold. Originally termed pHEMA "sponges", these phase-separated materials demonstrated cellular invasion *in vitro* and *in vivo*[26-28]. More recently, drug delivery from phase-separated pHEMA hydrogels have been studied, tailoring release by varying the monomer/crosslinker concentration, solvent mixture, and reaction temperature[29]. PHEMA gels may also be prepared by free radical polymerization of a continuous phase of high internal phase emulsion (polyHIPE) with the microstructure and pore size tailorable by the crosslinker[30]. Such polyHIPE structures can be functionalized by first modifying through halodehydroxylation to improve leaving group residues comparatively to the hydroxyl group[31], providing options to the surface chemical modification of sponges with tailorable porosity. Alternatively, pHEMA hydrogels may be prepared by photocrosslinking, where photoinitiator concentration and irradiation time affect crosslinking, resulting in different polymer density. The photoinitiator concentration limits the reaction of primary radicals, causing termination of that reaction[32].

Other hydrogels that phase separate upon polymerization include dextran-methacrylate[33]. Varying the methacrylate degree of substitution was found to influence the pore morphology and scanning electron microscopy (SEM) was used to observe the shape and size of pores: higher degrees of methacrylate substitution revealed a compact and rigid pore microstructure, whereas a lower substituted hydrogel presented a more delicate structure with smaller pores[33]. For TE applications, scaffolds need to have interconnected pores to facilitate nutrient diffusivity and cell infiltration. In previous studies, methacrylated dextran was combined with PEG to create macroporous hydrogels. In addition to tailoring the degree of methacrylate substitution on dextran, dextran molar mass and PEG concentration were used to engineer spongy scaffolds with larger pore sizes[34].

In this current work, we propose to further research on hydrogel materials combined with highly porous MEW scaffolds by developing peptide-functionalized hydrogels as coatings that promote cell attachment tailored to specific cell types onto microfiber scaffolds. Specifically, we develop a novel coating process by capturing phase-separated pHEMA droplets on PCL MEW scaffolds, then functionalizing the hydrogel coating with peptides for cell adhesion. As a proof of concept focusing on cell adhesion, we chose the peptide sequence arginine-glycine-aspartic acid (RGD) (full sequence: CG-RGD-SG) and compared this with a scrambled peptide control RGE (full sequence: CGG-RGE-SG).

2. Results and Discussion

2.1. Phase separation and characterization

Phase separation of HEMA occurs when this monomer is polymerized in excess water. First observed in the 1960s, research determined that as the polymer chains grow, they use the remaining monomer as its preferred "solvent". Such liquid-liquid phase separation is leveraged here to generate droplets that coat the PCL microfibers. Ammonium persulfate (APS) and tetramethylethylenediamine (TEMED), which together, initiate a redox reaction to commence the polymerization of the HEMA monomer (**Figure 5.1A**). The resulting hydrogel structure has been described as a "sponge" for decades[25], and has shown cell invasive properties.[28] These "sponges" traditionally result simply by allowing the mixture to complete its reaction (**Figure 5.1B**) where the droplets connect and undergo gelation. This study, however, captures the monomer droplets when phase separation occurs, onto PCL scaffold fibers, and then washes away excess material.

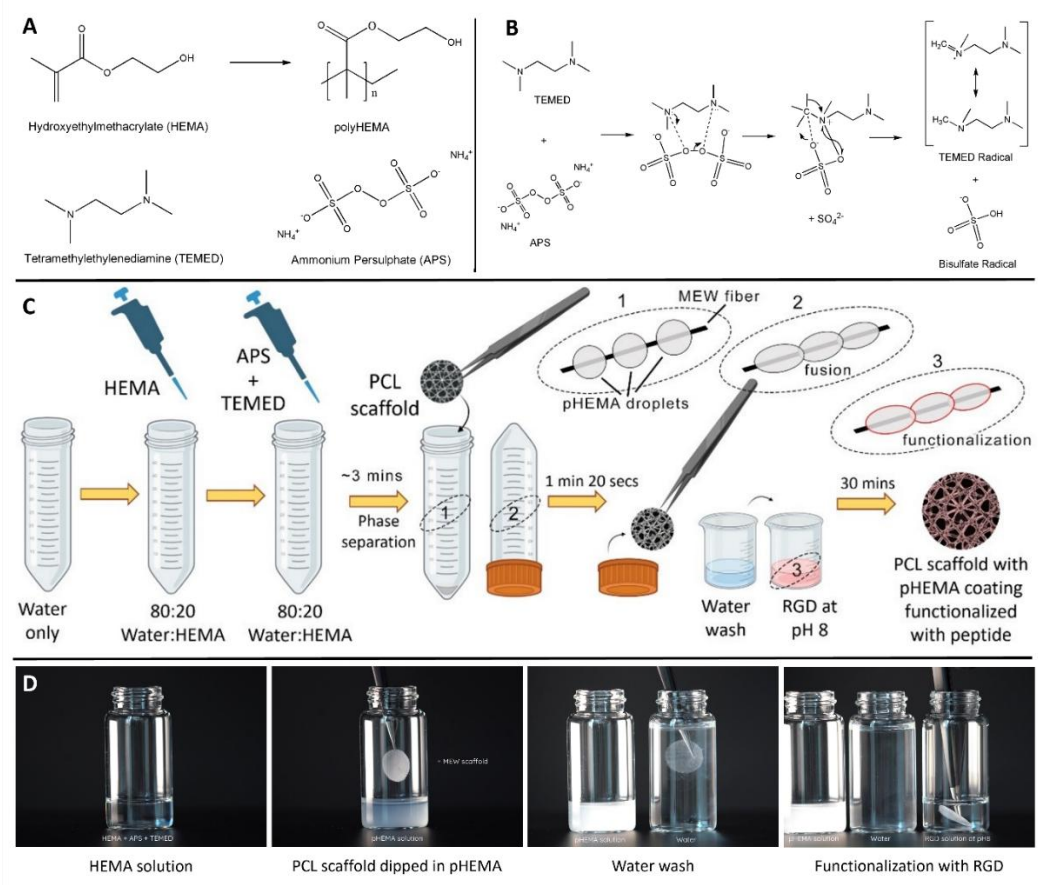

Figure 5.1. Methodology of coating PCL MEW scaffolds with phase-separated pHEMA and subsequent peptide functionalization. A) Chemical structure of monomer/polymer and the initiators of the redox system used to induce free-radical polymerization of HEMA. B) TEMED/APS reaction to form TEMED and bisulfate radicals[35]. C) Schematic of the process adopted in this study, where the phase separation step is used to disperse droplet coatings onto a scaffold that is then quenched in water and functionalized using peptide. D) Screenshots of Supporting Video S5.1 showing methodology: pHEMA polymerization via phase separation is visible by increasing opacity of pHEMA solution. PCL scaffold is placed into pHEMA solution to collect droplets onto polymer fibers. Excess polymer is washed and pHEMA is functionalized by dipping in CG-RGD-SG solution at pH 8. A and B created using ChemDraw Pro version 8.0. ~~B&~~C created with BioRender.com.

In this study, MEW scaffolds were washed in a phase separated HEMA/pHEMA mixture, and transferred in a water washing step that interrupts the coating formation (**Figure 5.1C**). The pHEMA/HEMA liquid droplets become attached to the hydrophobic PCL MEW fibers and form a hydrogel around them. By placing these pHEMA coated PCL scaffolds in water before complete polymerization, we can alter the coating morphology and thickness. We investigated the timing for polymerization by taking advantage of the optical properties of pHEMA. Specifically, since HEMA solution is transparent, and phase separated droplets cause the solution to become opaque over time, we studied the rate of reaction by measuring light absorbance over time (**Figure S5.1,** see section 4.5.1.). Since the polymer coating and wash step are performed within the first 8 min of reaction initiation, the washing step occurs before gelation. **Supporting Video S5.1** shows the phase separation and washing steps of the system. **Supporting Video S5.2** demonstrates the pHEMA droplets coating the scaffold fibers and progressively fusing into a continuous hydrogel network layer, as represented in **Figure 5.1C**. This visualization highlights the successful formation of the coating and provides insight into the mechanism underlying the coating process.

The water content of the bulk pHEMA gels was also measured: after freeze drying, the weight of each sample was recorded. Samples were placed in water at room temperature for 24 h and the weight was measured again. Excess water stored in the pHEMA pores was removed by centrifugation. From the difference in weight, the equilibrium water content was measured as 53.1% (**Equation 1**) [36].

(Eq. 1) $$Equilibrium\ water\ content = \frac{weight\ hydrated - weight\ dry}{weight\ dry} \times 100$$

2.2. Preparation and fabrication of PCL scaffolds

MEW scaffolds were 14 mm in circular diameter to fit a 24-well plate. Scaffolds were fabricated on a custom-built MEW printer as previously described[37]. Two scaffold designs were chosen: square and a triangle morphology, shown in **Figure 5.2A-B** and **D-E**. The 0°/90° square laydown pattern represents a standard morphology for MEW scaffolds[38], which also assists in observing the pHEMA coating bridging within the square pores. The triangle pore scaffolds made with a 0°/36°/72°/108°/144° laydown pattern form more divisions in the x-y directions, due to fiber bridging[39]/suspension[40]. The fiber diameters and inter-fiber distances were measured using light microscope (Keyence measuring tools) and are summarized in **Table 5.1**. A programmed fiber spacing of 250 μm with 11.3 ± 0.6 μm diameter fibers resulted in both square and triangle scaffolds with 96.5% porosity. This estimated value is based on measured MEW fiber size and programmed design (see section 4.6.2.).

Table 5.1. MEW scaffold fiber diameter, inter-fiber distance (non-coated) measured using light microscope (see section 4.3) and porosity via image processing of SEM images (see section 4.6.2).

	Fiber diameter (μm)	Spacing between parallel fibers (μm)	Porosity (%)
Square	11.3 ± 0.6	229.2 ± 10.4	96.5
Triangle	11.3 ± 0.6	235.0 ± 1.7	96.5

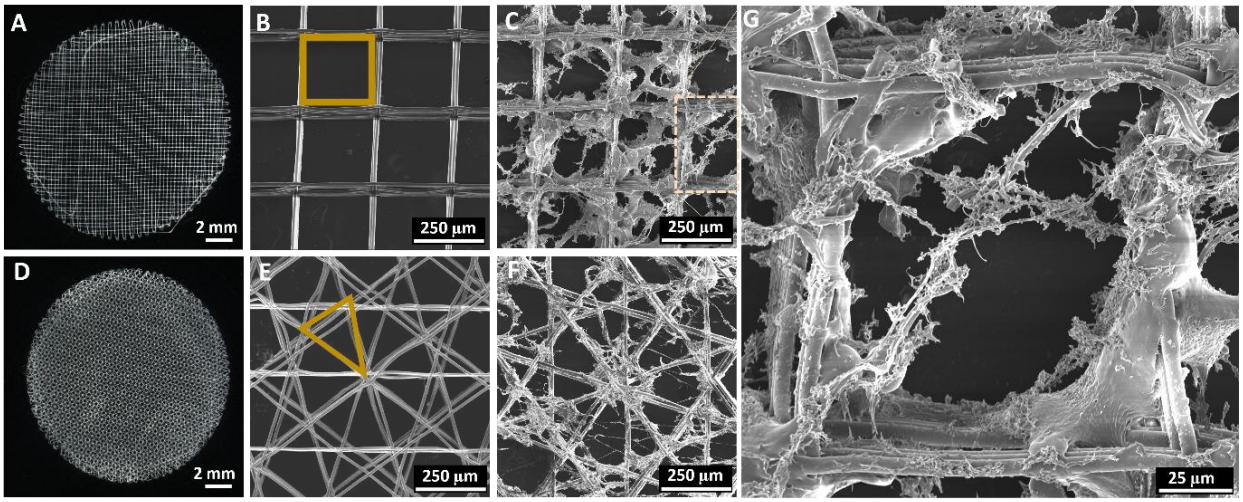

Figure 5.2. MEW scaffolds imaged with (A, D) optical microscopy and (B-C, E-G) scanning electron microscopy (SEM). A-B, D-E) non coated PCL scaffolds and C, F, G) pHEMA coated PCL scaffolds imaged with SEM. G) is a close up of C), as noted by a dashed yellow line. Scale bars: 2 mm (A, D), 250 µm (B-C, E-F), and 25 µm (G).

2.3. Scaffold coating and characterization

Bare PCL scaffolds were coated with phase separated pHEMA as shown in the schematic of **Figure 5.1** and in **Supporting Videos S5.1** and **S5.2**. The washing step changes the droplet morphology and surface area of the original PCL scaffolds. The droplet size that results from polymerizing in 80 wt.% water is larger than in mixtures with higher proportion of water[26]. There is also a phase separation threshold at 75 wt.%, below which the desired droplet formation is not achieved due to gelation preceding phase separation.

2.3.1. Morphology of pHEMA coated scaffolds

SEM was used to visualize the morphology of non-coated PCL scaffolds and pHEMA coated PCL scaffolds, as shown in **Figure 5.2 B&E** and **C&F**, respectively. The phase separated

pHEMA readily coated the MEW scaffold and presented a webbing morphology at the intersection of fibers and along the aligned PCL fibers. There was also bridging of the PCL pores observed where the pHEMA drops connect into spindle-like morphologies that span between fibers. The pHEMA bridges the pore voids by 32 ± 3% and 24 ± 4% of the pore areas for the square and triangle scaffolds respectively, creating a significantly greater surface area for cell attachment than the open pore voids ($p<1x10^{-6}$, n=5) (see section 4.6.2.). The porous microstructure of this synthetic pHEMA hydrogel resembles that of a micropore filling collagen matrix, formed around braided poly(lactic-*co*-glycolic acid) yarns as previously described[41]. Due to the important role that native collagen plays in tissue ultrastructure, forming such highly porous, high surface area scaffold with fibrillar morphologies is especially pertinent for biomedical materials[42].

2.4. Functionalization of pHEMA coated PCL scaffolds with RGD peptide

The peptide sequence arginine-glycine-aspartic acid (RGD) is an integrin recognition motif found in multiple cell adhesive extracellular matrix (ECM) proteins. First identified in fibronectin almost 40 years ago as a minimal integrin binding motif[43], RGD is one of the most extensively studied cell adhesion peptides. This particular peptide has been used in a range of TE applications, including with pHEMA brushes for specific cell attachment[44]. Our peptide functionalization approach suggests that the phase separated pHEMA droplets that coat the MEW PCL scaffold can incorporate bioactive CG-RGD-SG peptide and direct specific cell attachment through a physicochemical reaction. When adding the peptide, a pH of 8 is used for promoting Michael-Type addition reactions between the cysteine and unreacted HEMA. This reacted compound is then incorporated into the monomer droplets through a physical interaction. Previous work describes using X-ray photoelectron spectroscopy (XPS) and matrix-assisted laser desorption/ionization (MALDI) to study protein adsorption onto the pHEMA surface[45]. We found that due to the nature

of crosslinking and dynamic washing protocol described, traditional polymer characterization techniques (such as MALDI, gel permeation chromatography (GPC) or, Time-of-Flight Secondary Ion Mass Spectrometry (ToF-SIMS)) were not compatible with our system. Alternatively, we opted to use Fourier transform infrared spectroscopy – attenuated total reflectance (FTIR–ATR) to identify the presence of primary and secondary amines on the RGD-functionalized pHEMA coated PCL scaffolds. Using FT-IR ATR on dehydrated samples (**Figure S5.2**), peaks corresponding to primary and secondary amines are present only in the peptide-functionalized pHEMA samples, demonstrating presence of peptide. However, the thioester bond, which would indicate Michael-Type addition, overlaps with the carbonyl group and is very prominent in both samples.

As a proof of concept to determine peptide conjugation, we designed a set of biological experiments where the ubiquitously known peptide sequence that promotes cell attachment – RGD – is used in combination with a robust fibroblast cell line (NIH3T3). As a control for peptide functionality, a scrambled peptide (RGE) (full sequence: CGG-RGE-SG) is used as previously reported[46].

2.4.1. Evaluation of metabolic activity

To determine how cells proliferate on the scaffold surface, a metabolic assay based on 3-(4,5-Dimethyl-2-thiazolyl)-2,5-diphenyl-2H-tetrazolium bromide (MTT) was performed.[47] Our results showed a dynamic growth of NIH3T3 cells along the three timepoints (24, 48 and 72 h) within each experimental group (**Figure S5.3**). The non-coated PCL scaffolds had excellent cell adhesion and proliferation, as it is known that non-specific protein adsorption drives such cell-material interactions[48].

As expected with surfaces that reduce non-specific protein adsorption, the pHEMA coated PCL scaffolds had limited cell metabolic activity compared to non-coated scaffolds. This is due to

the known reduction in non-specific protein adsorption for pHEMA[49]. In summary, even though pHEMA increases the surface area of the scaffolds, this hydrogel coating reduces protein adsorption and cells growing on the surface of pHEMA have a slower metabolic rate.

2.4.2. Evaluation of cell morphology

To evaluate cell morphology of cells grown on non-coated and pHEMA coated scaffolds, NIH3T3 cells were grown for 24, 48 or 72 h, stained for nuclei (4',6-diamidino-2-phenylindole (DAPI), shown in blue) and F-Actin filaments (Phalloidin, shown in red) and imaged using a confocal microscope. Representative confocal images of cells attached to scaffolds are shown in **Figure S5.3B&C** for square and triangle pores, respectively. We observed more cell attachment onto the non-coated scaffolds compared to the pHEMA coated PCL scaffolds, which correlates to our findings from cell metabolic activity assays. We also observed an increase in number of cells across the three timepoints, showing cell growth and correlation to cell health (**FigureS5.3A**).

2.4.3. Optimization of peptide concentration

The functionalization of the pHEMA coated scaffolds with RGD peptide was optimized. Specifically, different peptide concentrations were explored to identify surface functionalization that supports cell attachment and growth. Previous research using pHEMA-functionalized with RGD used a 5 pmol/cm^2 peptide concentration[44]. Given that our scaffolds are 14 mm in diameter, the surface area of our circular scaffolds is 1.54 cm^2. This would be an equivalent of 7.7 pmol/scaffold, rounded to 8 pmol/scaffold. 100-fold higher (i.e., 800 pmol/scaffold) was used as a comparison. After a washing step, 20,000 cells were seeded on each scaffold (cell density of 13,000 cells/cm^2). The cell metabolic activity of cells grown for 72 h on pHEMA coated scaffolds functionalized with 8 or 800 pmol/scaffold is shown in **Figure 5.3A**. No significant differences

were observed between the two concentrations, and the lower concentration of 8 pmol/scaffold was used herein.

2.4.3. Optimization of reaction time for peptide functionalization

The freshly made pHEMA/PCL was dipped into the RGD solution at various times for the functionalization of the coating. After the pHEMA coating step, samples were placed in water to remove excess HEMA monomer and immediately placed in the peptide solution at pH 8 for 30 min. The time interval in which samples were left in water before functionalization varied between 0 min (dip wash) and 60 min. We also included a group in which the scaffolds were left in water overnight (ON) before functionalization and, lastly, a group in which scaffolds were dip washed and immediately functionalized, but then stored in PBS ON before seeding cells. The results of this optimization are represented in **Figure 5.3B**. We observed a rapid drop-off in effective functionalization at even the shortest period (less than 1 min). Specifically, no differences were found between cell metabolic of cells seeded onto RGD-functionalized that were washed in water for 1 min, 10 mins, 20 min, 1 h, or ON. Interestingly, cells seeded onto scaffolds that were functionalized immediately after the wash step and then stored ON showed similar metabolic activity to those prepared fresh (pHEMA + wash + RGD functionalization + cell seeding). The non-significant differences between freshly prepared scaffolds and those left in PBS ON suggest that the RGD-functionalization is stable when left in PBS ON. Even with this suggested stability of functionalization, scaffolds were prepared fresh each time before cell seeding.

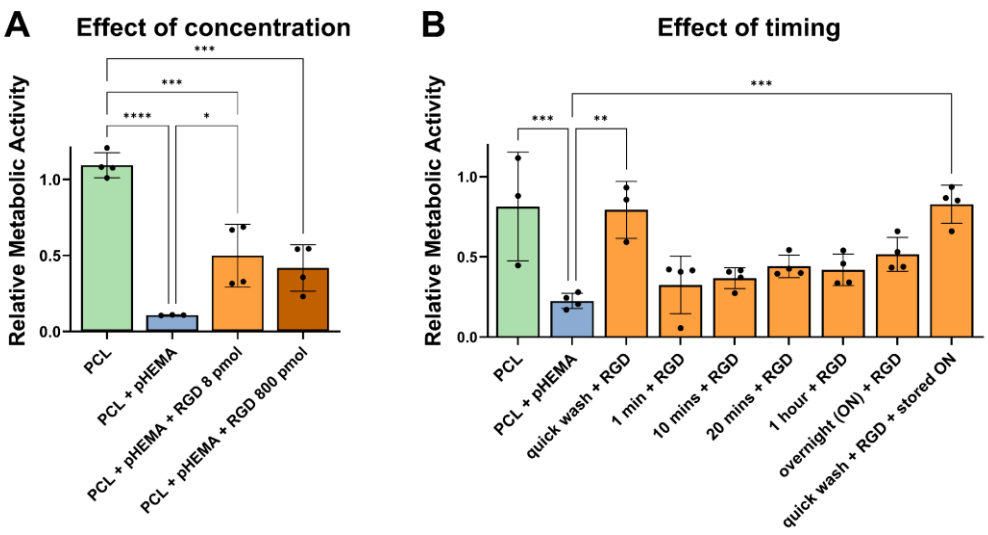

*Figure 5.3. Functionalizing pHEMA with RGD and comparing cell metabolic activity after 72 h in culture normalized to cells seeded directly into well. A) optimization of peptide concentration (8 pmol or 800 pmol per scaffold) and B) optimization of time window for peptide functionalization onto pHEMA coating (0, 1, 10, 20 or 50 min, overnight (ON+RGD) or functionalized after 0 min and left overnight at room temperature (RGD+ON). Results show that relative cell metabolic activity is similar for both concentrations of peptide used (8 pmol or 800 pmol RGD per scaffold). The ideal timing for RGD functionalization is an immediate wash step (0 min). Once freshly prepared pHEMA scaffolds are placed into water before functionalization for as little as 1 min, relative metabolic activity shows a notable decrease. Relative cell metabolic activity levels are consistent regardless of time in water (1, 10, 20, or 50 min or overnight (ON+RGD)). Further, relative cell metabolic activity levels are similar for cells seeded on RGD-functionalized scaffolds with quick wash step (0 min) immediately after functionalization or RGD-functionalized scaffolds left in PBS overnight and then seeded with cells (RGD+ON). Data represents mean and standard deviation for n=4 (*p<0.05, **p<0.01, ***p<0.001, ****p<0.0001) using one-way ANOVA and post hoc Tukey test.*

2.4.4. Evaluation of metabolic activity of functionalized scaffolds

After optimizing the peptide concentration and procedure timing for functionalization of pHEMA coated PCL scaffolds with RGD, we further studied cell metabolic activity over time. We measured metabolic activity of cells grown on non-coated PCL scaffolds, pHEMA coated PCL scaffolds, pHEMA coated PCL scaffolds functionalized with RGD, and pHEMA coated PCL scaffolds functionalized with scrambled peptide (RGE) (full sequence: CGG-RGE-SG) for 24, 48, or 72 h. Previous studies have used RGE sequence as a control for RGD[50]. Results shown in **Figure 5.4A** demonstrate that cells seeded onto RGD-functionalized pHEMA coated scaffolds showed increased cell metabolic activity compared to scrambled-functionalized pHEMA or non-functionalized scaffolds starting at 48 h. This trend becomes more evident for the 72 h timepoint. Therefore, the cells respond differently depending on the peptide sequence added to the pHEMA coating. This suggests tailorability to different peptide sequences, and we hypothesize that this process may be extrapolated to other pairs of peptide sequences and cell types.

2.4.5. Evaluation of cell morphology of functionalized scaffolds

To complement data of cell metabolic activity, studies were conducted to evaluate cell morphology. **Figure 5.4B** shows confocal images of cells grown on non-coated PCL scaffolds, pHEMA coated PCL scaffolds, and pHEMA coated PCL scaffolds functionalized with RGD or scrambled peptide for 24, 48 and 72 h. Our results support our findings from cell metabolic activity studies: we observed limited cell attachment and cell elongation on pHEMA coated scaffolds compared to non-coated PCL scaffolds. Peptide-functionalized pHEMA coated scaffolds show improved cell elongation along scaffold morphology compared to non-functionalized or scrambled-functionalized scaffolds. Overall, we observed improved cell attachment and metabolic activity on peptide-functionalized scaffolds. Further, by demonstrating that when using a

scrambled peptide, cells revert to limited cell attachment, we hypothesize this system will allow for tailorable cell attachment by addition of different peptide sequences.

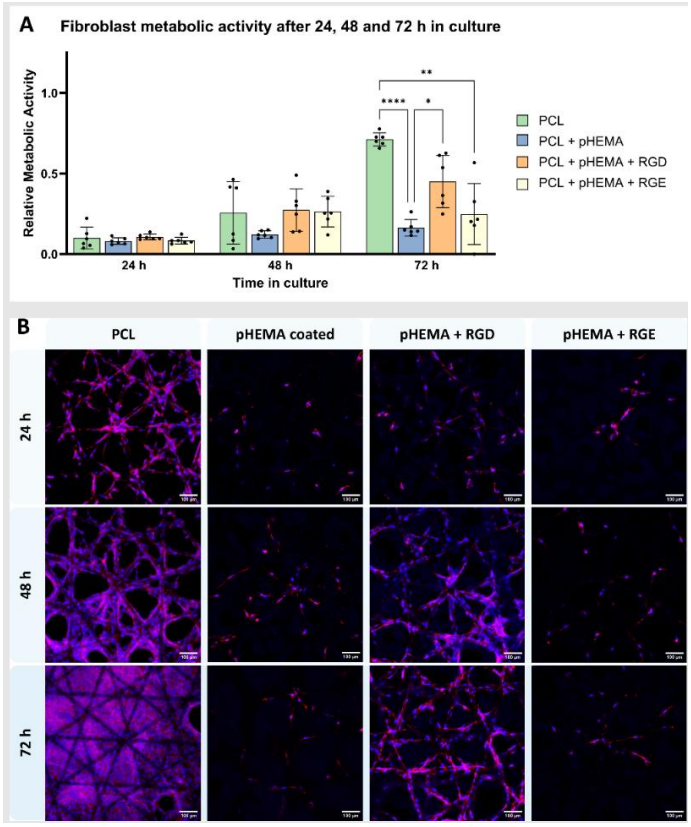

*Figure 5.4. Validation of peptide functionalization of pHEMA coated PCL scaffolds. A) relative metabolic activity comparing non-coated, pHEMA coated, RGD- and scrambled-functionalized (RGE) pHEMA coated PCL scaffolds for 24, 48 and 72 h. Data was normalized to cells seeded directly into well grown for 72 h and represents mean and standard deviation for n=6 (*p<0.05, **p<0.01, ****p<0.0001) using one-way ANOVA and post hoc Tukey test for each timepoint. B) confocal images of cells grown for 24, 48 or 72 h on left to right: PCL scaffold, pHEMA coated, RGD-functionalized pHEMA, and scrambled-functionalized pHEMA. NIH3T3 cells were stained for actin filaments with Alexa Fluor™ 594 Phalloidin (shown in red) and nuclei with DAPI (shown in blue). Scale bars: 100 µm.*

3. Conclusion

The current study demonstrates the successful coating of PCL MEW scaffolds with phase-separated pHEMA and subsequent functionalization with cell-adhesive peptides. This methodology leverages the unique phase separation properties of pHEMA to create a hydrogel coating with enhanced surface area and structural properties conducive to cell attachment and growth. The peptide-functionalized scaffolds, specifically those with the RGD peptide, significantly improved cell metabolic activity and attachment compared to non-functionalized and scrambled peptide controls. These findings suggest that the combination of MEW scaffolds and biofunctionalized hydrogels can be tailored to specific biomedical applications, offering a versatile platform for tissue engineering and regenerative medicine. Future work may explore the application of different peptide sequences and cell types to further optimize and expand the utility of this scaffold system.

4. Experimental Section/Methods

4.1. Scaffold design

Scaffolds used for this study were printed using a custom MATLAB code. The two scaffold designs used in this study were 1) square and 2) triangular pores. The square pores were used to visualize the stringing and coating effect of the pHEMA. The uniform square pores proved to be ideal for visualizing the pHEMA coating. Alternatively, triangular pores were used to investigate the coating on a more application-relevant scaffold (cell culture analysis) because they more closely resemble native tissue by having smaller average pore sizes, and randomized pore shapes and sizes. All scaffolds were designed to have a 14 mm diameter to fit in a standard 24 well plate and did not have typical turning loops on the scaffold edges to maximize the useful scaffold area.

The square pore scaffold is a basic test print with 0°/ 90° directions to give 10 layers in each direction for a total of 20 layers. The triangle-pore scaffold contains five directions at 36° increments (0°, 36°, 72°, 108°, 144°) to give layers in each direction for a total of 20 layers. Both scaffolds were designed with similar features to isolate the change in fiber placement between samples: 11 μm fiber diameter, 250 μm fiber to fiber distance, and 20 total layers.

4.2. MEW process and printing parameters

Scaffolds were printed on a custom-built MEW device as previously described.[37] Medical grade PCL (Corbion PC12) was heated to 75 °C and extruded by 0.3 bar pressure from a 22 G nozzle onto a glass slide resting on a metal substrate. Voltage difference of 5.5 kV (grounded nozzle and positive potential at the collector) was applied over the 3 mm gap between the nozzle and the glass slide. Printing speed was fixed at 500 mm/min, well above the jet speed measured as a critical translation speed (CTS), effectively stretching the fibers to have smooth surface. To ensure accurate fiber placement at the edge of the scaffold, 0.3s pauses were introduced to minimize the jet lag after long moves.

4.3. Characterization of non-coated MEW scaffolds

Fiber spacing and diameters were measured using a light microscope (VHX-7000 Digital Microscope, Keyence, Japan).

4.4. Preparation for cell culture of non-coated MEW scaffolds

PCL scaffolds were chemically etched with 0.1 M sodium hydroxide (NaOH) for 30 min. For cell culture analysis, PCL scaffolds were sterilized with 70% ethanol and subsequently etched with sterile filtered 0.1 M NaOH for 30 min. Scaffolds were rinsed with PBS three times and left to sit in media overnight before use.

4.5. PHEMA phase separation and coating of PCL scaffolds

PHEMA hydrogels were made on demand for the scaffold coating. HEMA with 99% purity was purchased from Sigma Aldrich, USA. The pHEMA hydrogels were formed using a redox initiator combination of APS and TEMED. All reagents were filtered with a 0.22 µm pore size filter (ThermoFisher, USA) to achieve sterility. Coating procedures were performed in a sterile environment. Briefly, an 80:20 (wt.%) dH_2O:HEMA solution was made. This concentration was chosen since it results in phase separation before polymerization. To this solution, 2 wt.% by monomer APS was added to the solution followed by 0.2 wt.% by monomer TEMED was added. The reaction took place undisturbed while waiting for phase separation to begin, or when the solution began to turn opaque. A scaffold was placed in the solution 30 sec post phase separation and allowed to sit on the bench top for 80 sec. The scaffold was then retrieved from the solution and placed in dH_2O to remove any excess HEMA. Alternatively, for peptide functionalization, pHEMA coated scaffolds were quickly washed in dH_2O and then placed directly in peptide solution to take advantage of the growing polymer chains. Performing this step immediately also carries the intention of transferring and trapping some peptide in the monomer droplet through a physicochemical reaction. Scaffolds were used *in vitro* promptly after coating and functionalization.

4.5.1. Phase separation timing

PHEMA monomer solution is clear and turns opaque once polymerization occurs. Smaller reaction volumes were used to fit a 96 well plate. The absorbance was measured at 350 nm over time using SpectraMax iD3 (Molecular Devices, USA). Experiments were performed in parallel and in triplicate. (See **Figure S5.1**).

4.6. Characterization of pHEMA coated scaffolds

4.6.1. SEM for morphology

The morphology of the coating was visualized using SEM. Scaffolds coated with pHEMA were prepared using both a freeze-drying process as well as airdrying. For freeze-drying, coated scaffolds were hung on binder clips and suspended on a 3D printed rig before being placed in the freezer at –20 °C. The scaffolds were dried using a vacuum pump lyophilizer overnight. Samples were coated with 5 nm of platinum before imaging using the Everhart–Thornley detector (ETD) of the SEM (ThermoFisher Apreo 2, USA).

4.6.2. Estimated porosity and pore filling of pHEMA coated scaffolds compared to non-coated scaffolds

Scaffold porosity was estimated by approximating the MEW fibers as cylinders with diameter equal to that measured in section 4.3 and totaling the volume of fibers within a unit scaffold volume based on the programmed square or triangle scaffold architectures. Since this approximation does not account for differences in scaffold height, both square and triangle design were programmed to have the same number of layers to mitigate porosity differences between scaffold designs. The proportion of pHEMA coating filling the MEW scaffold voids was also estimated by analyzing the morphology of the coating in SEM micrographs (section 4.6.1). A binary mask was applied to a 4x4 pore region of interest to segment MEW fibers and pHEMA structures from the background and compare pore coverage to the non-coated controls (ImageJ version 1.53t Java 1.8.0_322 (64-bit)).

4.7. Biofunctionalization of pHEMA

4.7.1. Peptide synthesis

The peptides RGD (CG-RGD-SG) and RGE (CGG-RGE-SG) were produced using solid-phase peptide synthesis (Liberty 2.0 - CEM, USA) on FMOC-Gly-Wang resin at 0.1 mmol scale (CEM, USA). Peptides were cleaved using 4 mL cocktail consisting of 0.5 mL triisopropylsilane, 0.5 mL ddH_2O, 0.5 mL 3,6 dioxa-1,8-octane dithiol, and 18.5 mL trifluoracetic acid for 30 min at 40ºC (CEM Razor - CEM, USA). Cleaved peptides were precipitated and washed three times in 100% diethyl ether, and vacuum-dried overnight. The purification was made using XBridge® Peptide C18 column (19 mm x 150 mm, 5 µm particle size, 130Å pore size, 1/pKg from Waters Co, USA) and a variation in the concentration of acetonitrile from 3% - 7% in water (both solvents with 0.1% Trifluoroacetic acid – TFA) using peptide purification system Prodigy (CEM, USA). High throughput analysis was performed via Matrix Assisted Laser Desorption/Ionization (MALDI) protocol was performed (Bruker, Germany) before and after purification (**Figure S5.4A-B, D-E**). The standards used covered mass range ~1000-3200 Da - Bruker) using α-Cyano-4-hydroxycinnamic acid as a matrix (Sigma Aldrich, USA). The purification was validated using high-performance liquid chromatography (HPLC) (**Figure S5.4C&F**), and it is considered pure for this study when it is greater than 95% purity. The HPLC test was set up to 20 µL injection volume, and it was conducted using a mobile gradient phase consisting of 93% acetonitrile + 0.05% TFA and 7% water + 0.05% TFA in a Kromasil C18 column (50 mm x 4.6 mm, 5 µm particle size, 100 Å pore size from Supelco, Bellefonte, PA) with a flow rate of 0.5 mL/min over 22 min. The column effluent was monitored with a variable wavelength UV−vis detector at 214 nm (Shimadzu Technologies, Japan). Peptides were freeze-dried using FreeZone 4.5 Liter -84 °C

Benchtop Freeze Dryers (Labconco Co, USA) and stored at -80 °C until use. Stock solutions of peptides were stored at -80 °C until use.

4.7.2. Peptide functionalization

Scaffolds coated with pHEMA were functionalized via a dip coating method. After coating with phase-separated pHEMA, the scaffolds were dipped in dH_2O at RT to wash some excess monomer and immediately dipped in peptide solution at pH 8 at RT using triethanolamine buffer (TEA) (Sigma Aldrich, USA). Scaffolds were submerged in the peptide solution (8 or 800 pmol) for 30 min at RT, and then washed in PBS before use.

4.7.3. ATR FT-IR for analysis of peptide functionalization

Attenuated total reflectance (ATR) Fourier transform infrared spectroscopy (FT-IR) was used to compare the profiles of non-functionalized and RGD-functionalized pHEMA scaffolds. Samples were prepared and freeze dried as previously described. Data was collected on Nicolet 6700 FT-IR (ATR) (ThermoFisher Scientific, USA). (See **Figure S5.2**).

4.8. Cell culture

Fibroblast cell line NIH-3T3 was purchased from ATCC. Cells were cultured in Dulbecco's Modified Eagle Medium (DMEM) (Gibco, USA) supplemented with 1x Non-Essential Amino Acids (NEAA) (Gibco), 5% Fetal Bovine Serum (FBS) (Gibco), and Penicillin-Streptomycin (Pen/Strep) (Sigma Aldrich, USA), and maintained at 37 °C at 5% CO_2 in a sterile Heracell VIOS CO_2 Incubator (ThermoFisher Scientific). Cells were passaged when 70% confluency was reached (every 2-3 days). For passaging, media was removed, and a gentle wash with sterile warm 1x PBS was performed before adding Trypsin 0.25% (Gibco) and incubating until cells detached (approx. 5 min) at 37 °C at 5% CO_2. Trypsin was inoculated with complete fresh media and centrifuged for 5 min at 3000 rpm (Centrifuge 5702 RH Eppendorf, USA). Supernatant was removed and cells

were resuspended in fresh media at 1 million cells/mL. Cells were seeded into a new T-flask (Gibco) or used for experiments.

4.9. Cell seeding

All scaffolds were prepared under sterile conditions as stated above. All PCL scaffolds were pretreated (etched) with 0.1 M NaOH solution for 30 min. PCL scaffolds were coated with phase separated pHEMA, and then further functionalized with RGD or scrambled peptide. Scaffolds were placed on a custom-designed platform and cells were seeded onto the scaffolds. This elevated platform prevents direct contact with the well plate, promoting cell attachment onto the scaffolds. Each scaffold was seeded with 20,000 cells in 20 μL of culture media in a droplet placed in the center of the scaffold. Scaffolds were incubated for 3 h at 37 °C. After, the scaffolds were removed from their elevated platform, placed in the bottom of a new well, and 1 mL of complete media was added. Cells were cultured for 24, 48, or 72 h before analysis.

4.10. Cell metabolic activity

Cell metabolic activity was measured using 3-(4,5-Dimethyl-2-thiazolyl)-2,5-diphenyl-2H-tetrazolium bromide (MTT). MTT (Sigma Aldrich) was mixed with PBS to create a stock solution of 5 mg/mL and filtered with a 0.22 μm pore filter to achieve sterility. To conduct the MTT assay, two different procedures were conducted depending on if the analysis was conducted on a well with just cells or a well with a scaffold. For wells with only cells, 200 μL of the MTT stock solution was added to each well. To wells with a scaffold, a working solution of 1 mg/mL was created by combining 1 mL of media with 200 μL of MTT stock solution for every scaffold. The scaffolds were moved to a new well with 1.2 mL of working solution. All samples were incubated for 3 h at 37 °C and 5% CO_2.

After this time, the formed formazan crystals were dissolved in 330 µL IPA. For wells containing scaffolds, 330 µL IPA were placed into a microcentrifuge tube to which the scaffold was added. For wells without scaffolds, the existing media was aspirated, and the wells were washed with the same volume of IPA. Samples were then centrifuged at 10,000 rpm for 3 min to separate the cells/cell debris from the solution. 100 µL of each sample solution pipetted in duplicate into a 96 well plate. The absorbance was taken at 570 nm using a plate reader (Molecular Devices, USA). Data was normalized to cells seeded directly onto well plate and cultured for 72 h.

4.11. Cell Fixation

Cells were fixed using a 4% solution of paraformaldehyde (PFA) (Electron Microscopy Sciences, USA). After a PBS wash, each sample was placed in 200 µL of PFA for 20 min at RT. Samples were washed and stored in PBS at 4 °C until staining.

4.12. Cell staining and imaging

Cells were stained with phalloidin (actin filaments) using Phalloidin (Alexa Fluor™ 594 Phalloidin, Invitrogen) at 1:400 dilution, and (4',6-diamidino-2-phenylindole) DAPI (nuclei) using DAPI (ThermoFisher Scientific) at 1:100 dilution. Fixed cells were permeabilized with a 0.1% working solution of Triton X-100 for 15 min and washed twice with PBS. To each sample, 200 µL of phalloidin working solution was added for 30 min. 200 µL of DAPI was added for 5 min. The samples were then washed twice with PBS and stored at 4 °C protected from light. Samples were imaged using a Zeiss confocal SP3 microscope with objective Plan-Apochromat 10x/0.45 M27 and ZEN Black Version 2.1. to visualize actin filaments (Em.: 585 nm and Ex.: 733 nm) with laser power 6.0% and nuclei (Em.: 410 nm and Ex.: 507 nm) with laser power 4.0%. Images shown are a compressed z-stack ranging from 152-220 µm thickness with images acquired every 2 µm. Different channels were condensed into a single image using Fiji ImageJ version 1.53t Java

1.8.0_322 (64-bit), (ImageJ, USA). For long term storage, a few drops of antifade mounting media (ProLong, Invitrogen) were added and samples were stored at 4 °C protected from light.

4.13. Statistical Analysis

MTT data was processed using GraphPad Prism version 10.2.2. Data was normalized to cells seeded directly into well grown for 72 h and represents mean and standard deviation for n=4 for RGD concentration and timing and n=6 for validation of peptide functionalization. Data was screened for outliers using GraphPad Prism and the outliers were removed. All data sets showed a normal distribution through Shapiro-Wilk test. In all cases, one-way ANOVA was performed with 95% confidence and post-hoc Tukey's test with p= *<0.05, **<0.005, ***<0.0005, and ****<0.0001.

4.14. Videography and video editing

Supporting Video S5.1 was captured using a SONY SteadyShot α7III camera and lenses SONY FE4/24-105 G OSS (Sony, Japan) and Canon macro lens EF 180 mm 1:1.5 ultrasonic adapted with Fotodiox Pro EF-Sny (E) Fusion (Canon, Japan). **Supporting Video S5.1** was captured using a digital microscope (Andonstar AD210, Andonstar Tech Co., China). Videos were edited using Microsoft Clipchamp v.2023 (Microsoft 365, Windows, USA) and Adobe Premiere Rush v2.10.0 (Adobe, USA).

Acknowledgements

This project was funded by the Wu Tsai Human Performance Alliance and the Joe and Clara Tsai Foundation while A. K. appreciates the funding from Knight Campus Undergraduate Research Program. P.D. is supported by the Bradshaw and Holzapfel Research Professor in Transformational Science and Mathematics. N.P. acknowledges funding support from the Knight Campus-

PeaceHealth Postdoctoral Fellowship Program and Advance Queensland Industry Research Fellowship (AQIRF2020). The technical assistance of Kelly Leguineche and Dr. Genevieve Romanowicz is greatly appreciated. K. L. O. appreciates the insight from Jacqui Beran and Dr. Stephen Golledge at Center for Advanced Materials Characterization in Oregon (CAMCOR).

References

[1] K. L. O'Neill, P. D. Dalton, *Small Methods* **2023**, **7**, 2201589.

[2] J. C. Kade, P. D. Dalton, *Adv. Healthcare Mater.* **2020**, 202001232.

[3] D. G. Castner, B. D. Ratner, *Surface Science* **2002**, 500, 28.

[4] L. Y. Liu, S. F. Chen, C. M. Giachelli, B. D. Ratner, S. Y. Jiang, *Journal of Biomedical Materials Research Part A* **2005**, 74A, 23.

[5] B. D. Ratner, *Journal of Controlled Release* **2002**, 78, 211.

[6] A. R. Jahangir, W. G. McClung, R. M. Cornelius, C. B. McCloskey, J. L. Brash, J. P. Santerre, *J Biomed Mater Res* **2002**, 60, 135.

[7] J. Visser, F. P. W. Melchels, J. E. Jeon, E. M. van Bussel, L. S. Kimpton, H. M. Byrne, W. J. A. Dhert, P. D. Dalton, D. W. Hutmacher, J. Malda, *Nature Communications* **2015**, 6, 6933.

[8] O. Bas, E. M. De-Juan-Pardo, M. P. Chhaya, F. M. Wunner, J. E. Jeon, T. J. Klein, D. W. Hutmacher, *European Polymer Journal* **2015**, 72, 451.

[9] D. Janzen, E. Bakirci, A. Wieland, C. Martin, P. D. Dalton, C. Villmann, *Adv Healthc Mater* **2020**, 9, e1901630.

[10] N. T. Saidy, A. Fernández-Colino, B. S. Heidari, R. Kent, M. Vernon, O. Bas, S. Mulderrig, A. Lubig, J. C. Rodríguez-Cabello, B. Doyle, D. W. Hutmacher, E. M. De-Juan-Pardo, P. Mela, *Advanced Functional Materials* **2022**, 32, 2110716.

[11] D. Janzen, E. Bakirci, J. Faber, M. Andrade Mier, J. Hauptstein, A. Pal, L. Forster, J. Hazur, A. R. Boccaccini, R. Detsch, J. Tessmar, S. Budday, T. Blunk, P. D. Dalton, C. Villmann, *Adv Healthc Mater* **2022**, 11, e2201826.

[12] A. Kriebel, M. Rumman, M. Scheld, D. Hodde, G. Brook, J. Mey, *Journal of Biomedical Materials Research Part B-Applied Biomaterials* **2014**, 102, 356.

[13] P. Achenbach, I. Hambeukers, A. L. Pierling, J. L. Gerardo-Nava, L. Hillerbrand, A. S. Sechi, K. J. Glucks, P. D. Dalton, A. Pich, A. Dievernich, H. Altinova, G. A. Brook, *J Neurosci Methods* **2021**, 361, 109289.

[14] Y. Wang, W. Zhang, C. Gong, B. Liu, Y. Li, L. Wang, Z. Su, G. Wei, *Soft Matter* **2020**, 16, 10029.

[15] S. Bertlein, G. Hochleitner, M. Schmitz, J. Tessmar, M. Raghunath, P. D. Dalton, J. Groll, *Adv Healthc Mater* **2019**, 8, e1801544.

[16] O. Wichterle, D. LÍM, *Nature* **1960**, 185, 117.

[17] A. W. Lloyd, R. G. A. Faragher, S. P. Denyer, *Biomaterials* **2001**, 22, 769.

[18] I. Tranoudis, N. Efron, *Cont Lens Anterior Eye* **2004**, 27, 193.

[19] A. Mandal, J. R. Clegg, A. C. Anselmo, S. Mitragotri, *Bioeng Transl Med* **2020**, 5, e10158.

[20] C. Hicks, G. Crawford, T. Chirila, S. Wiffen, S. Vijayasekaran, X. Lou, J. Fitton, M. Maley, A. Clayton, P. Dalton, S. Platten, B. Ziegelaar, Y. Hong, A. Russo, I. Constable, *Progress in Retinal and Eye Research* **2000**, 19, 149.

[21] C. R. Hicks, T. V. Chirila, A. B. Clayton, J. H. Fitton, S. Vijayasekaran, P. D. Dalton, X. Lou, S. Platten, B. Ziegelaar, Y. Hong, G. J. Crawford, I. J. Constable, *British Journal of Ophthalmology* **1998**, 82, 18.

[22] M. Zare, A. Bigham, M. Zare, H. Luo, E. Rezvani Ghomi, S. Ramakrishna, *Int J Mol Sci* **2021**, 22.

[23] Y. S. Casadio, D. H. Brown, T. V. Chirila, H.-B. Kraatz, M. V. Baker, *Biomacromolecules* **2010**, 11, 2949.

[24] M. Pradny, M. Slouf, L. Martinova, J. Michalek, *E-Polymers* **2010**, DOI: 043.

[25] K. Dušek, B. Sedláček, *European Polymer Journal* **1971**, 7, 1275.

[26] T. V. Chirila, I. J. Constable, G. J. Crawford, S. Vijayasekaran, D. E. Thompson, Y.-C. Chen, W. A. Fletcher, B. J. Griffin, *Biomaterials* **1993**, 14, 26.

[27] C. R. Hicks, T. V. Chirila, P. D. Dalton, A. B. Clayton, S. Vijayasekaran, G. J. Crawford, I. J. Constable, *Australian and New Zealand Journal of Ophthalmology* **1996**, 24, 297.

[28] J. S. Calnan, J. J. Pflug, A. S. Chhabra, N. Raghupati, *British Journal of Plastic Surgery* **1971**, 24, 113.

[29] X. Lou, S. Munro, S. Wang, *Biomaterials* **2004**, 25, 5071.

[30] M. Paljevac, K. Jeřabek, P. Krajnc, *Journal of Polymers and the Environment* **2012**, 20, 1095.

[31] J. Majer, M. Paljevac, E. Žagar, S. Kovačič, P. Krajnc, *Reactive and Functional Polymers* **2016**, 109, 99.

[32] E. A. Kamoun, A. El-Betany, H. Menzel, X. Chen, *Int J Biol Macromol* **2018**, 120, 1884.

[33] S.-h. Kim, C.-C. Chu, *Journal of Biomedical Materials Research* **2000**, 53, 258.

[34] S. G. Levesque, R. M. Lim, M. S. Shoichet, *Biomaterials* **2005**, 26, 7436.

[35] M. Ziminska, J. J. Wilson, E. McErlean, N. Dunne, H. O. McCarthy, *Materials* **2020**, 13, 2530.

[36] S. Atzet, S. Curtin, P. Trinh, S. Bryant, B. Ratner, *Biomacromolecules* **2008**, 9, 3370.

[37] I. Liashenko, A. Hrynevich, P. D. Dalton, *Adv. Mater.* **2020**, 32.

[38] T. M. Robinson, D. W. Hutmacher, P. D. Dalton, *Advanced Functional Materials* **2019**, 29, 1904664.

[39] J. Kim, E. Bakirci, K. L. O'Neill, A. Hrynevich, P. D. Dalton, *Macromolecular Materials and Engineering* **2021**, 306, 2000685.

[40] A. Youssef, A. Hrynevich, L. Fladeland, A. Balles, J. Groll, P. D. Dalton, S. Zabler, *Tissue Engineering Part C: Methods* **2019**, 25, 367.

[41] G. P. Chen, T. Sato, H. Ohgushi, T. Ushida, T. Tateishi, J. Tanaka, *Biomaterials* **2005**, 26, 2559.

[42] M. Vranceanu, R. Şaban, I. Antoniac, M. Albu, F. Miculescu, *UPB Scientific Bulletin, Series B: Chemistry and Materials Science* **2012**, 74, 145.

[43] E. Pierschbacher Md Fau - Ruoslahti, E. Ruoslahti.

[44] S. Tugulu, P. Silacci, N. Stergiopulos, H. A. Klok, *Biomaterials* **2007**, 28, 2536.

[45] S. L. McArthur, K. M. McLean, H. A. W. St. John, H. J. Griesser, *Biomaterials* **2001**, 22, 3295.

[46] D. Grafahrend, K. H. Heffels, M. V. Beer, P. Gasteier, M. Moller, G. Boehm, P. D. Dalton, J. Groll, *Nat Mater* **2011**, 10, 67.

[47] R. Podgorski, M. Wojasinski, T. Ciach, *Sci Rep* **2022**, 12, 9047.

[48] C. J. Wilson, R. E. Clegg, D. I. Leavesley, M. J. Pearcy, *Tissue Engineering* **2005**, 11, 1.

[49] J. Deng, T. Ren, J. Zhu, Z. Mao, C. Gao, *Regenerative Biomaterials* **2014**, 1, 17.

[50] D. Grafahrend, K. H. Heffels, M. V. Beer, P. Gasteier, M. Moller, G. Boehm, P. D. Dalton, J. Groll, *Nature materials* **2011**, 10, 67.

CHAPTER 6: AUTOMATED SEAMLESS POLY(E-CAPROLACTONE) ELECTROSPUN TUBES FOR CRITICALLY-SIZED BONE DEFECT REPAIR

O'Neill KL, Williams KE, Hajarizadeh A, Rauff A, Liashenko I, Guldberg RE, Dalton PD Automated Seamless Poly(ε-caprolactone) Electrospun Tubes for Critically-Sized Bone Defect Repair. *Submitted to Tissue Engineering Part C: Methods* (Dec 2025).

This chapter presents an automated manufacturing framework for the scalable production of electrospun polymer scaffolds designed for critical defect repair in rate femoral defect model. By integrating SES with automated solder-based perforation, the study introduces a streamlined and reproducible workflow for fabricating seamless tubular PCL meshes. The approach eliminates manual assembly steps, improves structural consistency, and preserves mechanical performance while significantly reducing fabrication time and material waste. Beyond its immediate application to bone TE, this work contributes to the broader field of TE.

Scientific Contribution and Advancement of Knowledge

This work advances the scientific understanding of how automated fabrication processes influence scaffold reproducibility, mechanical performance, and biological function. PCL tubular meshes were fabricated using SES, followed by a subtractive manufacturing step using the stage of a custom-bult MEW system to control the positioning of a portable soldering iron. The development of this seamless, tubular PCL mesh demonstrates how automation can overcome limitations inherent to manually assembled electrospun scaffolds, such as variability in thickness, bonding strength, and geometric uniformity. The integration of a programmed soldering system for perforation enables precise, repeatable pore formation while maintaining structural integrity, representing a critical step toward scalable scaffold production. The resulting constructs show

consistent fiber morphology and mechanical resilience comparable to traditional hand-assembled designs, validating that enhanced efficiency does not compromise functional performance. This chapter contributes to the linking of fabrication control and biological outcome, providing quantitative evidence that uniform scaffold architecture supports bone formation *in vivo*.

Broader Implications and Future Directions

The broader implications of this chapter extend to the fields of biofabrication, materials engineering, and regenerative medicine. It illustrates how automation and hybrid manufacturing can be integrated into scaffold design pipelines to achieve precision and scalability across tissue types. The methodology can be adapted to other thermoplastic biomaterials. Future directions include coupling automated perforation with MEW-based architectures for tunable reinforcement. Collectively, these advances contribute to the overarching vision of this thesis: to establish reliable, high-resolution fabrication platforms that enable reproducible solutions for TE applications.

Automated Seamless Poly(ε-caprolactone) Electrospun Tubes for Critically-Sized Bone Defect Repair

Kelly L. O'Neill, Kylie E. Williams, Auveen Hajarizadeh, Adam Rauff, Ievgenii Liashenko, Robert E. Guldberg, Paul D. Dalton**

**Equal contribution*

Phil and Penny Knight Campus for Accelerating Scientific Impact

University of Oregon

1505 Franklin Boulevard, 97403-6231, Eugene, OR, USA

Corresponding authors: Paul D. Dalton pdalton@uoregon.edu; Robert E. Guldberg guldberg@uoregon.edu

Keywords: bone tissue engineering, solution electrospinning, biofabrication

Abstract for "Automated Seamless Poly(ε-caprolactone) Electrospun Tubes for Critically-Sized Bone Defect Repair"

In this study, we demonstrate an automated approach to efficiently and reproducibly manufacture perforated poly(ε-caprolactone) (PCL) solution electrospun tubular meshes designed for critically-sized bone defect repair. The workflow improves reproducibility and reduces fabrication time by 67% (8.7 versus 2.7 h per 10 meshes). By directly electrospinning PCL onto a rotating cylindrical mandrel, seam-related discontinuities are eliminated, and subsequent use of an automated soldering iron system enables precise 1 mm perforations that promote vascular ingrowth during bone healing. Despite the decrease in mass of the new design compared to the original design (18.24±1.5 mg for old versus 11.48±1.2 mg for new design), mechanical testing revealed similar resistance to lateral compression compared to semi-manually assembled meshes. This is important to prevent collapse during surgical placement and injection of osteoinductive treatments. Further, eliminating surgical glue improves the manufacturing simplicity and scaffold reproducibility. Following implantation with bone morphogenic protein-2 loaded alginate, the new design performed similarly to the original: *in vivo* micro-computed tomography confirmed bone formation that significantly increased ($p \leq 0.05$) over 8-weeks in an established rat femoral defect model. This study provides a novel production method of tubular scaffolds with variable dimensions and flexible perforation patterns and demonstrates improvements in fabrication efficiency and reproducibility.

1. Introduction

Large bone defects present a challenge to orthopedic medicine. Overcoming these challenges is crucial since the skeleton provides structural support that facilitates human posture and locomotion, contributes to systemic mineral and nutrient storage, and enables blood and immune cell production [1]. The current gold standard for treatment is autologous grafting, which is often constrained by complications such as donor site morbidity and limited graft availability [2, 3]. Alternatively, allogenic grafts, while relieving the injured patient from bone harvest, pose the risk of immune rejection [4]. To address these challenges, tissue engineering (TE) strategies combining polymeric scaffolds and meshes with bioactive molecules have been designed to enhance bone repair [5-7].

Many fabrication methods have been proposed for polymeric scaffold formation towards bone regeneration [8, 9]. One fabrication method commonly used to produce polymer meshes is solution electrospinning (SES). For TE applications, the resulting non-woven ultra-fine fibers are intended to mimic the extracellular matrix (ECM) [10] and SES products have been broadly applied towards different tissues [11]. Improvements of SES fabrication towards bone TE have also been recently reviewed by Ma *et al.* [12] and Wang *et al*. [13]. Although both biologically-derived and synthetic polymers can be processed using SES, poly(ε-caprolactone) (PCL) is particularly well suited for TE applications, as reviewed by Mokhena *et al*. [14]. In particular for bone TE, PCL remains a good option due to its established clinical use in this tissue, slow biodegradation rate and mechanical tunability [15]. The SES mesh provides a high surface area that supports cellular adhesion and proliferation, thereby promoting osteogenesis both *in vitro* and *in vivo* [10]. Furthermore, successful regeneration of long bone defects with PCL has been

achieved with the delivery of osteoinductive growth factors such as bone morphogenic protein-2 (BMP-2) [7].

BMP-2 is a potent osteoinductive growth factor that promotes bone regeneration by recruiting mesenchymal stromal cells and driving their differentiation into osteoblasts [16-18] . However, its clinical use has been hindered by complications such as heterotopic ossification, soft tissue inflammation, and unpredictable inflammatory responses [19, 20]. Additional concerns include rapid systemic diffusion, inefficient protein retention at the target site, and the potential for reduced osteogenic efficacy due to burst release kinetics [20-22]. These adverse effects are largely attributed to the use of absorbable collagen sponges as delivery vehicles, which rely on weak electrostatic interactions to entrap BMP-2, leading to supraphysiological doses, poor localization and uncontrolled protein release [23, 24].

A primary challenge in the clinical translation of BMP-2 is achieving localized and sustained delivery. To mitigate adverse outcomes and reduce the required BMP-2 dose, recent strategies have emphasized controlled release systems and combinatorial delivery of complementary growth factors to modulate osteogenesis more precisely [23, 24]. For instance, affinity-based release systems that use ECM-mimetic molecules such as heparin have been explored to enhance retention and reduce burst release of BMP-2 [20]. However, each approach presents trade-offs in terms of specificity, bioactivity retention, and production feasibility.

One promising biomaterial strategy integrates SES PCL meshes with hydrogels to provide localized protein delivery [21]. A notable example by Kolambkar *et al.* demonstrated that SES PCL meshes combined with alginate hydrogels has shown to enhance the delivery profile of BMP-2 by creating a hydrated matrix conducive to cellular infiltration and prolonged growth factor availability [25]. Alginate is a biocompatible, biodegradable material derived from marine algae.

Venkatesan *et al.* reviewed a range of alginate composites for bone TE applications, demonstrating versatility of alginate [26]. Kolambkar's hybrid system preserved BMP-2 bioactivity while minimizing rapid diffusion [25]. Preclinical studies utilizing this hybrid SES/hydrogel system have demonstrated its efficacy in repairing critically-sized femoral defects in rats. PCL meshes containing alginate loaded with BMP-2 increased bone regeneration and improved biomechanical function compared to the clinical synthetic standard (collagen sponge) delivery [25]. Moreover, perforations in the SES mesh enhanced vascular infiltration, facilitating accelerated repair while preserving the structural integrity of the mesh. These results highlight the potential of TE hybrid systems in addressing the biological signaling for effective bone regeneration.

Although SES has been used for over two decades within the TE community, it is widely appreciated that SES faces challenges in scalability and high enough yield for large-scale production [27]. To address these challenges, our study introduces a novel fabrication improvement that decreases production time and increases reproducibility (**Figure S5.1**). We demonstrate a manufacturing workflow that is faster and more reproducible, requiring less focused active hours and materials, while yielding similar mechanical properties and equivalent *in vivo* outcomes.

2. Materials and Methods

Flat meshes (original design)

Flat meshes were produced as previously described [25]. Briefly, PCL pellets (Sigma-Aldrich, USA) were dissolved at 12% w/v in a 90:10 solvent mixture of hexafluoro-2-propanol and dimethylformamide (DMF) (Sigma-Aldrich, USA) and allowed to dissolve overnight under gentle agitation (16-24 h). The PCL polymer solution was loaded into a syringe (Becton Dickinson, USA), to which a 22G blunt stainless-steel nozzle (Jensen Global, Inc., USA) was attached. The

syringe was mounted on a syringe pump (Harvard Apparatus, USA) at a flow rate of 0.75 mL/h. Fibers were collected onto a flat copper plate coated with aluminum foil, positioned 20-23 cm from the nozzle tip. Electrospinning was carried out for 6 h under an applied voltage of 13-20 kV, supplied by a high-voltage power unit (Gamma High Voltage Research, USA), to produce a dense SES sheet. Residual solvents were allowed to evaporate by placing the fibers in a desiccator overnight.

The fabricated SES meshes were then utilized to construct tubular implants as previously described [25]. The SES flat sheet was placed in a laser cutter (Universal Laser Systems, USA) and cut to a rectangle of 20 mm x 13 mm using Universal Control Panel (UCP) interface (Universal Laser Systems, USA). These rectangular meshes were then wrapped around steel mandrels (McMaster-Carr, USA) to form tubes approximately 5 mm in diameter and 13 mm in length. Overlapping edges were bonded using UV-curable glue (DYMAX Corporation, USA), cured with a LED spot-curing lamp (DYMAX Corporation, USA).

Tubular meshes (new design)

For tubular meshes, PCL (PC-12 PURASORB, Corbion, USA) was dissolved at 15% (w/v) in a solvent mixture of dichloromethane (DCM; Sigma-Aldrich, USA) and dimethylformamide (DMF; Sigma-Aldrich, USA) in a 3-to-2 volume ratio. The solution was stirred gently overnight (16-24 h). A custom-based printer system was used to electrospin a uniform coating of PCL onto a 5 mm cylindrical collector (McMaster-Carr, USA). The polymer solution was loaded into a 3 mL syringe (FORTUNA, USA) with a 32G nozzle (McMaster-Carr, USA). The distance from printhead to collector was set to 13 cm. Pressure of 1 bar and voltage difference of 20 kV was applied. The mandrel movement was programmed with Mach3 software (Artsoft, USA) to uniformly cover the tubular mandrel for a duration of 2 h and 30 min (**Supporting Video S6.1**).

Then, a solder (Miniware TS80P-FU40, China) was used to melt through the SES membrane for a preprogrammed path to match the mesh design (**Supporting Video S6.2**). The solder tip was set to 400 °C, and AeroBasic software (Aerotech, USA) was used to program the solder path. The programmed solder path features the perforation pattern and the separation of the polymer coated mandrel into small segments. To finalize each mesh, a gentle perforation of the solder through each "X" shape is performed. This yields 1 mm diameter perforations, which have been shown to enhance vascular invasion during the repair process [25]. The resulting meshes are 5 mm in diameter and 13 mm in length, with 1 mm diameter perforations in an alternating pattern of 3 or 2 openings in each row. Once the soldering step is complete, the polymer coated mandrel is sprayed with 70% ethanol to detach the mesh from the aluminum mandrel and individual meshes are removed by hand.

Bone mesh characterization: imaging and measurements

Meshes were characterized using both light microscopy (Keyence, USA) and scanning electron microscopy (SEM) (Apreo 2, ThermoFisher Scientific, USA). For SEM, meshes were sputter coated with 5 nm gold (Hummer II, Technics, USA). Measurements were taken from light microscope and SEM images using integrated software. For thickness measurements of the SES membrane, seven points across the polymer membrane were chosen, and measurements were performed in three technical replicates. For the flat membrane, points were chosen in a diagonal line across the membrane. For the tubular membrane, points were chosen along the length of the tube, as represented in **Figure S5.2**. The thicknesses of SES membranes were measured using integrated software on the Keyence light microscope and are summarized in **Table S5.1**. The diameter of SES individual fibers was measured from three technical replicates using integrated software on the SEM and are summarized in **Table S5.2**.

Mechanical testing

Assessment of mechanical properties was performed using lateral compression comparing meshes produced by the original and solder-perforated manufacturing processes. An ElectroForce 3220 (TA Instruments, USA) was fitted with flat platens and a 1000 g load cell. Samples were placed in the horizontal position on the bottom platen, and the upper platen was lowered until a force of 0.1 g was registered. The reference length (mesh diameter) was recorded as the distance between the platens, and samples were compressed to 50% of reference diameter. To evaluate the resistance to fatigue, the testing procedure consisted of 20 compression cycles of 50% strain at 1 Hz. We evaluated 1) the trend in peak load over cycles by measuring the change in maximum force across cycles (i.e. the slope of the peaks across the 20 cycles), 2) peak load variability by measuring the fluctuation in peak force across cycles (i.e. difference between highest and lowest peak), and 3) stiffness fatigue: ratio of loading slope (stiffness) in cycle 1 divided by the loading slope in cycle 20). A MATLAB (version R2021a 9.10.0.1602886) custom script was used to extract and plot data.

Preparation of alginate hydrogel with growth factor

The RGD-functionalized alginate (FMC Biopolymer NOVATACH VLVG 4GRGDSP, Lot# BP2010-17) was dissolved in α-MEM (Corning, USA) to create a 3% (w/v) solution. Recombinant human BMP-2 (rhBMP-2, R&D Systems, USA) was reconstituted in 0.1% rat serum albumin (Sigma Aldrich, USA) and 4 mM HCl containing 3 µg of BMP-2 per defect. To cross-link the solution, a calcium sulfate (Sigma Aldrich, USA) slurry (0.21 g $CaSO_4$ per 1 mL deionized water) was added at a 25:1 ratio (35 µL $CaSO_4$ to 875 µL of alginate-rhBMP-2 mixture). Mixing was performed using two 1-mL syringes connected via a Luer-Lok syringe coupler (Cole-Parmer,

USA) to minimize air entrapment. The solutions were left to gel at room temperature for 30 minutes before being stored at 4 °C overnight. The hydrogels were used for surgical applications the next day, ensuring aseptic handling throughout all steps, including during syringe manipulation.

Sterilization

Prior to implantation, meshes were sterilized using ethylene oxide (EtO) (AN74i Andersen Sterilizer, USA) and allowed to degas for 5 days before surgery. With aseptic handling, mesh tubes were transferred to sterile 24-well plates (Corning, USA), immersed in approximately 200 µL of α-MEM (Invitrogen, USA) and stored at 4 °C overnight until ready for implantation.

Bone mesh implantation and analysis

An established critically-sized, 6 mm femoral segmental defect rat model was used in this study with 14-week-old female Wistar (Envigo) rats. All surgical procedures were approved by the University of Oregon's Institutional Animal Care and Use Committee (IACUC protocol #20-32). The rat model and surgical technique has been described previously [28]. Briefly, internal fixation plates made of Ultra-High Molecular Weight Polyethylene (UHMWPE) with two stainless steel plates were secured onto the left femur of rodents (**Figure 5.6**). After securing an internal fixation plate to the femur, 6 mm segmental defects were created in the mid-diaphysis. SES mesh tubes were placed in the defect region around the adjacent bone ends, allowing for an overlap of approximately 3.5 mm with the native bone ends at each end of the tubular mesh. After placing the mesh, pre-gelled 3% alginate with 3 µg BMP-2 was injected in the tube lumen using an 23G blunt stainless-steel needle (Sigma-Aldrich, USA).

In vivo analysis

In vivo micro-computed tomography (micro-CT) images were obtained at 2, 4 and 8 weeks after surgery to quantify bone formation within the defect region. Rats were anaesthetized by isoflurane and placed in an *in vivo* micro-CT rodent holder (Viva-CT-80, Scanco Medical, Bassersdorf, Switzerland). The femoral defect region was scanned at a 48 μm voxel resolution, a voltage of 55-kVp and a current of 145 μA. The radiotranslucent UHMWPE material of the fixation plate does not interfere with micro-CT scanning and therefore allows longitudinal evaluation of bone formation. To obtain a consistent volume of interest (VOI) for bone volume quantifications, only the central 5.5 mm of the 6 mm defect along the longitudinal plane was analyzed *in vivo* by drawing and stacking circular contours along the transverse plane that encompassed all callus tissue. A Gaussian filter (sigma = 1.2, support = 1) was used to suppress noise in the VOI, and a global threshold of 388 mg hydroxyapatite/cm^3 was applied, corresponding to half the density of intact cortical bone.

Statistical analysis

Statistical analysis was performed using GraphPad Prism version 10.2.2. Data were screened for outliers and tested for normal distribution through Shapiro-Wilk test. A paired t-test was performed using Mann-Whitney test in cases where $n < 8$ or data were not normally distributed. For thickness measurements, a two-way ANOVA was used to determine statistically significant differences between the thickness of the Original and New methods, while also evaluating any differences between batches. *In vivo* bone healing data were run with Kruskal-Wallis nonparametric test, followed by Dunn's multiple comparison's test. In all cases, tests were run with 95% confidence.

3. Results and Discussion

Current clinical practices to treat critically-sized bone defects rely on bone grafting for successful bone bridging. To avoid the need of graft tissue, critically-sized bone defects can be treated with local delivery of bone morphogenic protein 2 (BMP-2) with a tubular mesh designed to improve retention of BMP-2-loaded alginate [25, 29] within the defect region to facilitate new bone growth. In the previous mesh design, SES sheets were printed in flat sheets, perforations were introduced by laser cutting, and individual meshes were rolled up and glued into a desired diameter [25, 29]. The process of rolling up the flat membrane into a tubular shape and gluing the mesh into place is time consuming and introduces variability in overlaps across individual meshes. It also required manual dispensing of surgical glue to secure the flat meshes into tubular structures which pose a barrier to clinical translation. Therefore, the elimination of glue also improves the potential for commercializing this scaffold technology. These limitations not only compromise mechanical integrity and impact uniform diffusion of growth factors but also lead to the rejection of approximately 30% of meshes during fabrication and surgical implantation. During implantation of meshes produced in the original method, surgeons experienced high attrition rates because variable manufacturing caused tearing or mesh collapse. The purpose of this work is to improve production of bone sleeve meshes into a seamless manufacturing process that is faster and more reliable than current approaches.

Figure 6.1 illustrates the improved automated two-step manufacturing workflow of tubular meshes. PCL is electrospun directly onto a rotating mandrel to yield a uniform membrane at the desired diameter (5 mm) (**Figure 6.1A**). The second step uses a soldering iron tip to melt the PCL membrane corresponding to the preprogrammed designs (**Figure 6.1B**). Lastly, once the meshes were removed from the mandrel, perforations were finalized manually with a soldering iron to

indent the "X" shape placement to a 1 mm circle. The new meshes were thinner than the original design: 340 ± 46 µm for the new design compared to 807.8 ± 479.2 µm for the original design. For the original design, thickness was measured across a diagonal line in the flat SES membrane (**Figure S6.2A**) and thickness values were summarized in **Table S6.1**. For the new design, thickness measurements were taken along the length of the mandrel (**Figure S6.2C**), and recorded values were summarized in **Table S6.2**. The complete process is summarized in Supplementary **Figure S6.1**.

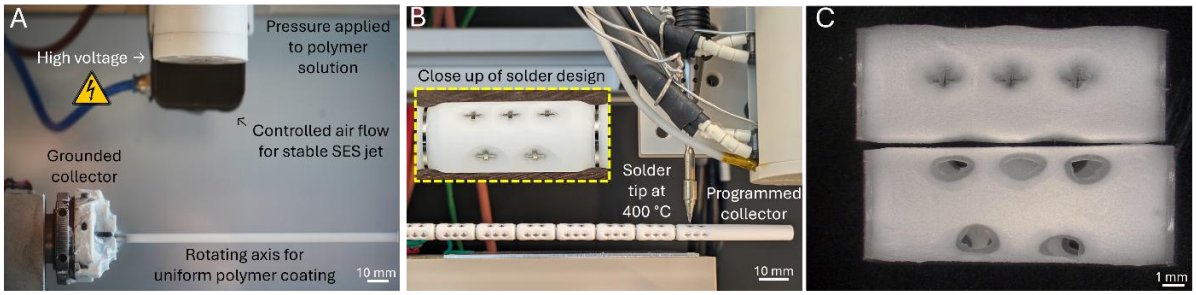

Figure 6.1. Tubular meshes manufactured in two steps: A) SES of PCL onto rotating mandrel for uniform coating. B) soldering of polymer membrane directly onto mandrel to create bone mesh design. C) resulting mesh with "X" shape soldered (top) and finalized design with solder after removal from mandrel (bottom). Scale bars: A-B) 10 mm; C) 1 mm.

A detailed investigation into the mesh perforation designs was performed (**Figure 6.2**). A representative image of the resulting tubular mesh is shown in **Figure 6.2A**, and a representative SEM image of the PCL fibers is shown in **Figure 6.2B**. Initially, a simple 1-second dot press of the soldering iron onto the mesh was used (**Figure 6.2C**) but resulted in a large melt area that fused the fibers rather than forming a perforated hole. We iterated to a square shape soldering pattern, but observed a "window" effect, where polymer remained within the perforation, which is not ideal. Finally, we found that a small "X" shaped perforation, with slight movement of the soldering

iron 0.3 mm each way (**Supplementary Video S6.2**), was most effective, as denoted by **Figure 2F.** Through several iterations, we resolved to finalize each mesh with a gentle perforation of the solder through each "X" shape after the meshes have been removed from the mandrel (**Figure 6.1C**). This way, we can keep the 1 mm diameter perforations in bone sleeves, which serve a dual purpose: 1) allowing entrance of the 23G needle required to deliver the BMP-2–loaded alginate gel; and 2) enhancing vascular invasion during the repair process [25]. While the integration of the soldering iron perforation method presents a process improvement in mesh fabrication, it also offers an automated, scalable and efficient approach for the final shaping of a range of scaffolds and meshes made from thermoplastic polymers beyond PCL.

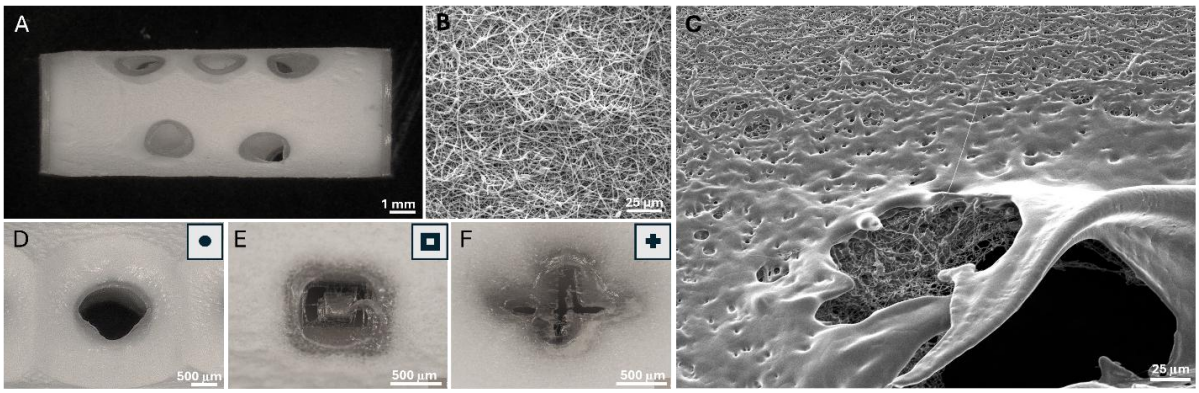

Figure 6.2. Bone mesh characterization via A) light microscopy to observe mesh features and B-C) scanning electron microscopy (SEM) for close-up of solution electrospun (SES) fibers. B) Representative SEM image of SES fibers and C) representative SEM of molten polymer in the area surrounding solder following exposure to high temperature. D-F) Light microscope images after removal from mandrel that show proposed pattern for solder perforation and resulting pattern on the SES mesh. Scale bars: A)1 mm; B) 25 µm; C) 25 µm; D-F) 500 µm.

We then evaluated the differences between the original design (printed as a flat sheet then rolled and glued) and new design (printed as a tubular structure) in terms of mesh morphology, production time, viability for surgical use, and mechanical properties (**Figures 6.3-4**). One major improvement between the original and new designs is the absence of the overlapping section/seam required to glue the flat meshes into a tube (**Figures 6.3B and 3E**). Previously, when manufacturing meshes using the original method, production time would average 8.7 h for 10 viable meshes. SES would take 6-8 h (passive time) and would be monitored by visual inspection. The flat ES membrane was laser cut into rectangles with perforations, then rolled up individually and glued into a cylindrical shape. Our new method reduced production time from 8.7 h to 2.7 h for 10 viable meshes. The current production time for a batch of 10 meshes involves a SES step of 2 h 30 min (passive time) and subsequently a 2-3 min soldering step (passive time), followed by final manual perforations yielding 1 mm circles of less than 1 min/mesh (active time). The decrease in production time for a batch of 10 meshes, represented in **Figure 6.3H**, excludes dissolving the polymer overnight prior to SES, which is required for both original and new manufacturing processes. Our new manufacturing process resulted in a more uniform thickness, increased reproducibility, and decreased active and total manufacturing time.

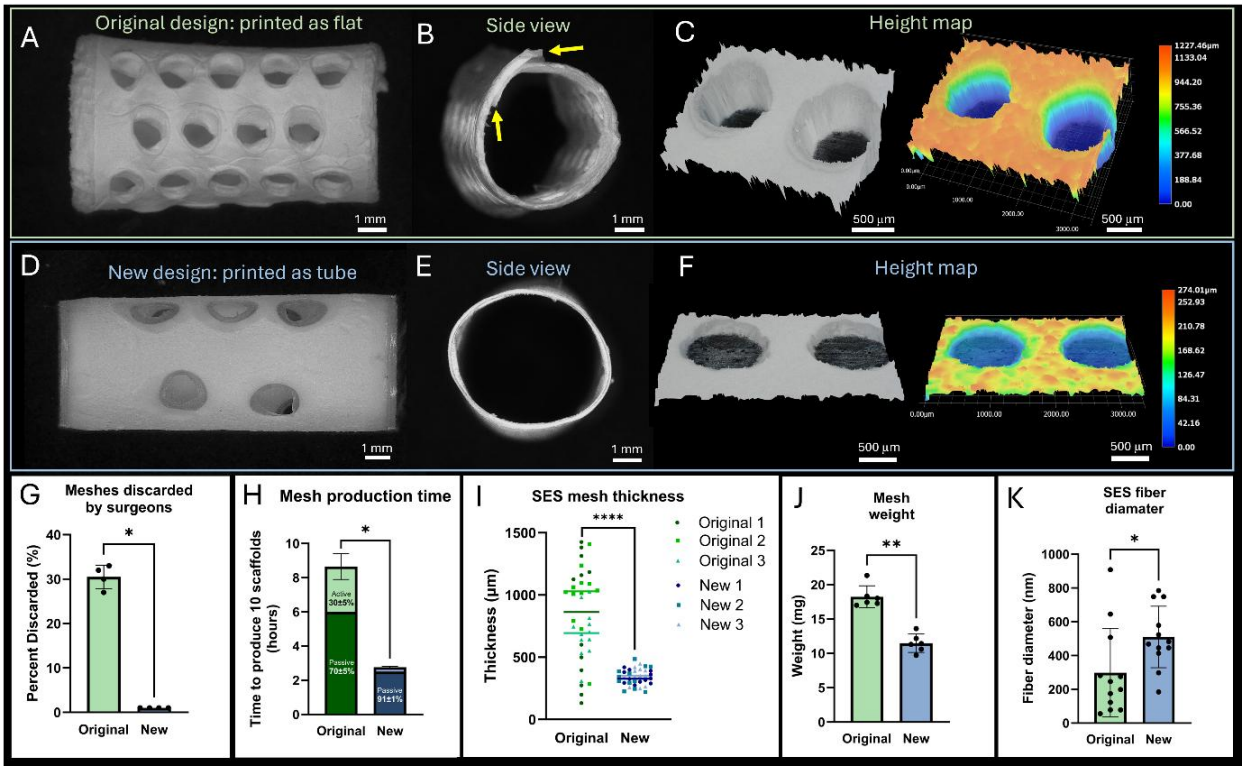

Figure 6.3. Evaluation of differences in meshes printed as flat and then rolled up (original) versus meshes printed as tubes (new). A) Light microscope image of tube printed as a flat membrane and rolled up into tube (original) and B) corresponding side view. Yellow arrows indicate an overlap along the seams. C) Representative height map and corresponding color-coded heat map rendered from z-stack. D) Light microscope image of mesh printed as tube (new) and E) corresponding side view. F) Representative height map and corresponding color-coded heat map rendered from z-stack. G) Percentage of meshes discarded by surgeons. With the new mesh design, all of the meshes prepared and treated are used in surgery, whereas before, about 30% would be discarded due to suboptimal mechanical integrity. H) Production time for 10 meshes. There is a decrease in production time from 8.7 h to 2.7 h production time for original versus new design, respectively. I) Mesh thickness: the new design shows thinner meshes and a more uniform thickness profile. J) Mesh weight: new scaffolds are made with less material (18.24 ± 1.5 mg for old versus 11.48 ± 1.2 mg for new design). K) Fiber diameter of solution electrospun fibers: both manufacturing

*processes show similar disparity in SES fiber diameter, as expected, although a larger fiber diameter on average was recorded for the new design. *, $p \leq 0.05$; **, $p \leq 0.005$; ****, $p \leq 0.0001$. Scale bars: A-B) and D-E) 1 mm; C and F) 500 µm.*

As the surgeons evaluated mesh surgical utility of the original design, it was reported that meshes would lose their tubular shape at the overlapping seam where it had been glued together (**Figure 6.3B and D**), resulting in about 30% of meshes to be discarded due to insufficient mechanical strength (**Figure 6.3G**) after submersion in DMEM. By printing the meshes as tubular structures (**Figure 6.3C**), these meshes became 99% viable for use in the surgical suite, reflecting improved reliability and reduction in time for surgical procedure due to less discarded meshes during surgery (**Figure 6.3H**). Thickness of meshes was reduced on average 2.4-fold, and **Figure 3I** showed a more uniform thickness distribution for the new design compared to the original. This time-saving effort was also reflected in reduction of reagents due to lower mesh weight (18.24 ± 1.5 mg for old versus 11.48 ± 1.2 mg for new design) (**Figure 6.3J**), ranging from the mesh raw materials (PCL and its solvents) as well as reagents needed for post processing such as alpha-MEM and BMP-2 loaded alginate. We also found an increase in average SES fiber diameter (**Figure 6.3K**), although, as expected, the SES fiber diameter was varied for both designs: 298 ± 250 µm to 510 ± 174 µm for original to new design, respectively. This variation in SES fiber diameters falls within typical SES values reported in the literature [30]. With the new tubular design, all meshes that were prepared, sterilized, and pre-treated were implanted by surgeons, representing a higher surgeon satisfaction rate and reduction in time and reagents.

Lateral compression tests were performed on tubular meshes to compare the fatigue of original versus the new design in the dry state (**Figure 6.4**). The trend in peak load over cycles (measured by the slope of the peaks across the 20 cycles) showed no differences between original

and new design (**Figure 6.4A**). The peak load variability (measured by calculating the difference between highest and lowest peak) also showed no differences between designs (**Figure 6.4B**). Lastly, the stiffness fatigue (measured by dividing the ratio of loading slope in cycle 1 by that of the loading slope in cycle 20) showed values close to 1, indicating stable stiffness across 20 loading cycles in both the original and new design, with no significant differences (**Figure 6.4C**). Summary of outputs from lateral compression is shown in **Figure S6.5**. **Supplementary Video S6.3** shows a recording of the new mesh design undergoing lateral compression testing. Overall, our data showed that the new tubular meshes exhibited similar and uniform resistance to compression compared to the original design under dry testing conditions, regardless of having a smaller mass.

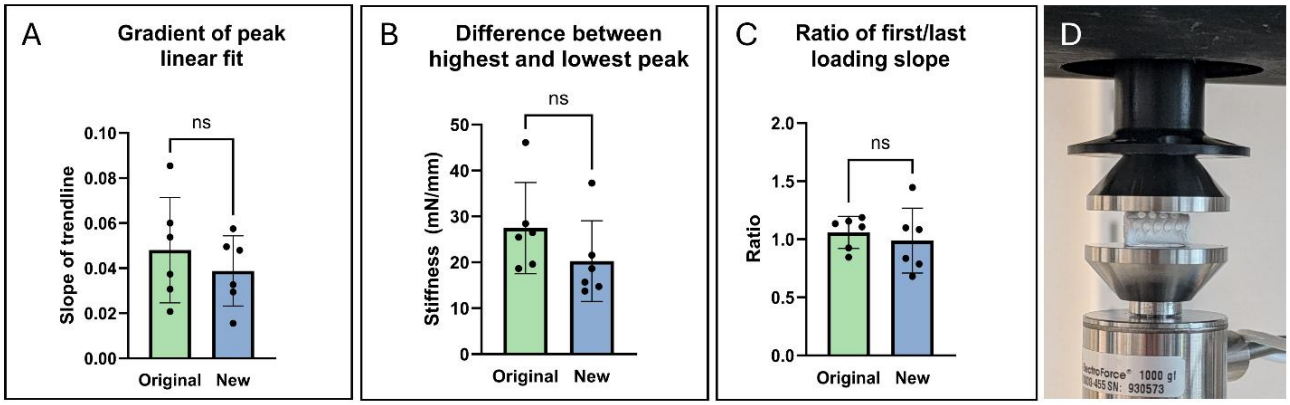

Figure 6.4. Resistance to fatigue measured by resistance to lateral compression evaluated. A) Gradient of peak linear fit, B) difference between highest and lowest peak, C) ratio of first/last loading slope. ns = non-significant. More details are provided in Figure S6.5. D) Photograph of original mesh design loaded for lateral compression setup.

In addition to evaluating the meshes' resistance to fatigue, it was important to verify that the new design retains the locally injected alginate gel loaded with BMP-2. **Figure S6.3** shows the surgical utility of meshes with tweezers both dry and holding the alginate gel. Once loaded with gel, the mesh maintains its tubular shape (**Figure S6.3C**).

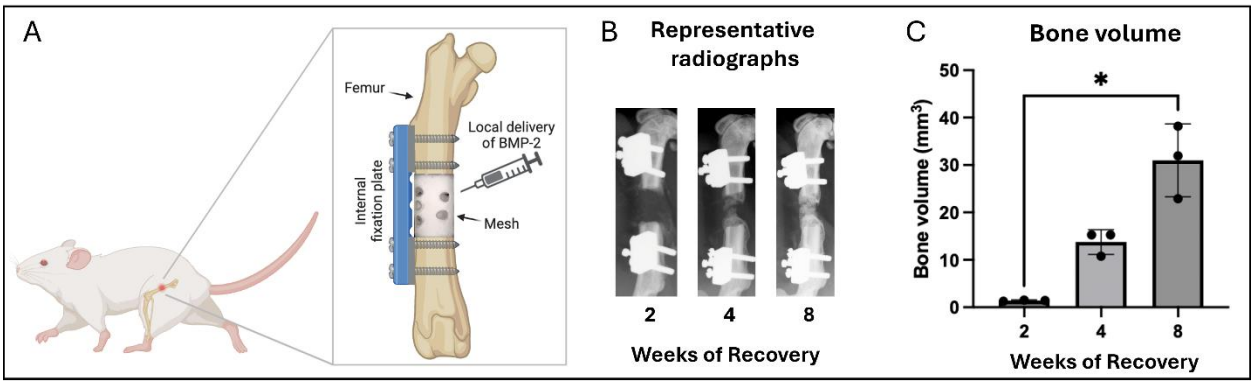

*Figure 6.5. In vivo study with new meshes facilitated bone healing over time. A) Segmental defect model diagram with mesh and local delivery of BMP-2 within the defect region. Created with biorender.com. B) Representative radiographs after 2, 4 and 8 weeks of recovery from 6 mm segmental femur defect surgeries. C) Longitudinal bone volume quantifications of newly formed bone within the defect region. Kruskal-Wallis nonparametric test revealed significant effect of time (**, p = 0.0036) and Dunn's multiple comparison's test revealed significant increase in bone volume from week 2 to week 8 (*, p = 0.0211).*

In vivo experiments were performed to evaluate the safety and function of the newly manufactured meshes. For this experiment we utilized a critically-sized segmental defect model in rodent femurs (**Figure 6.5A**). The mesh design used for this experiment was based on previous studies that established the 1 mm perforations as advantageous for vascular ingrowth and bone healing, while retaining the injected BMP-2 loaded alginate [25]. Surgery was performed to create the 6 mm bone injuries, and bone regrowth was monitored across weeks 2, 4 and 8 using *in vivo*

radiographs and micro-CT scans. As expected, bone volume significantly increased over time across all subjects due to the local delivery of BMP-2 within the new meshes (**Figure 6.5B and C**). Within this model, the perforated meshes ensured that BMP-2 remains in the defect region with controlled diffusion to facilitate BMP-2 mediated bone healing. It is worth noting that new bone growth did not expand the entire defect region in some regions due to the minimally effective dose (3 μg) of BMP-2 used in this model (**Figure 6.5B**). More robust bridging could be achieved with a slightly higher dose of BMP-2 as shown across previous studies which used a 67% higher dose [17]. Importantly, high doses of BMP-2 can lead to excessive bone growth and inflammation so growth factor doses could be explored incrementally within the current standard (up to 5 μg) [17]. Implantation of the new meshes did not impact rodent recovery as no post-operative complications occurred and no adverse tissue responses were noted during dissection after 8 weeks of implantation. Overall, the new meshes with a more reliable and high-throughput manufacturing capabilities, exhibited efficient implantation at time of surgery, achieved safe and successful mesh integration, and mediated local release of BMP-2 to facilitate bone healing in our well-characterized bone injury model.

4. Conclusion

In this study, we introduced an automated manufacturing workflow to fabricate PCL electrospun meshes used to treat bone defects. Our approach successfully streamlined the manufacturing process, reduced fabrication time, improved reproducibility, and enhanced surgical utility, while maintaining treatment efficacy, as demonstrated by significant bone growth in rodent *in vivo* model. The traditional mesh production relied on manual rolling and adhesive bonding that introduced a high degree of variability to the mesh thickness and geometry (**Figure 6.3**). In contrast, our automated method directly deposited electrospun PCL onto a cylindrical mandrel,

eliminating structural weaknesses associated with overlapping seams and batch to batch variability due to consistency of user assembly and varying amounts of surgical glue. The result of our new methodology is a mesh that is faster to produce and highly reproducible in terms of diameter, weight, and resistance to lateral compression via integration of an automated soldering iron for perforation system.

Future work will focus on higher-precision soldering tips to minimize fiber fusion zones and increase the design space for SES PCL meshes. This will open the scaffold design space towards further tuning growth favor diffusion rates depending on perforation pattern and size.

Overall, this study demonstrates the utility of automated manufacturing techniques that include subtractive approaches to enhance the clinical applicability of electrospun meshes, paving the way for more effective and reproducible bone regeneration strategies.

5. Acknowledgements

The financial support from the Wu Tsai Human Performance Alliance and the Joe and Clara Tsai Foundation is greatly appreciated. PD is supported by the Bradshaw and Holzapfel Research Professor in Transformational Science and Mathematics Fund. The *in vivo* animal study was supported by the National Institutes of Health under Grant R01 AR069297. Tyler Guyer and Lia K. Strait contributed to the *in vivo* validation of the bone meshes used in this study. The authors appreciate the support from Kelly E. H. Leguineche and Samuel R. Nightheart.

6. References

[1] Borrelli, Joseph Jr., W. D. Prickett, W. M. Ricci, *Clinical Orthopaedics and Related Research*® **2003**, 411, 245.

[2] R. Dimitriou, G. I. Mataliotakis, A. G. Angoules, N. K. Kanakaris, P. V. Giannoudis, *Injury* **2011**, 42 Suppl 2, S3.

[3] A. H. Schmidt, *Injury* **2021**, 52 Suppl 2, S18.

[4] W. F. Enneking, D. A. Campanacci, *JBJS* **2001**, 83, 971.

[5] R. E. Guldberg, M. E. Oest, K. Dupont, A. Peister, E. Deutsch, Y. Kolambkar, D. Mooney, *J Musculoskelet Neuronal Interact* **2007**, 7, 333.

[6] M. E. Oest, K. M. Dupont, H.-J. Kong, D. J. Mooney, R. E. Guldberg, *Journal of Orthopaedic Research* **2007**, 25, 941.

[7] L. Krishnan, L. B. Priddy, C. Esancy, M.-T. A. Li, H. Y. Stevens, X. Jiang, L. Tran, D. W. Rowe, R. E. Guldberg, *Clinical Orthopaedics and Related Research*® **2015**, 473.

[8] S. Bhushan, S. Singh, T. K. Maiti, C. Sharma, D. Dutt, S. Sharma, C. Li, E. M. Tag Eldin, *Bioengineering (Basel)* **2022**, 9.

[9] A. G. Abdelaziz, H. Nageh, S. M. Abdo, M. S. Abdalla, A. A. Amer, A. Abdal-Hay, A. Barhoum, *Bioengineering (Basel)* **2023**, 10.

[10] Y. Su, M. S. Toftdal, A. Le Friec, M. Dong, X. Han, M. Chen, *Small Science* **2021**, 1, 2100003.

11] M. Z. A. Zulkifli, D. Nordin, N. Shaari, S. K. Kamarudin, *Polymers (Basel)* **2023**, 15.

[12] Y. Ma, R. Zhou, M. Yang, J. Zhang, W. Song, X. Ma, M. Liu, X. Cui, B. Li, Y. Zhang, Y. Long, Z. Zhou, C. Li, *Materials & Design* **2025**, 252.

[13] X. Wang, Y. Guo, P. Liu, X. Chen, H. Zhou, *Polymer-Plastics Technology and Materials* **2025**, 64, 2019.

[14] T. C. Mokhena, M. B. Chabalala, S. Mapukata, A. Mtibe, L. Hlekelele, Z. Cele, M. J. Mochane, B. Ntsendwana, T. A. Nhlapo, T. P. Mokoena, M. F. Bambo, K. P. Matabola, S. S. Ray, E. R. Sadiku, K. Shingange, *Macromolecular Materials and Engineering* **2024**, 309.

[15] R. Dwivedi, S. Kumar, R. Pandey, A. Mahajan, D. Nandana, D. S. Katti, D. Mehrotra, *Journal of Oral Biology and Craniofacial Research* **2020**, 10, 381.

[16] K. Miyazono, Y. Kamiya, M. Morikawa, *J Biochem* **2010**, 147, 35.

[17] Y. M. Kolambkar, J. D. Boerckel, K. M. Dupont, M. Bajin, N. Huebsch, D. J. Mooney, D. W. Hutmacher, R. E. Guldberg, *Bone* **2011**, 49, 485.

[18] J. Sun, J. Li, C. Li, Y. Yu, *Mol Med Rep* **2015**, 12, 4230.

[19] A. W. James, G. LaChaud, J. Shen, G. Asatrian, V. Nguyen, X. Zhang, K. Ting, C. Soo, *Tissue Eng Part B Rev* **2016**, 22, 284.

[20] M. H. Hettiaratchi, L. Krishnan, T. Rouse, C. Chou, T. C. McDevitt, R. E. Guldberg, *Science Advances* **2020**, 6, eaay1240.

[21] H. D. Kim, R. F. Valentini, *Journal of Biomedical Materials Research* **2002**, 59, 573.

[22] A. F. Kamal, O. S. H. Siahaan, J. Fiolin, *Arch Bone Jt Surg* **2019**.

[23] P. S. Briquez, H.-M. Tsai, E. A. Watkins, J. A. Hubbell, *Science Advances* **2021**, 7, eabh4302.

[24] J. D. Boerckel, Y. M. Kolambkar, K. M. Dupont, B. A. Uhrig, E. A. Phelps, H. Y. Stevens, A. J. Garcia, R. E. Guldberg, *Biomaterials* **2011**, 32, 5241.

[25] Y. M. Kolambkar, K. M. Dupont, J. D. Boerckel, N. Huebsch, D. J. Mooney, D. W. Hutmacher, R. E. Guldberg, *Biomaterials* **2011**, 32, 65.

[26] J. Venkatesan, I. Bhatnagar, P. Manivasagan, K. H. Kang, S. K. Kim, *Int J Biol Macromol* **2015**, 72, 269.

[27] A. D. Tsareva, V. S. Shtol, D. V. Klinov, D. A. Ivanov, *Surfaces* **2025**, 8.

[28] L. Krishnan, L. B. Priddy, C. Esancy, B. S. Klosterhoff, H. Y. Stevens, L. Tran, R. E. Guldberg, *Acta Biomaterialia* **2017**, 49, 101.

[29] R. Subbiah, M. A. Ruehle, B. S. Klosterhoff, A. S. P. Lin, M. H. Hettiaratchi, N. J. Willett, L. E. Bertassoni, A. J. García, R. E. Guldberg, *Acta Biomaterialia* **2021**, 127, 180.

[30] A. K S, P. Sanpui, K. Chatterjee, *journal of polymer and biopolymer physics chemistry* **2014**, 2, 62.

CHAPTER 7: COMMERCIALIZATION STRATEGY FOR MEW-FABRICATED NERVE GUIDANCE CONDUITS

This chapter presents the commercialization plan of a nerve guidance conduit under the working name PeriMend3D. PeriMend3D represents a hypothetical and unregistered company concept advanced through entrepreneurship programs at the University of Oregon and the OIC to explore the clinical translation potential of MEW-based scaffold technologies. Building upon the scientific foundation of MEW, this chapter bridges the gap between experimental scaffold design and the translational frameworks required for medical device development. It demonstrates how high-resolution 3D printing, regulatory planning, and market-informed design converge to carry biomedical research into a viable clinical and commercial innovation. PeriMend3D serves as a case study in translating biomaterial research toward patient-centered applications.

Commercialization Plan for PeriMend3D

Kelly L. O'Neill

This document presents a commercialization plan that outlines the pathway to translate PeriMend3D's melt electrowriting (MEW)-fabricated nerve guidance conduit (NGC) from laboratory innovation to clinical and market adoption. Anchored in doctoral research in bioengineering, PeriMend3D leverages micron-scale fiber control to produce customizable, shelf-stable conduits designed to address the limitations of autografts, allografts, and existing synthetic devices. The plan integrates scientific validation with market evidence gathered through structured interviews with surgeons and medical device specialists, aligning product design with key priorities such as performance, handling, and storage efficiency.

This commercialization plan progresses from opportunity to implementation. It defines market size and segmentation, identifying traumatic hand surgery as the initial target market with potential expansion into broader reconstructive and regenerative applications. It articulates the value proposition as precision architecture, reliable handling, and elimination of cold-storage requirements compared to current clinically available options. Technical feasibility is demonstrated through design refinements guided by clinician feedback, including packaging improvements, standardized sizing, and the eventual integration of a collagen coating to enhance cell attachment and in turn improve clinical outcomes.

A defined regulatory strategy outlines a 510(k)-clearance pathway supported by biocompatibility, sterility, and performance data, while the Business Model Canvas summarizes key partners, activities, distribution channels, and revenue streams. The go-to-market plan emphasizes early clinical partnerships, engagement of key opinion leaders, representative-led training programs, and a consignment-based approach to facilitate product evaluation and

adoption. Five-year financial projections, staged funding sources (STTR/SBIR, angel, Series A), and milestone-driven development ensure alignment between capital investment, regulatory progress, and commercialization readiness. An executive summary at the conclusion of this business plan consolidates these components, providing a comprehensive overview of PeriMend3D's strategy, financial trajectory, and translational potential.

Finally, the plan situates PeriMend3D within the broader framework of the doctoral thesis, demonstrating how rigorous biofabrication research, combined with entrepreneurial methodology, can advance patient-centered medical devices and contribute to sustainable innovation in regenerative medicine.

Introduction and Context

Peripheral nerve injuries compromise essential motor and sensory functions, affecting millions worldwide. Standard interventions, while clinically accepted, remain inadequate for large-gap nerve damage, leading to permanent disability and poor quality of life. Autografts remain the gold standard but are limited by donor nerve availability and morbidity. Cadaveric allografts such as AxoGen's Avance graft offer alternatives but require stringent cold storage and pose immune risks. Synthetic conduits, though shelf-stable, frequently collapse or fail to guide nerve regeneration effectively.

PeriMend3D introduces a new paradigm in peripheral nerve repair by uniting bioengineering research and clinical insight. The nerve guidance conduit, fabricated using MEW, provides structural precision at the microscale, guiding regenerating axons while maintaining mechanical stability (**Figure 7.1**). The company leverages expertise in MEW scaffold design, neural cell culture, and translational bioengineering to deliver a clinically adaptable, shelf-stable, and high-performance device.

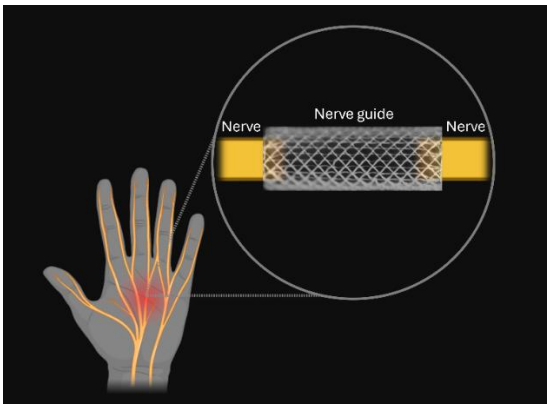

Figure 7.1. Schematic representation of the PeriMend3D nerve guidance conduit (NGC) fabricated using MEW. The design illustrates aligned fibers and crosshatch architecture that provide directional cues for axonal growth and mechanical reinforcement, bridging the gap between injured nerve ends while maintaining structural integrity.

Market Analysis

Market Overview

The global peripheral nerve repair market was valued at $7.5 billion in 2020 and is projected to exceed $11 billion by 2028. Growth is driven by the rising incidence of trauma-related injuries, post-surgical reconstructions, and chronic nerve conditions. Approximately 20 million individuals suffer from PNIs annually, with about 10% requiring surgical intervention. The United States accounts for nearly a third of these cases, representing a robust entry point for PeriMend3D.

Market Segmentation and Beachhead Market

Through iterative market validation and interviews with clinicians, two promising market segments emerged:

1. Traumatic Hand Surgery: High frequency of nerve repairs, strong adoption of new technologies within university and orthopedic hospitals, and clear reimbursement pathways.

2. Breast Reconstruction After Mastectomy: Identified in later interviews as a rapidly expanding niche, aligning with trends toward natural-feeling, biologically integrated reconstruction materials for breast cancer survivors.

The initial commercialization strategy targets hand surgery as the beachhead market where surgeons are receptive to innovation and procedures are frequent, followed by expanding into breast reconstruction and broader reconstructive applications. The complete list of market segments is shown in **Figure 7.2**.

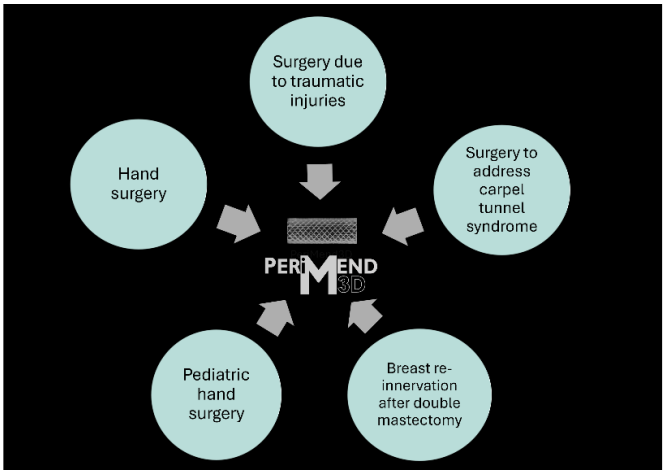

Figure 7.2. Market Segmentation and Beachhead Market Selection. Visualization of the market assessment identifying traumatic hand surgery and breast reconstruction as high-potential entry points based on size, demand, and clinical feasibility.

Market Drivers

- Technological advancements in biofabrication and biocompatible polymers.
- Growing demand for minimally invasive and regenerative procedures.
- Rising healthcare expenditure supporting advanced biomaterials.
- Increasing surgeon interest in synthetic alternatives that reduce donor-site morbidity.

Competitive Landscape

A complete list of FDA-approved nerve guides is summarized in **Table 7.1**. PeriMend3D competes primarily against AxoGen's processed allografts and synthetic conduits from companies such as Integra and Polyganics. As revealed through surgeon interviews, these competitors fail to meet key expectations in performance, shelf-life, and customization. PeriMend3D's MEW-printed conduits combine structural reliability, controlled degradation, and ease of use, which directly address these gaps (**Figure 7.3**).

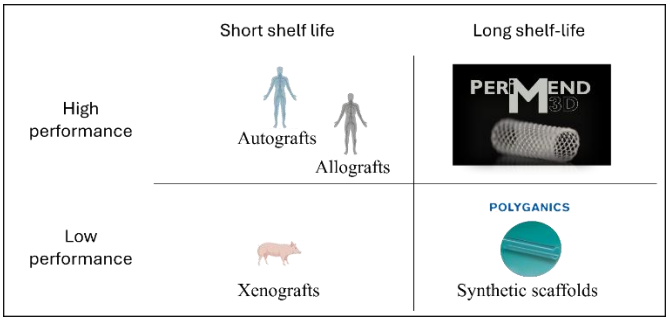

Figure 7.3. Competitive Positioning and Value Proposition Matrix. Comparative analysis positioning PeriMend3D relative to existing autografts, allografts, and synthetic conduits, highlighting superior performance, shelf stability, and handling characteristics.

Interview-Derived Insights

Dr. Bruce Watkins (hand surgeon) emphasized that surgeons value shelf-life and ease of use above marginal price differences. The necessity of ordering cadaveric grafts on dry ice 24 hours in advance represented a significant logistical barrier that PeriMend3D eliminates. Dr. Raj Midha (neurosurgeon, specialist in peripheral nerve) highlighted the absence of effective products for bridging nerve gaps exceeding 3 cm, confirming a technical opportunity for long-gap repair. These insights informed PeriMend3D's design and market entry strategy, ensuring direct alignment between clinical pain points and product functionality.

Table 7.1. Commercially available FDA-approved nerve conduits organized chronologically

Product name	Composition	Structure	Diameter	Length	Degradation time	Manufacturer
Neurotube ™	Poly(glycolic acid)	Absorbable woven PGA mesh	2-8 mm	4 cm	3 months	Synovis Micro Companies Alliance
SaluBridge ™	Salubria® Poly(vinyl alcohol	PVA hydrogel tube	2-10 mm	6.35 cm	No degradation	SaluMedica LLC
NeuraGen ™	Type I collagen	Semipermeable, fibrillar collagen hollow tube	2-7 mm	2 cm	4 years	Integra Neuroscience
NeuroMatrix ™ Neuroflex ™ Neuromend ™	Type I collagen	Semipermeable tubular collagen matrix	2-6 mm	2.5 cm	7 months	Collagen Matrix Inc.,
AxoGuard Nerve Connector ™	Small intestine submucosa	Thin and porous membrane	2-5 mm	4 cm	6 months	Axogen Corp.,
Avance ™	Decellularized human nerve allograft	Native peripheral nerve ECM	1-5 mm	7 cm	3-4 months	Axogen Corp.,
Neurolac ®	Poly(lactide-co-caprolactone)	PLCL hollow tube	1.5-10 mm	3 cm	16 months	Polyganics BV, Netherlands
NeuraGen 3D ™	Type I collagen	Outer semi-permeable membrane with enriched inner matrix	1.5-7 mm	2-3 cm	3 years	Integra Neuroscience
Reaxon® Nerve Guide	Chitosan	Permeable hydrogel hollow tube	2.1-6 mm	3 cm	2.5 years	Medovent, Mainz, Germany (KeriMedical group)
Nerbridge ™	Collagen and polyglycolic acid (PGA)	Outer collagen coating with PGA layer and inner collagen matrix	0.5-4 mm	2.5 cm	3 months	TOYOBO Co., LTD. Japan
NeuroShield ™	Chitosan	Thin and porous membrane	9-12 mm	3-4 cm	18 months	Monarch Bioimplants GmbH Switzerland
VersaWrap ™	Hyaluronic acid and alginate	Thin membrane OR injectable hydrogel	Variable	Variable	2 years	Alafair Biosciences

Value Proposition and Product Differentiation

PeriMend3D's nerve guidance conduit offers three core differentiators:

1. Customization and Precision: MEW technology allows for fine-tuned fiber architecture that replicates the extracellular matrix and can be tailored to patient-specific anatomy.
2. Shelf Stability and Logistics: Synthetic, sterilized scaffolds that require no cold storage, enabling hospitals to maintain ready-to-use inventory.
3. Superior Handling and Biocompatibility: Thin yet strong walls ensure easy suturing and integration within existing surgical workflows.

These features directly reflect surgeon feedback. Dr. Watkins' emphasis on convenience led to the adoption of simplified packaging and a standardized range of scaffold sizes. Ongoing advancements include Dr. Ken Weeks' (tendon treatment medical device specialist) suggestion to incorporate a collagen coating to improve cell adhesion and biocompatibility, while maintaining the synthetic scaffold's integrity.

Compared to autografts and allografts, PeriMend3D eliminates the need for additional surgeries, reduces infection risk, and shortens procedure time. Its synthetic nature ensures consistent quality and scalability, unlike donor-dependent alternatives. Compared to current synthetic conduits, it offers alignment cues and a balance between mechanical flexibility and integrity, preventing collapse while remaining flexible.

Technical Feasibility and Development Plan

Technology Foundation

PeriMend3D's platform leverages MEW to produce microscale fibers with controlled orientation, creating a porous, bioresorbable scaffold, designed to promote directional axonal

regeneration. This precision allows for custom permeability and stiffness profiles to suit varying nerve gap lengths. The design and material selection supports a predicted degradation within 6-9 months post implant, aligning with typical peripheral nerve healing timelines.

Preclinical Development

The preclinical pathway has been shaped through collaborations with experts across disciplines:

1. Dr. Rebecca Fredrick advised on optimizing experimental parameters using Design of Experiments (DoE) to streamline pilot studies.
2. Dr. Kait Link provided regulatory and logistical oversight for animal research, emphasizing sterility, team coordination, and endpoint definition.
3. Prof. Benjamin Aleman supported statistical modeling via design of experiments to reduce animal use while maximizing data quality.

Mechanical and suture retention tests are currently underway, evaluating tensile strength, bending stiffness, and suture pull-out resistance. Future *in vivo* pilot studies will utilize a supra-critical size rat sciatic nerve model. Outsourcing histological analysis to INOTIV will accelerate the data pipeline and ensures standardized results.

Design Improvements from Interviews

Interviews directly informed technical refinements:

- Collagen Coating: suggested by Dr. Weeks to enhance cell adhesion.
- Multiple Product Formats: inclusion of nerve wraps alongside tubes following Dr. Watkins' recommendation for broader clinical use.
- Sterilization Workflow: adapted to ethylene oxide (EtO) gas with a 7-day degassing period, as outlined by Dr. Link and Dr. Williams.

These data-driven refinements align the conduit's specifications with both surgical practicality and regulatory readiness.

Regulatory Strategy

PeriMend3D's conduit qualifies for the FDA 510(k) pathway as a Class II medical device, given its substantial equivalence to existing synthetic nerve guides. The regulatory plan involves three phases:

- Preclinical Phase: Completion of small- and large-animal studies validating safety, degradation, and functional recovery (Years 1-2).
- Regulatory Submission Preparation: Compilation of biocompatibility, sterility, and mechanical data, with expert consultation to ensure compliance.
- Clinical Trials and 510(k) Submission: Execution of human clinical trials in collaboration with university hospitals (Years 3-4), followed by FDA clearance and commercialization in Year 5.

The regulatory timeline is integrated within the financial model to ensure resource alignment across technical, clinical, and administrative milestones.

Business Model Canvas

- Key Partners: University laboratories (Knight Campus), clinical collaborators (OHSU, Slocum Clinic), regulatory consultants, manufacturing partners, distributors.
- Key Activities: Scaffold fabrication, sterilization, mechanical testing, regulatory compliance, clinical trials, surgeon education, marketing.
- Key Resources: MEW printing infrastructure, bioengineering expertise, IP portfolio, regulatory know-how, strategic partnerships.
- Value Proposition: Premium nerve guides designed to simplify surgery while supporting superior recovery rates; shelf-stable and customizable.

- Customer Relationships: High-touch engagement through surgeon training, clinical partnerships, and post-adoption support.
- Channels: Direct sales via medical device representatives; strategic hospital partnerships; licensing to research institutions.
- Customer Segments: Peripheral nerve surgeons, reconstructive and plastic surgeons, hospitals, and research institutions.
- Cost Structure: R&D, regulatory, manufacturing, marketing, and distribution expenses.
- Revenue Streams: Direct sales, licensing, R&D collaborations, and future expansion into adjacent reconstructive applications.

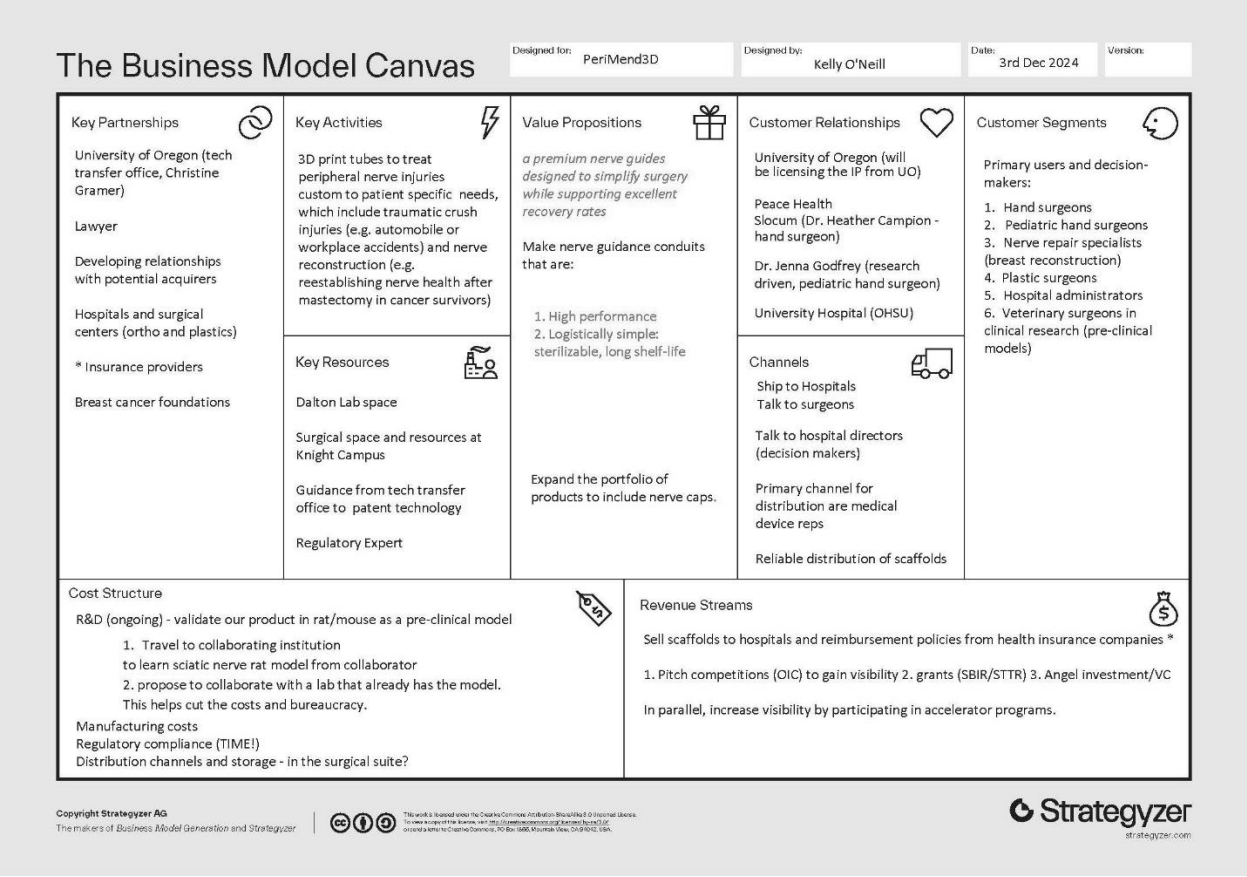

Figure 7.4. Business Model Canvas for PeriMend3D. Summary of key components guiding the commercialization of MEW-fabricated nerve conduits, including partners, activities, value proposition, and revenue streams.

Go-to-Market Strategy

PeriMend3D's market entry emphasizes surgeon trust and clinical evidence. The strategy unfolds in three stages, as depicted in **Figure 7.5**:

1. Early Adoption (Years 1-2): Engage university hospitals and teaching institutions as clinical partners to generate data and refine surgical protocols.
2. Expansion (Years 3-4): Leverage early adopters as ambassadors to reach private practices and large hospital systems. Dedicated medical device representatives will facilitate training and relationship building.
3. Scaling (Year 5 onward): Broaden product distribution nationally, integrate digital marketing and continuing medical education workshops, and explore international licensing.

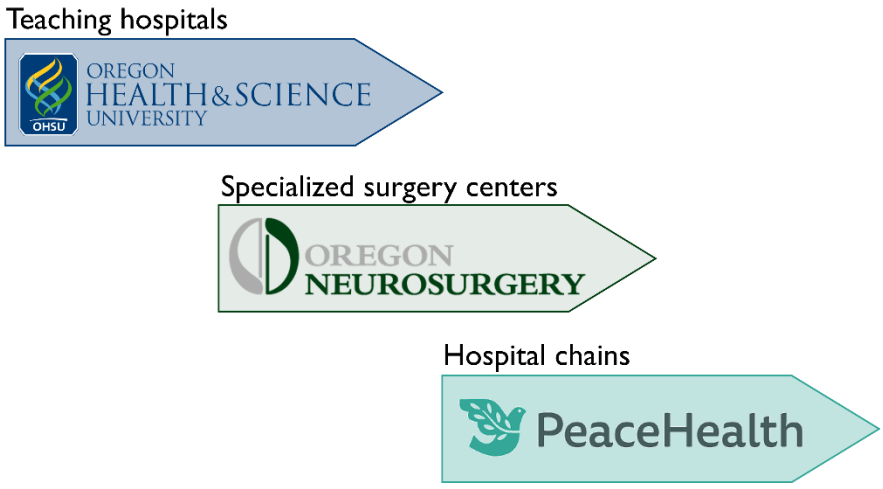

Figure 7.5. Go-to-market strategy framework for PeriMend3D: Diagram illustrating the phased commercialization approach progressing from early adoption within academic medical centers to broader expansion into private and hospital-based surgical practices, culminating in large-scale distribution.

Interview feedback reinforced the importance of personal relationships and on-site support. As Dr. Weeks noted, surgeons expect product representatives to assist during early cases, emphasizing the necessity of a robust sales and training team. A consignment-based purchasing model, suggested by Dr. Midha, will be adopted, allowing hospitals to stock guides on-site and pay upon use, minimizing barriers to trial and adoption.

Financial Model and Funding Strategy

Projected Financials (5-Year Plan)

- Year 1: Preclinical validation; costs ≈ $1.2 M.
- Year 2: Large-animal trials; costs ≈ $2.5 M; early grant revenue ≈ $0.75 M.
- Years 3-5: Clinical trials and commercialization; cumulative revenue ≈ $10 M by Year 5.

Funding Milestones

1. STTR Phase I/II grants: Non-dilutive funding for R&D and early testing.
2. Angel Round ($1 M): Supports pilot studies, team expansion, and regulatory preparation.
3. Series A ($12 M): Finances human trials and manufacturing scale-up.
4. Break-Even Analysis: Achieved by end of 2026, with a 40% gross margin target and manufacturing cost ≈ $300 per unit against a $2,500 price point.

This staged model mitigates risk, ensuring scientific progress aligns with investor expectations and regulatory deliverables.

Risk Analysis and Mitigation

Key risks and strategies include:

- Regulatory Delays: Early consultation with FDA and adoption of proven biomaterial standards mitigate uncertainty.

- Funding Shortfall: Diversified funding streams such as grants, angel, and venture capital reduce dependency on a single source.
- Market Adoption: Strong surgeon engagement, training, and consignment model reduce friction for adoption.
- Technical Challenges: Continuous product testing and iterative design ensure consistent quality and performance.
- Intellectual Property: Patent filings on scaffold geometry secure competitive protection.

Conclusion

PeriMend3D stands at the intersection of advanced biofabrication and clinical need. Guided by direct clinician feedback and rigorous scientific development, the company delivers a nerve repair solution that outperforms existing alternatives in usability, performance, and scalability. This structured commercialization strategy is anchored by validated market demand, regulatory foresight, and a sustainable financial model, which positions PeriMend3D to transform peripheral nerve repair.

Mission Statement

Driven by innovation and compassion, our mission is to transform peripheral nerve regeneration. Through cutting-edge 3D printing technologies like MEW, we design and create seamless tubular structures that will help patients regain motor control and function. Our goal goes beyond science; it's a dedication to restoring the simple yet profound gestures of everyday life

Executive Summary

PeriMend3D is an emerging biotechnology venture translating advanced 3D printing science into a transformative medical device for peripheral nerve repair. Rooted in the doctoral research of a bioengineering PhD candidate specializing in MEW, PeriMend3D develops biocompatible, customizable nerve guidance conduits that address the critical limitations of existing treatments for peripheral nerve injuries (PNI). Each year, more than 20 million people suffer from PNIs in the US, many requiring surgical repair. Current methods (autografts, allografts, and synthetic conduits) are restricted by donor-site morbidity, immune rejection, storage challenges, and poor structural reliability. PeriMend3D's 3D-printed nerve bridge directly responds to these shortcomings through precision design, shelf stability, and scalable manufacturability.

The company's solution combines biodegradable and biocompatible polymers with MEW technology, enabling micron-level fiber control that mimics the extracellular matrix and supports guided axonal growth. The result is a nerve guide that is thin yet mechanically robust, easy to handle during surgery, and customizable for different injury types and lengths. In contrast to autografts and cadaveric allografts, PeriMend3D eliminates the need for secondary donor-site surgery and bypasses complex cold storage logistics. Surgeon interviews, particularly with Dr. Bruce Watkins and Dr. Raj Midha, validated these priorities, emphasizing shelf-life, performance, and ease of use as top purchasing criteria. These direct insights shaped the final product design: strong yet flexible scaffolds with tunable permeability, optimized degradation, and standardized packaging for immediate use.

PeriMend3D's commercialization strategy is grounded in scientific credibility and market feasibility. The target market is the peripheral nerve repair sector, estimated at $7.5 billion and

growing at a CAGR of 9.2%. Initial market entry will focus on early adopters within university hospitals, followed by expansion to private surgical centers and larger hospital systems. Early clinical relationships and partnerships with key opinion leaders are already forming through collaborations at the University of Oregon's Knight Campus and affiliated hospitals. PeriMend3D's business model incorporates multiple revenue streams: direct sales to hospitals and surgical centers, licensing of scaffold designs and MEW technology, and research collaborations. The primary beachhead markets identified include traumatic hand surgery and breast reconstruction following mastectomy, both representing high-value segments with pressing clinical demand and existing reimbursement structures.

The venture's financial strategy follows a staged approach aligned with regulatory milestones. Early funding sources include STTR and SBIR Phase I/II grants, followed by a $1 million angel investment to complete preclinical validation and a $12 million Series A round to support clinical trials and FDA submission under the 510(k) pathway. Revenue generation is expected in Year 5, following successful regulatory clearance. By then, PeriMend3D projects $10 million cumulative revenues, driven by a scalable production model and premium pricing justified by superior clinical outcomes and logistical advantages.

PeriMend3D's competitive positioning is defined by high performance and long shelf-life. These attributes confirmed as decisive by surgeon interviews and plotted within a competitive matrix outperforming autografts, allografts, and existing synthetics. The venture's value proposition extends beyond innovation in materials: it offers surgeons convenience and reliability, hospitals cost efficiency, and patients faster recovery with reduced complications. The company's integration of advanced 3D printing, biomaterials science, and clinical insight exemplifies translational innovation in regenerative medicine.

Ultimately, PeriMend3D demonstrates how rigorous doctoral research can evolve into a commercially viable enterprise addressing a significant unmet clinical need. The project combines entrepreneurial acumen, scientific innovation, and stakeholder-driven design, positioning it to redefine the standard of care for peripheral nerve repair and expand the frontiers of bioengineered medical devices.

Concluding remarks for Chapter 7: Integration of Research and Entrepreneurship

The PeriMend3D commercialization pathway exemplifies the convergence of academic discovery and entrepreneurial execution. This process extends the traditional boundaries of research into real-world impact. The iterative cycle of hypothesis testing, prototype validation, customer discovery, and business model refinement mirrors the scientific method while cultivating essential translational skills.

Through hands-on experience, this work highlights acquisition of competencies in regulatory navigation, market analysis, financial planning, and interdisciplinary collaboration. These skills are critical for leadership in the biomedical innovation ecosystem. Courses in entrepreneurship and innovation provided the frameworks (e.g., Lean Startup, Business Model Canvas) that complemented laboratory research, enabling a holistic understanding of how scientific breakthroughs evolve into viable products.

Moreover, the engagement with clinicians, regulatory experts, and investors demonstrates how translational research thrives through stakeholder collaboration. This experience underscores the educational value of commercialization within doctoral training, by linking theoretical knowledge into societal impact, this way bridging the gap between bench science and patient care.

CHAPTER 8: CONCLUSION

This thesis presents MEW as a high-precision additive manufacturing technique to create scaffolds towards TE applications. This is achieved through systematic integration of theory, computational design, multi-material printing, biological validation, and translational strategy.

Summary of Scientific and Technological Contributions

The review A Decade of Melt Electrowriting (Chapter 2) contributed to the field by providing the first comprehensive synthesis of MEW's electrohydrodynamic behavior. This work formalized the concepts of jet stability, fiber trajectory, and process reproducibility, defining the operational window necessary for consistent scaffold fabrication. The insights gained here underpin all subsequent chapters and have been positively recognized in the field.

Chapter 3 advanced MEW into the digital domain through the development of a parametric modeling and G-code generation tool in Grasshopper. This innovation provided a predictive, visual platform for virtual prototyping and design iteration, bridging computational geometry with physical fabrication. It addressed a critical technological gap by enabling logic-based control over fiber placement and scaffold architecture, which is an essential prerequisite for reproducibility and scalability.

Chapters 4 and 5 expanded the material and biological dimensions of MEW. The multi-material fabrication system developed in Chapter 4 demonstrated how semi-crystalline and amorphous polymers can be integrated into tubular scaffolds. This work presents a platform that can be used to study the combination of flexibility with radial strength. Chapter 5 introduced biochemical modulation via hydrogel-peptide coatings, offering precise control of cell-material interactions.

Chapters 6 and 7 addressed scalability and translation. The automation of electrospun tube fabrication in Chapter 6 provided a reproducible, high-throughput method for scaffold production, while Chapter 7 articulated the commercialization pathway through the case study *PeriMend3D*. By integrating technical, regulatory, and market considerations, this final chapter demonstrated how academic innovation can evolve into a clinically feasible medical device strategy.

Concluding Remarks

The collective impact of this thesis lies in its demonstration that MEW is a fabrication method with potential as platform for regenerative medicine. This work establishes computational design frameworks, multi-material capabilities, and scalable automation strategies. The technologies and frameworks developed offer versatile strategies applicable to peripheral nerve, musculoskeletal and bone TE applications.

APPENDIX

1. Supporting Information for Chapter 3: Visualizing Fiber Path and Generating G-code for Melt Electrowriting of Tubular Scaffolds Using Grasshopper Software

Kelly L. O'Neill, Taite McLoughlin, Georgia Van der Linden, Ignacio Lopez Buson, Naomi C. Paxton, Mary Polites, Paul D. Dalton

Supplementary Video S3.1 demonstrates interaction with Grasshopper software to generate visualization of MEW fiber path.

Supplementary Video S3.2 demonstrates interaction with Grasshopper software to generate G-code in AeroBasic language.

Supplementary Video S3.3 compares the visualization to actual printing of the 90° crosshatch angle.

Supplementary Video S3.4 is a video recording of MEW printing onto a tubular collector of fibers parallel to the length of the tube.

Supplementary Video S3.5 compares recordings of MEW printing onto a tubular collector of the three crosshatch angles presented in this body of work: 45°, 67.5° and 90°. Left: Grasshopper generated rendered image of the different angles. Center: Video recordings of the first layer of the different angles. Right: Light microscope images of resulting scaffolds.

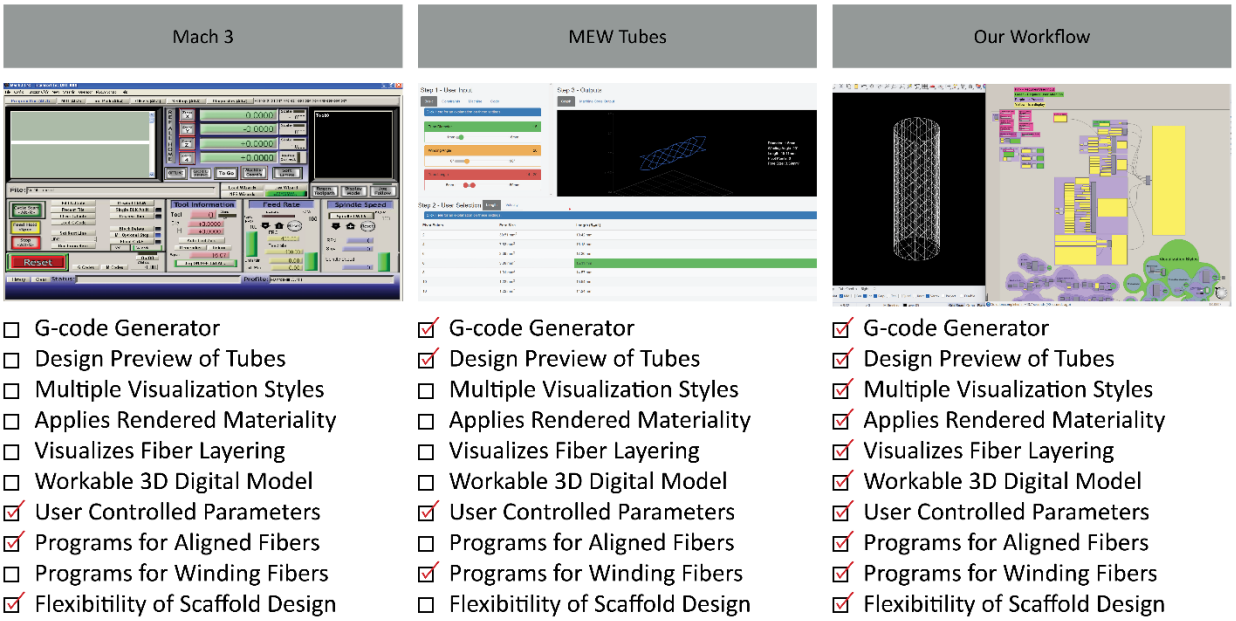

Figure S3.1. Current software comparison. This chart lists the similarities and differences of these digital environments.

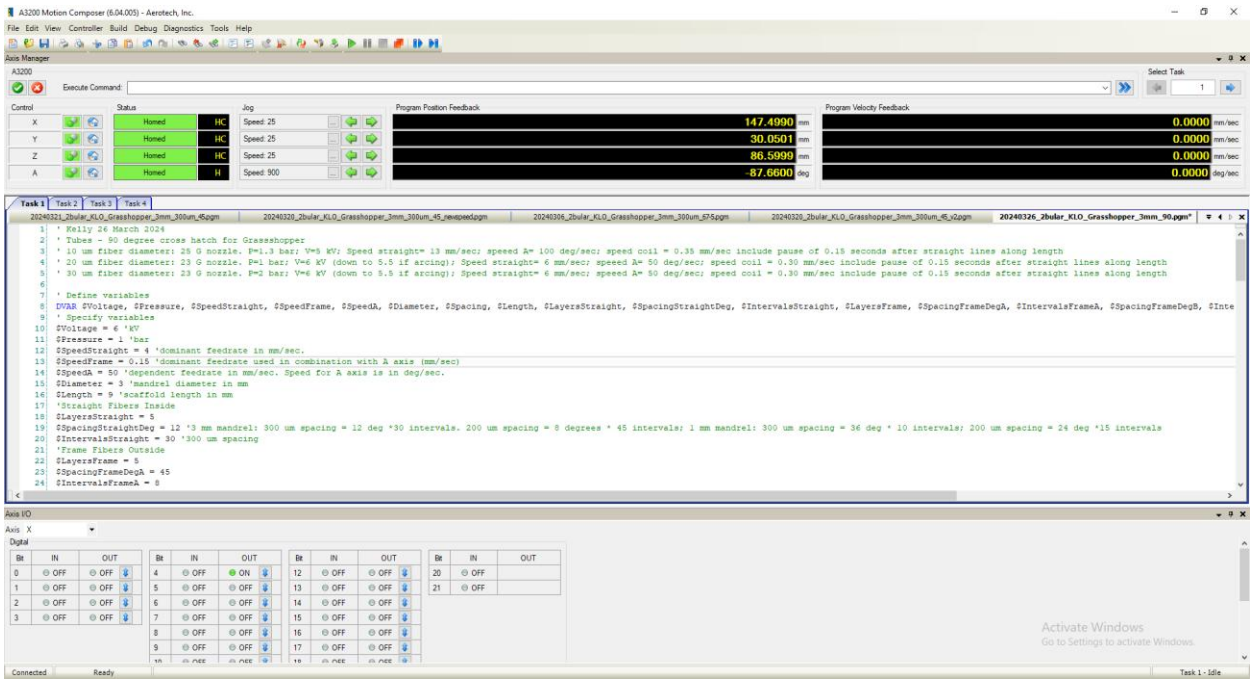

Figure S3.2. High resolution screenshot of Grasshopper parameter interface as shown in Figure 3.1D.

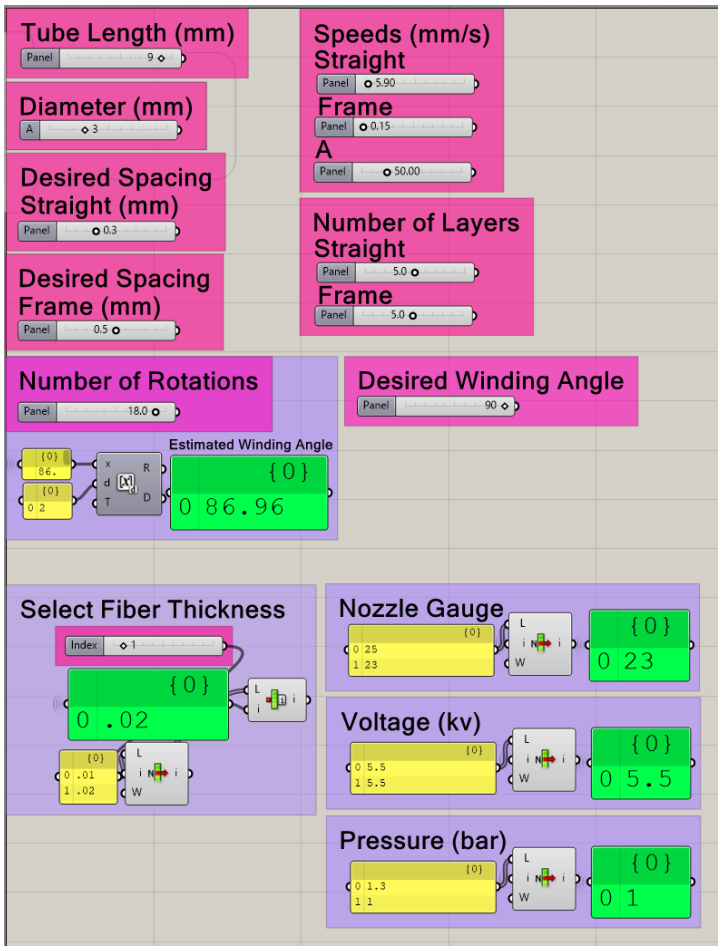

Figure S3.3. High resolution screenshot of Grasshopper parameter interface as shown in Figure 3.2. The user can choose design and printing parameters for fiber path prediction and G-code generation in AeroBasic script. Printing parameters shown correspond to scaffold with 3 mm inner diameter, 20 µm fiber diameter, 300 µm spacing along length and 90° crosshatch pattern with 500 µm spacing.

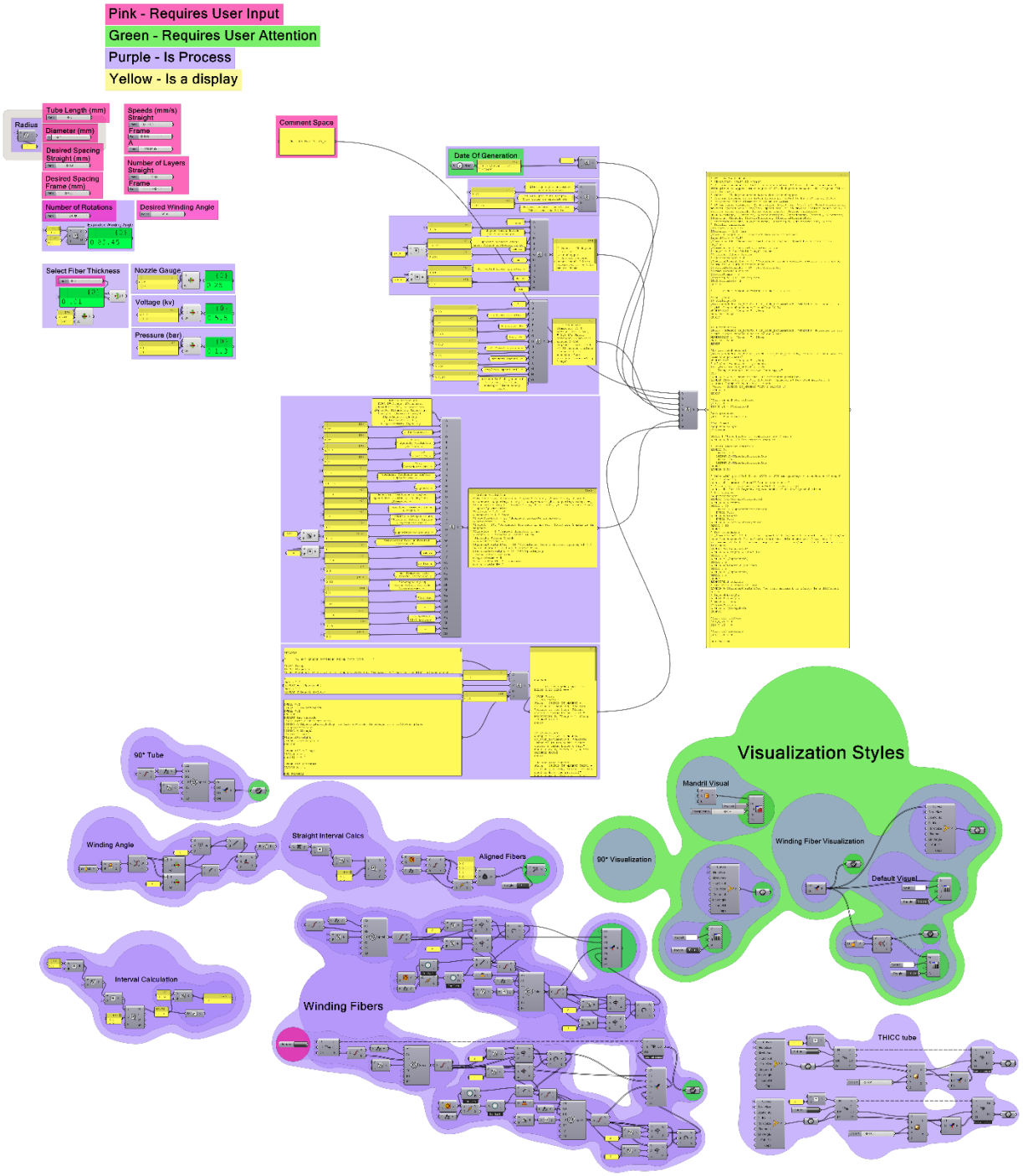

Figure S3.4. Image of complete Grasshopper definition, also available in high resolution here.

A

Measurement number	Spacing between fibers on crosshatch patters (μm)
1	525
2	510
3	522
4	508
5	505
6	515
7	496
8	500
9	540
Average	513
Standard dev.	13

B

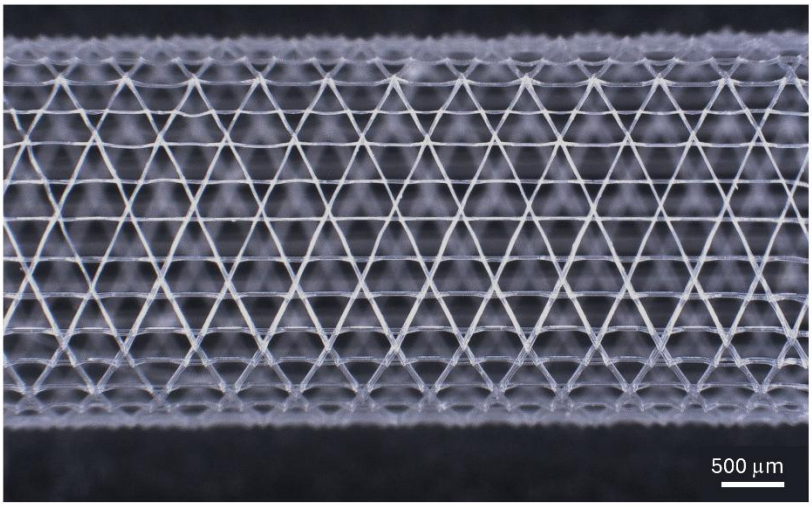

Figure S3.5. Measured inter fiber spacing of printed scaffolds A) Table of measurements and respective average and standard deviation. B) representative image taken using light microscope (Keyence, USA).

2. **Supporting Information for Chapter 4: High Precision Fiber Printing of Semi-Crystalline and Amorphous Polymer Materials to Create 3D Printed Tubular Scaffolds Produced by Melt Electrowriting**

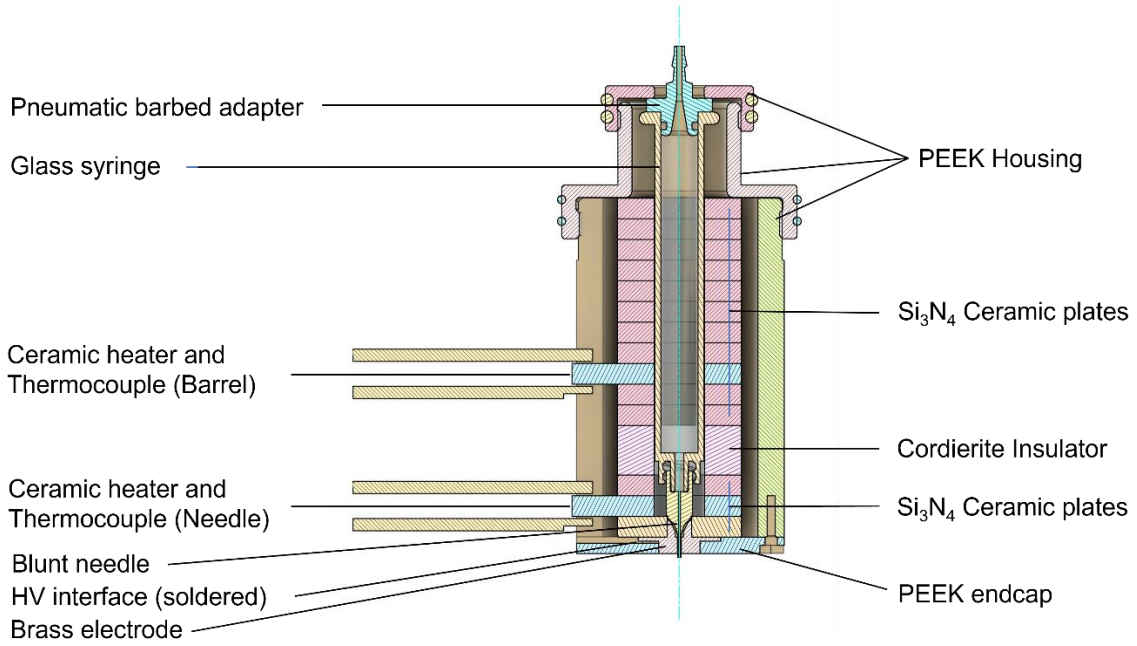

Figure S4.1. Schematic of printer head for custom-built MEW system.

3. Supporting Information for Chapter 5: Tailoring Cell Attachment onto Melt Electrowritten Scaffolds via Phase Separated Hydrogel Coating and Peptide Functionalization

Kelly L. O'Neill, Amanda Kurtz, Ievgenii Liashenko, Guilherme Rocha, Naomi C. Paxton, Paul D. Dalton

Supporting Video S5.1. Process of coating PCL MEW scaffolds with pHEMA and functionalization with peptide.

Supporting Video S5.2. Optical microscopy capturing the coating process of pHEMA on PCL MEW scaffolds, demonstrating the mechanism illustrated in Figure 5.1C.

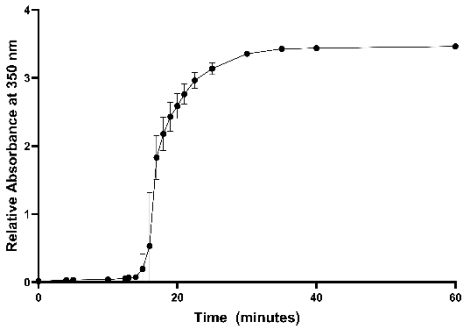

Figure S5.1. pHEMA growth rate along time, measured by absorbance at 350 nm.

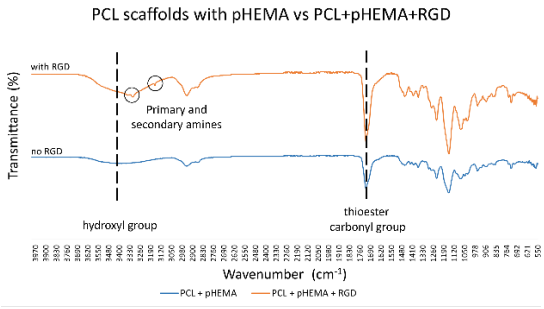

Figure S5.2. FT-IR (ATR) comparing peptide-functionalized to non-functionalized scaffolds pHEMA coated PCL scaffolds.

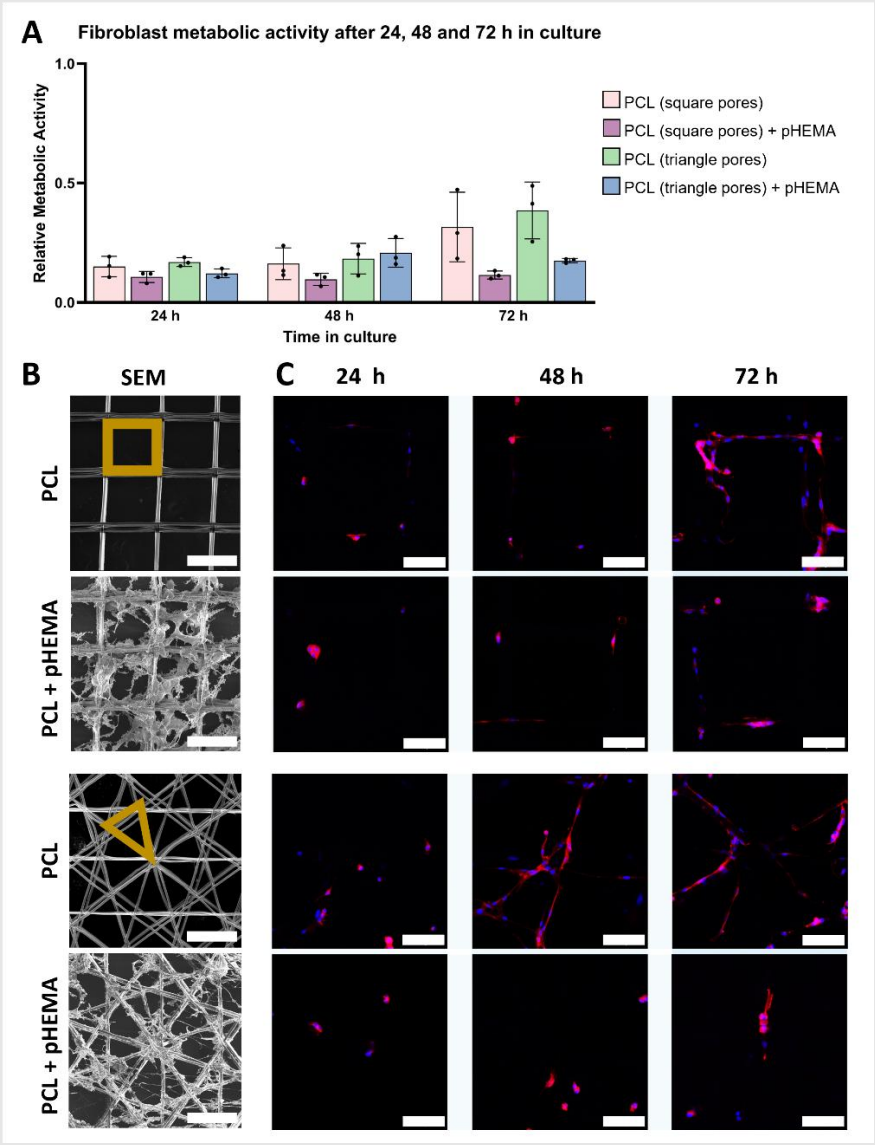

Figure S5.3. A) Cell metabolic activity for fibroblasts grown on PCL and pHEMA coated PCL scaffolds for 24, 48, and 72 h normalized to cells seeded directly into well and cultured for 72 h. Results from two designs are shown: square and triangle. Data represents mean and standard deviation for n=3. One-way ANOVA and post-hoc Tukey test within each timepoint showed no significant differences between conditions. B) Scanning Electron Microscope (SEM) images of non-coated and pHEMA coated scaffolds of square and triangle design. C) Confocal images of NIH3T3 fibroblasts grown on non-coated PCL and pHEMA coated PCL square (top) and triangle (bottom) shaped scaffolds for 24, 48 and 72 h (left to right). NIH3T3 cells were stained for actin filaments with Alexa Fluor™ 594 Phalloidin (shown in red) and nuclei with DAPI (shown in blue). Scale bars: B) 250 µm; C) 100 µm.

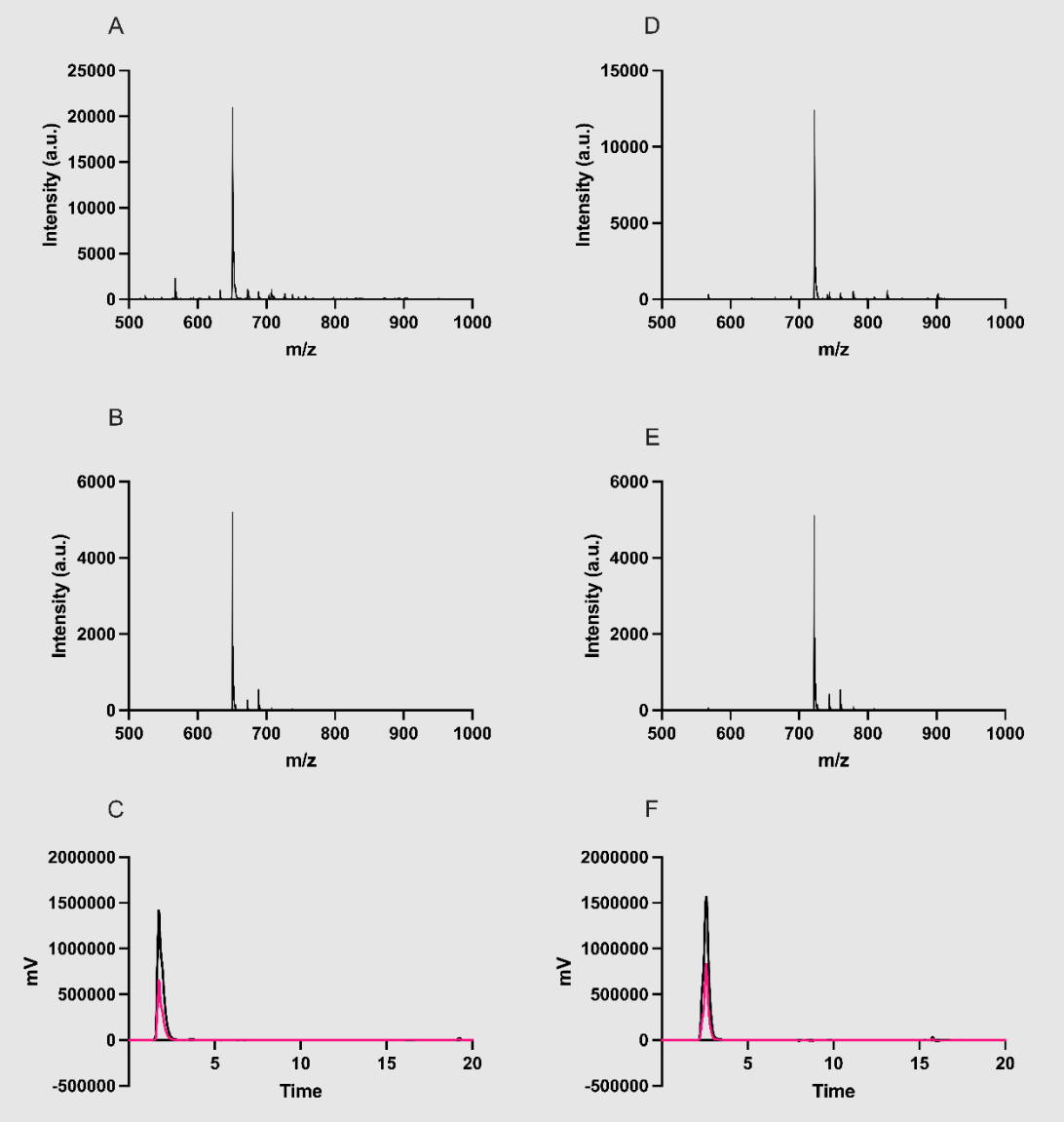

Figure S5.4. Peptide characterization by Mass Spectrometry Smart LS Matrix Assisted Laser Desorption/Ionization (MALDI) and analytical high-performance liquid chromatography (HPLC). A) RGD crude – full sequence: CG-RGD-SG with expected molecular weight of 650.66; B) RGD pure; C) HPLC spectra from pure RGD collected directly from data report: 97%; D) RGE crude – full sequence: CGG-RGE-SG with expected molecular weight of 721.74; E) RGE pure; F) HPLC spectra from pure RGE collected directly from data report: 95.5%. m/z: mass-to-charge; a.u.: arbitrary scale.

4. **Supplementary Information for Chapter 6: Automated Seamless Poly(ε-caprolactone) Electrospun Tubes for Critically-Sized Bone Defect Repair**

Kelly L. O'Neill, Kylie E. Williams, Auveen Hajarizadeh, Adam Rauff, Ievgenii Liashenko, Robert E. Guldberg, Paul D. Dalton

Manufacturing process of original and new design

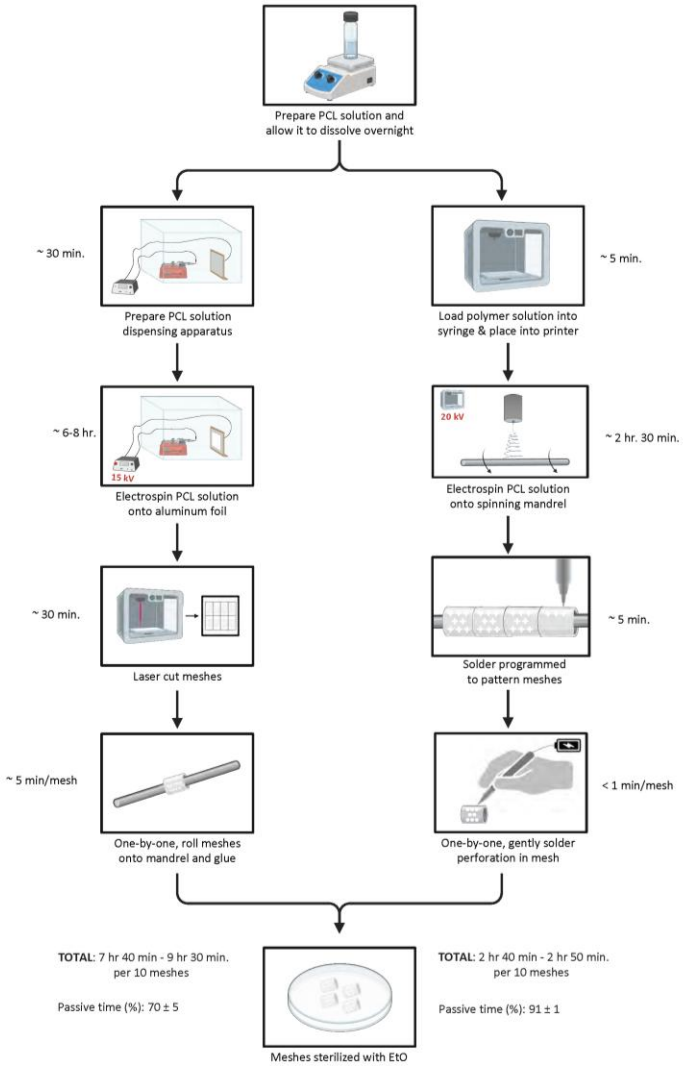

Figure S6.1. Comparison between manufacturing process of original versus new design, on the left and right, respectively. Noted are the approximate duration for each step of the process.

Thickness of solution electrospun membranes

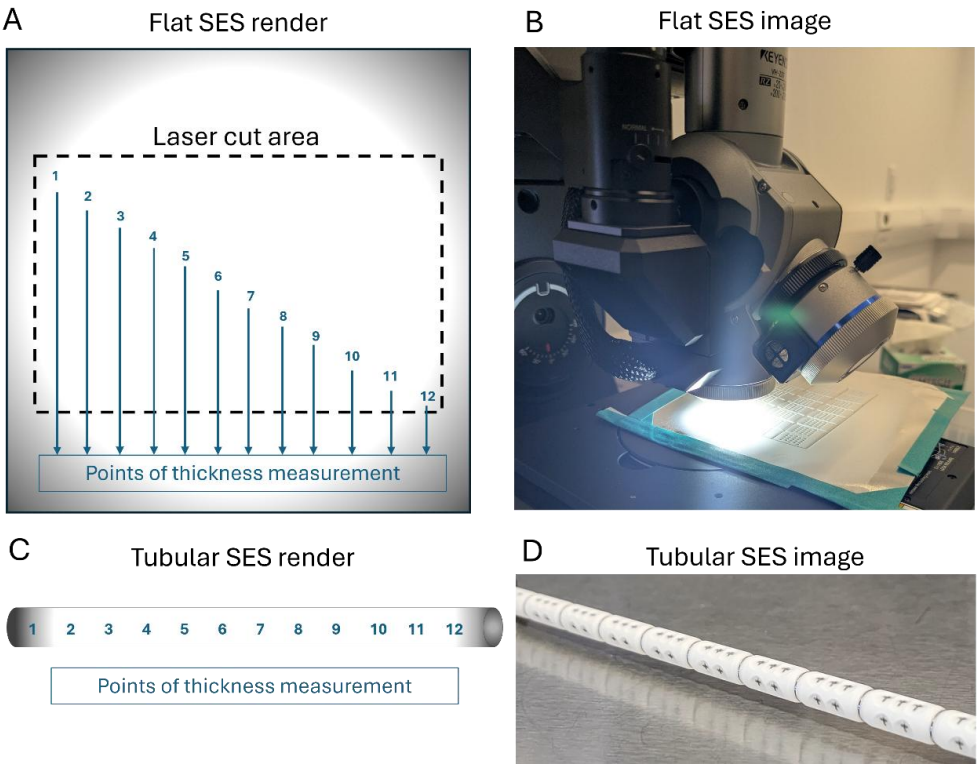

Figure S6.2. Location of measurements taken for thickness of SES membrane produced in flat (original) and tubular (new) A) flat render and B) photograph of flat SES membrane; C) tubular render and D) photograph of tubular SES membrane. Twelve points were chosen along the SES membrane.

Surgical utility of perforated meshes

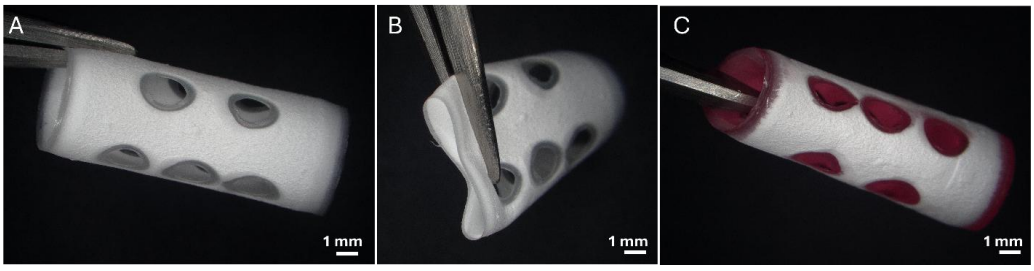

Figure S6.3. Surgical utility of perforated meshes. A) mesh held with tweezers; B) mesh compressed; C) mesh holding alginate dissolved in media. Scale bars: A-C) 1 mm.

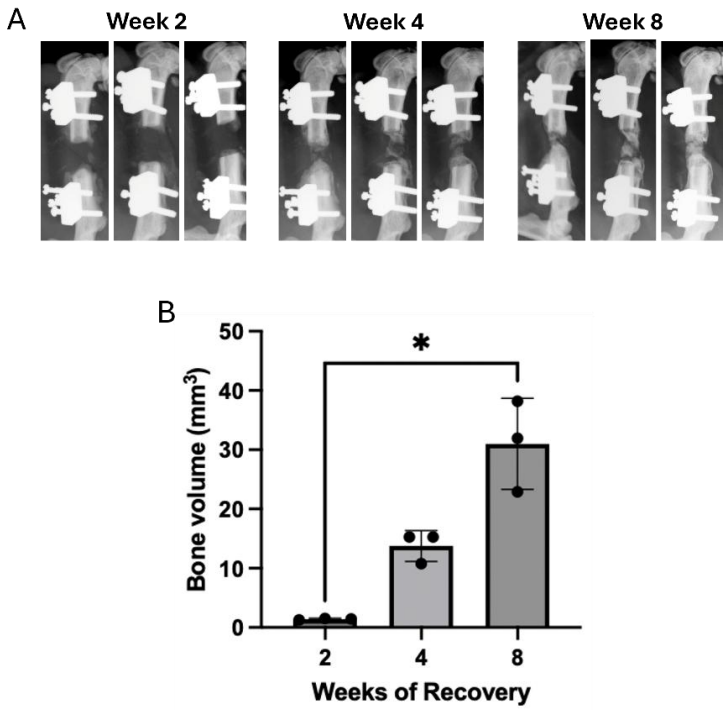

*Figure S6.4. Supporting information for in vivo study where new meshes facilitated bone healing as expected. A) Representative radiographs after 2, 4, and 8 weeks of recovery from 6 mm segmental femur defect surgeries. B) Corresponding longitudinal bone volume quantifications of newly formed bone within the defect region, as seen in Figure 6.5. Kruskal-Wallis nonparametric test revealed significant effect of time (**, p = 0.0036) and Dunn's multiple comparison's test revealed significant increase in bone volume from week 2 to week 8 (*, p = 0.0211).*

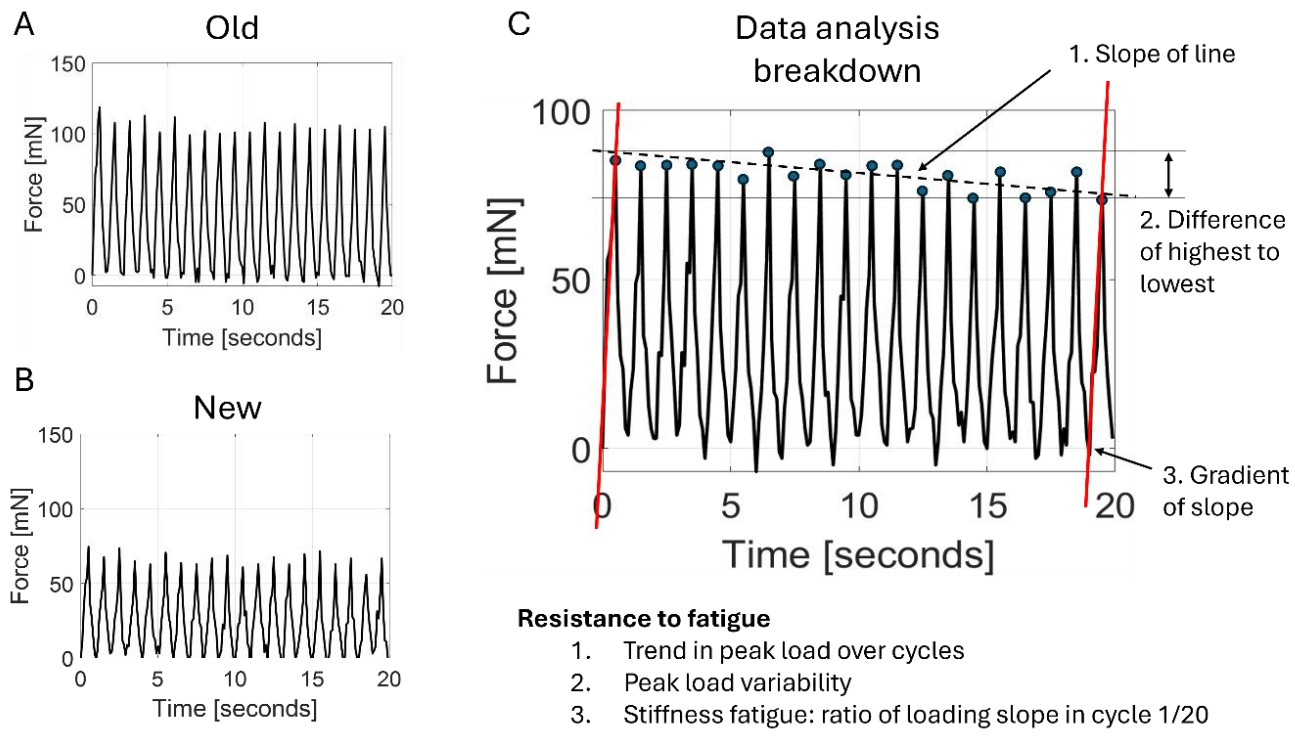

Figure S6.5. Mechanical testing of bone sleeves: A-B) representative plots of raw data of Figure 6.4 of main paper. Data shows original design hold greater resistance to compression compared to new design. C) breakdown of data analysis to retrieve resistance to fatigue. Meshes underwent resistance to lateral compression over 20 cycles at 1 Hz. Meshes were compressed to 50% of reference diameter.

Thickness measurements of original and new meshes

Table S6.1. Thickness of SES mesh produced in flat (original) compared to tubular (new).

Measurement number	Original (μm)	New (μm)
1	1125.9	399.4
2	1159.6	361.5
3	1426.2	316.4
4	1184.1	288.8
5	131.8	294.6
6	199.5	275.9
7	395.5	391.4
8	274.01	419.2
9	1314.9	325.7
10	1382	329.3
11	600	302.5
12	499.6	380.3
Average	807.8	340.4
Std	479.2	46.2
Coefficient of variation	42.1%	9.6%

Fiber diameter measurements of original and new meshes

Table S6.2. Diameter of SES fibers produced in original design (printed as flat) compared to new design (printed as tube).

Measurement number	Original (nm)	New (nm)
1	198.7	467.7
2	275.6	445.3
3	508.2	184.9
4	909.1	784.4
5	123.3	748.7
6	174.3	413.4
7	77.9	748.7
8	246.5	578.8
9	645.2	482.1
10	281.1	522.9
11	55.1	298.1
12	77.9	445.3
Average	297.7	510.0
Std	250.5	174.4
Coefficient of variation	84%	34%

Supplementary videos

Supplementary Video S6.1 – Solution Electrospinning (SES) setup and SES jet close-up. The jet is shown by a green laser pointer, demonstrating a vertical jet for 3-4 cm before traditional SES whipping (off screen).

Supplementary Video S6.2 – Perforations of tubular scaffolds are achieved by programmed solder movements.

Supplementary Video S6.3 – Lateral compression testing of bone sleeve (new design).

List of Abbreviations

2D	two-dimensional
3D	three-dimensional
AM	additive manufacturing
APS	ammonium persulfate
BMP-2	bone morphogenic protein-2
CAMCOR	center for advanced materials characterization in Oregon
CEW	cell electrowriting
CNC	computer numerical control
CTS	critical translation speed
DAPI	4’,6-diamidino-2-phenylindole
DCM	dichloromethane
DMEM	Dulbecco's modified eagle medium
DMF	dimethylformamide
DoE	design of experiments
ECM	extracellular matrix
EtO	ethylene oxide
FBS	fetal bovine serum
FFF	fused filament fabrication
FTIR–ATR	Fourier transform infrared spectroscopy – attenuated total reflectance
GelMA	gelatin methacrylate
GPC	gel permeation chromatography
HFIP	hexafluoro-2-propanol
HPLC	high-performance liquid chromatography
IACUC	institutional animal care and use committee
KCUS	Knight campus undergraduate research program
MALDI	matrix-assisted laser desorption/ionization
MES	melt electrospinning
MEW	melt electrowriting
micro-CT	micro-computed tomography
MTT	3-(4,5-dimethyl-2-thiazolyl)-2,5-diphenyl-2H-tetrazolium bromide
NaOH	sodium hydroxide
NEAA	non-essential amino acids

NGC	nerve guidance conduit
OIC	Oregon innovation challenge
ON	overnight
p(CL-co-AC)	poly(ε-caprolactone-co-acryloyl carbonate)
p(LLA-co-CL-co-AC)	poly(L-lactide-co-ε-caprolactone-co-acryloyl carbonate)
PCL	poly(ε-caprolactone)
PEEK	polyether ether ketone
PEG	poly(ethylene glycol)
PEtOx	poly(2-ethyl-2-oxazoline)
PFA	paraformaldehyde
pHEMA	poly(2-hydroxyethyl methacrylate)
PLCL	poly(L-lactide-co-ε-caprolactone)
PLLA	polymer poly(L-lactic acid)
PNI	peripheral nerve injuries
polyHIPE	polymerization of high internal phase emulsion
POx	poly(2-oxazoline)
PP	polypropylene
PVDF	poly(vinylidene fluoride)
RGD	arginine-glycine-aspartic Acid
ROI	region of interest
SEM	scanning electron microscopy
SES	solution electrospinning
sP(EO-stat-PO)	star-shaped poly(ethylene oxide-stat-propylene oxide)
TE	tissue engineering
TEA	triethanolamine buffer
TEMED	tetramethylethylenediamine
TFA	trifluoroacetic acid
ToF-SIMS	time-of-flight secondary ion mass spectrometry
UHMWPE	ultra-high molecular weight polyethylene
VOI	volume of interest
XPS	X-ray photoelectron spectroscopy